Carbon-Based Nanomaterials as an Anode for Lithium Ion Battery

Fei Yao, Costel Sorin Cojocaru

Carbon-Based Nanomaterials as an Anode for Lithium Ion Battery

Fei YAO

LPICM-École Polytechnique, CNRS (UMR 7647)
Laboratoire de Physique des Interfaces et Couches Minces
Route de Saclay; 91128 PALAISEAU Cedex , France

The Graduate School
Sungkyunkwan University
Department of Energy Science (DOES)
IBS Center for Integrated Nanostructure Physics
300 Cheoncheon-dong, Jangan-gu, Suwon 440-746, R. O. Korea

THÈSE

Présentée pour obtenir le grade de
DOCTEUR DE L' ÉCOLE POLYTECHNIQUE
Spécialité: Physique
Par
Fei YAO

Carbon-Based Nanomaterials as an Anode for Lithium Ion Battery

Soutenue le 27 / 06 / 2013 devant le jury constitué de :

M. Jean-Pierre Pereira-Ramos	Directeur de Recherche CNRS	Rapporteur
M. Kee Seok Nahm	Professor à Chonbuk National University	Rapporteur
M. Won Sub Yoon	Professor à Sungkyunkwan University	Examinateur
M. Marc Chatelet	Directeur de Recherche CNRS	Examinateur
M. Costel-Sorin Cojocaru	Chargé de recherche au CNRS Enseignant à l'École polytechnique	Directeur de Thèse
M. Young Hee Lee	Professor à Sungkyunkwan University	Directeur de Thèse

LABORATOIRE DE PHYSIQUE DES INTERFACES ET COUCHES MINCES (LPICM)
CNRS, UMR7647, ÉCOLE POLYTECHNIQUE

This certifies that the dissertation
of Fei YAO is approved.

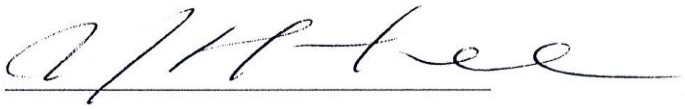

Lee, Young Hee: Thesis Supervisor

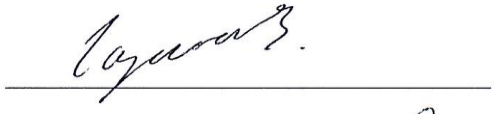

Costel-Sorin Cojocaru: Thesis Supervisor

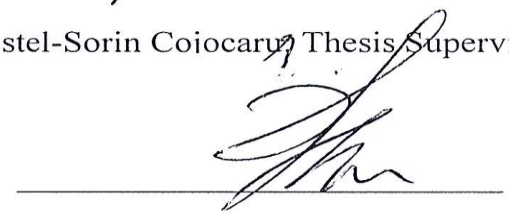

Yoon, Won Sub: Thesis Committee Member

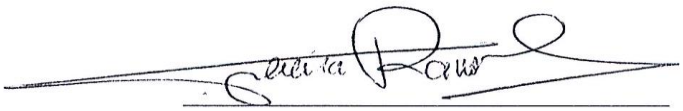

Jean-Pierre Pereira-Ramos: Thesis Committee Member

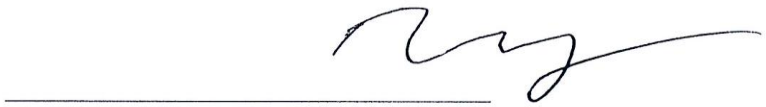

Kim, Ki Kang: Thesis Committee Member

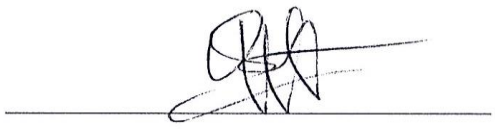

Marc Chatelet: Thesis Committee Chairman

The Graduate School
Sungkyunkwan University
June 2013

ACKNOWLEDGMENTS

First and foremost, I would like to express my greatest gratitude to Prof. Young Hee Lee and Dr. Costel Sorin Cojocaru, my advisors of graduate research, for their patient guidance and continuous support throughout the last three years. They taught me strict sense of research, humble attitude of study, and correct path in life. I feel so lucky and honored for being their student in the most important days of my growth. Their great fairness, concern and understanding will be appreciated through all my life.

My sincerely thanks are extended to all my coworks, Dr. Fethullah Güneş, Mr. Bing Li, Dr. Kangpyo So, Mr. Huy Quang Ta, Mr. Jian Chang, Mr. An Quoc Vu, Mr. Seung Jin Chae, Dr. Hongyan Yue, Prof. Didier Pribat and Prof. Sishen Xie, in Sungkyunkwan University. And also Dr. Seung Mi Lee from Center for Nanocharacterization, Korea Research Institute of Standards, Dr. Kyeu Yoon Sheem from Science and Samsung SDI Corporate R&D Center.

I would like to dedicate this thesis to my parents and sister for their continuous understanding, support, and love. My deepest appreciation to my beloved husband, Humin Li, for his love, encouragement and accompanying all the time!

TO MY PARENTS…

ABSTRACT

In this thesis work, carbon-based nanomaterials using as an anode for lithium ion battery have been generally investigated. Compared to typical micron-sized carbon materials, nanosized carbon materials exhibited great potentials not only in practical anode application but also in the fundamental science exploration of Li ion diffusion. In the case of practical application, one dimensional carbon nanofibers (CNFs) fabricated by electrospinning was prepared for anode material. The structure involves neither a metal substrate nor binders and therefore eventually benefited the capacity and long term stability. Yet, the energy density is still limited to 370 mAh/g of conventional carbon. In order to improve the capacity of raw carbon nanofibers, silicon, a high Li storage material, was incorporated by electrochemical deposition. The resulted Si/CNF mat improved clearly the capacity of carbon materials more than twice for most of cases.

In the case of fundamental study, chemical vapor deposition (CVD)-synthesized two dimensional graphene was chosen to be a media to reveal the diffusion pathways of Li ion. Compared to typical graphite which contains both basal and edge planes, a well defined basal plane with large area can be realized in graphene to provide a comprehensive picture of lithium diffusion mechanism. We have discovered that electrochemical reaction of electrode (substrate/graphene) not only is related to the number of graphene layers but also relies on the defect sites on the basal plane of graphene. Combing the experimental results and density functional theory calculations, we proved that basal plane hindered lithium ion diffusion with a high diffusion barrier height, whereas divacancies and higher order defects can be shortcuts for lithium ion diffusion.

Keyworks: nanocarbon materials, lithium ion battery, carbon nanofiber, silicon, graphene, lithium ion diffusion

RESUME

Dans ce travail de thèse, nous avons exploré l'utilisation des nanomatériaux à base de carbone comme anode pour les batteries lithium-ion. Par rapport aux matériaux d'anode classiques qui sont de type carbone graphitique a des tailles de grains de l'ordre du micromètre, les matériaux de carbone de taille nanométrique présentent un grand potentiel non seulement pour l'application pratique en tant que matériau d'anode, mais aussi du point de vue de la science fondamentale car permettent l'exploration fine des phénomènes de diffusion des ions lithium. Dans le cadre de l'application pratique, nous avons exploré les nanofibres unidimensionnelles de carbone (CNF) en tant que matériau d'anode. Cette structure d'anode comporte un substrat métallique comme collecteur de courant mais n'avons pas utilisé des liants ce qui bénéficie a la stabilité à long terme. Pourtant, la densité d'énergie que nous avons obtenu était encore limitée à 370 mAh /g similaire à celle du carbone conventionnel. Afin d'améliorer la capacité des nanofibres de carbone bruts, nous les avons recouverts de silicium (par dépôt électrochimique), un matériau d'insertion de lithium avec une bien plus importante capacité de stockage. Le tapis hybrides Si / CNF ont permis d'améliorer nettement la capacité des matériaux de carbone jusqu'à deux fois de plus pour la plupart des cas.

Du point de vue des études fondamentales, le graphène matériau bidimensionnel, a été synthétisé par dépôt chimique en phase vapeur (CVD) et utilisé comme un support pour mettre en évidence les chemins de diffusion des ions lithium. Par rapport à du graphite classique qui contient à la fois les deux plans de type basal et prismatique, seulement un plan basal bien défini et d'une grande surface spécifique peut être réalisé dans le cas du graphène. Nous avons découvert que la réaction électrochimique a l'électrode (substrat / graphène) est non seulement liée au nombre de couches de graphène mais s'appuie également sur la présence de défauts dans le plan de graphène. Combinant les résultats expérimentaux et les calculs de théoriques, nous avons pu prouver que le plan basal empêche la diffusion des ions de lithium avec une hauteur de barrière de diffusion élevé, alors que les divacancies et les défauts d'ordre supérieur peuvent constituer des raccourcis pour la diffusion des ions de lithium.

Keyworks: Matériaux des nanocarbonés, batterie lithium-ion, nanofibre de carbone, Silicium, graphène, diffusion des ions lithium

Table of Contents

Chapter 3. Silicon-Coated Carbon Nanofiber Mat for Anode of Lithium Ion Battery

List of Tables

List of Figures

INTRODUCTION

The issue of the sustainability of energy supply has attracted worldwide concern due to the crisis in rapid depletion of fossil energy resources along with serious environmental pollution issues. Over the past several decades, tremendous efforts have been made in developing alternative technologies to harvest and store sustainable clean energy. Thanks to the development of nanoscience and nanotechnology, clean energy technologies are progressing impressively which makes them more practical and price competitive with fossil fuels. Clean energy technology covers production, storage, and conversion. Researches on energy production from renewable natural resources include solar energy conversion, wind, geothermal and hydraulic energy and involve often heavy engineering works. Our main concern using nanoscience from basic science point of view is energy storage. Among all different kinds of energy storage systems, rechargeable lithium-ion battery (LIB) is one of the greatest successes of modern material electrochemistry. It has drawn the most attention not only because of its higher energy density and longer cycle life compared to any existing battery systems but also its lightweight and compact which benefit the application in hybrid vehicles and portable electronics [1].

LIB consists of an anode (negative electrode) and a cathode (positive electrode). These two electrodes are capable of reversibly hosting lithium in ionic

form. Common candidates for the cathode are lithiated metal oxides and carbonaceous materials for the anode. Prior to the discovery of graphite anode materials, lithium metal had been used. However, possibility of thermal runaway caused by the internal shorts triggered by the formation of lithium dendrites has been a long standing issue [2]. The use of graphite as an anode material for intercalating lithium ions in rechargeable LIB was then proposed [3]. It is still the main stream of anode material for commercial LIB up to now due to its well defined layered structure for lithium intercalation, low operating potential, and remarkable interfacial stability [4]. Unfortunately, the intercalation capacity of lithium ions in graphite is limited to 372 mAh/g with LiC_6 stoichiometry. Numerous efforts have been made to increase this value by modifying the crystallinity, the microstructure, and the micromorphology of the carbonaceous material [5-8]. These structural parameters play a crucial part in determining and optimizing the electrochemical performance of carbon anodes.

The exploration of nanomaterials and nanocomposites provides us new opportunities to improve the anode performance of LIB. Compared to micrometer-scaled carbon material, nanostructured carbon exhibits differences not only in dimensionality and morphology, but also in the distribution of chemical bonding which allows the mixtures of local electronic structures between sp^2 and sp^3 [9] Therefore, carrier transport properties are different from classic carbon material when nanometer-scaled carbon is in contact with

reactants. Nanostructured carbon materials with high accessible surface areas and short diffusion time for lithium ions open new perspectives for high energy density and high power density LIB.

In order to fully develop the potential of nanoscaled carbon as an anode for LIB, a systematical study is needed. In this thesis work, after a brief overview of LIB (chapter one), fundamentals that provide the basic idea of operation mechanism in LIB, types of conventional carbon anode materials, and their anode performance will be reviewed in chapter two. Chapter three will mainly focus on studying the one dimensional carbon nanofiber anode material. An easy fabrication process, electrospinning, which is a good for mass production is introduced for raw carbon nanofiber synthesis. In order to improve the performance of raw carbon nanofiber, Si, a high Li storage material, is incorporated through electrochemical deposition method. Using nanoscaled carbon material for fundamental research of lithium ion diffusion pathway is given in chapter four. Here, two dimensional graphene synthesized by chemical vapor deposition is chosen to study the nature of Li ion diffusion since it is the basic building block of graphite which is the most common material for anode.

Finally, a general conclusion and perspectives are given.

Bibliography of Introduction

[1] J. M. Tarascon, M. Armand, *Nature* **2001**, *414*, 359.

[2] F. Orsini, *et al*., *J. Power Source* **1999**, *81***,** 918.

[3] M. Armand, P. Touzain, *Materials Science and Engineering* **1977**, *31*, 319.

[4] M. Winter, O. J. Besenhard, E. M. Spahr, P. Novák, *Adv. Mater.* **1998**, 10, 725.

[5] M. Winter, J. O. Besenhard, *Lithium Ion Battery: Fundamentals and Performance* **1998** (Eds.: M. Wahihara, O. Yamamoto), Wiley-VCH, Weinheim.

[6] A. Mabuchi, K. Tokumitsu, H. Fujimoto, T. Kasuh, *J. Electrochem. Soc.* **1995**, *142*, 1041.

[7] W. Ruland, *J. Appl. Phys.* **1967**, *38*, 3585.

[8] M. Endo, C. Kim, K. Nishimura, T. Fujino, K. Miyashita, *Carbon* **2000**, *38*, 183.

[9] D. S. Su, R. Schlögl, *ChemSusChem*, **2010**, *3*, 136.

Outline of Chapter One

Overview of Rechargeable Lithium Ion Battery

CHAPTER ONE

Overview of Rechargeable Lithium Ion Battery

1.1 Electrochemical Energy Storage Systems

Systems for electrochemical energy storage convert chemical energy into electrical energy. Electrochemical energy storage devices basically include batteries, fuel cells, and electrochemical capacitors (ECs). Although the mechanisms for energy storage and conversion are different, similarities do exist among these three systems. Common features are that batteries, fuel cells, and ECs consist of two electrodes which in contact with electrolyte. Requirements upon electron and ion conduction in electrodes and electrolyte are valid for all three systems. Furthermore, electron and ion transport are separated during the charge/discharge processes which take place at the phase boundary of the electrode/electrolyte interface [1]. The main difference between battery, fuel cell and ECs is the way of elec trical energy generation. In batteries and fuel cells, electrical energy is produced by conversion of chemical energy via redox reactions (Faradic process) at the anode and cathode. On the other hand, in ECs, energy may not be delivered via redox reactions but rather via the formation of electrical double layers (non-Faradic process) by orientation of electrolyte ions at the electrode/electrolyte interface, and thus the use of the terms anode and cathode may not be appropriate [2].

In order to value the energy contents of a system, terms of "energy density" (or "specific energy") and "power density" (or "specific power") are used. "Energy density" is expressed in watt-hours per liter (Wh/L) [or in watt-hours per kilogram (Wh/kg)] and "power density" is expressed in watt per liter (W/L) [or in watt per kilogram (W/kg)] [2]. To compare the performance of various energy storage devices, a reprehensive chart known as the Ragone plot was developed. In such a plot, the values of specific energy (in Wh/kg) are plotted versus specific power [3], as shown in **Figure 1.1**. It is clear to see that fuel cell can be considered as high energy density system and supercapacitor as high power density system. However, battery has intermediate energy and power characteristics. Compared to fuel cells and supercapacitors, batteries have realized the biggest application markets so far. Whereas supercapacitors have found its own position as memory protection in several electronic devices and instantaneous power backup systems, fuel cells are basically still in the development stage [1].

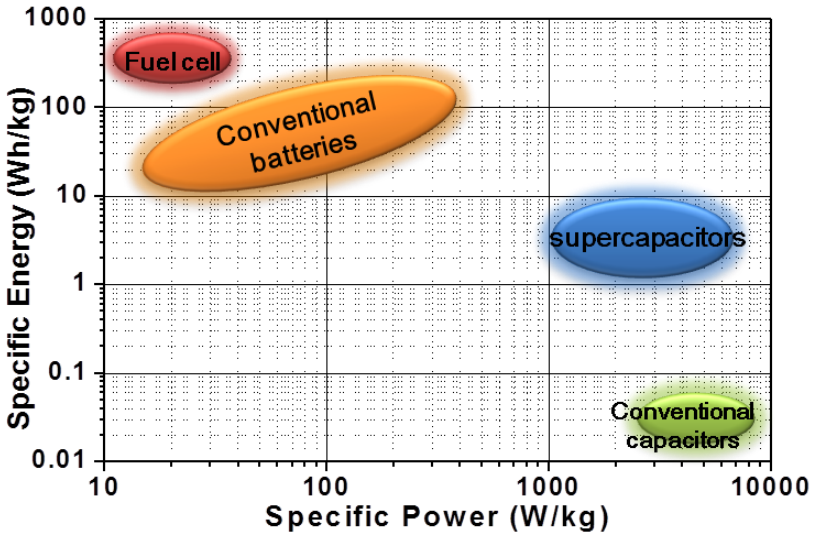

Figure 1.1. Ragone plot showing energy density vs. power density for various energy storage devices. Cited and modified from Ref. [3].

1.2 Rechargeable Lithium Based Battery

There are two types of batteries: primary batteries that are designed to be used once and discarded, and secondary batteries that are designed to be recharged and used multiple times. Therefore, they are also named as disposable batteries and rechargeable batteries. Common types of disposable batteries such as zinc–carbon battery cannot be reliably recharged, since the chemical reactions are not easily reversible and active materials cannot recover to the original forms [4]. On the other hand, electrochemical reactions in rechargeable batteries such as nickel-cobalt battery and lithium-based batteries are electrically reversible.

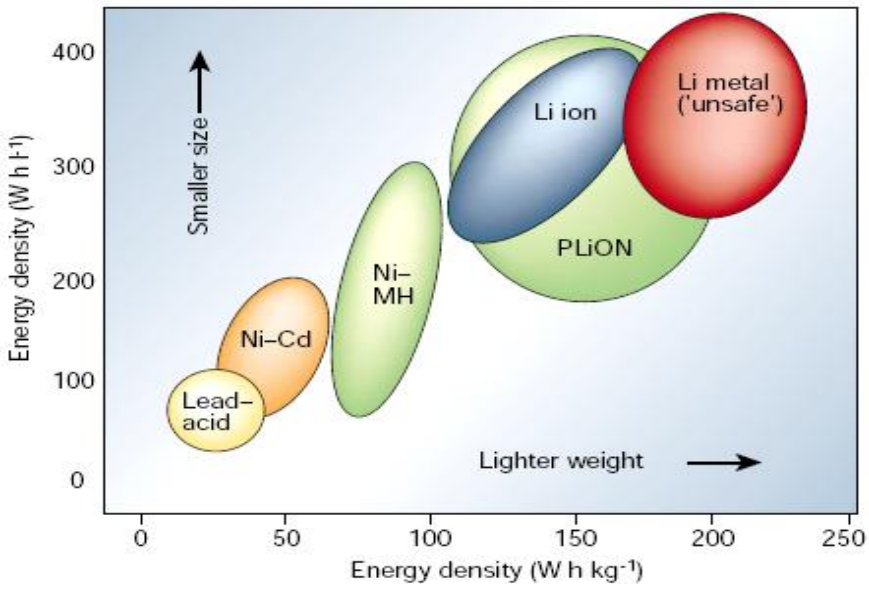

Figure 1.2. Comparison of the different battery technologies in terms

of volumetric and gravimetric energy density. Cited from Ref. [5].

Considering the requirements of modern society with popular portable electronics, rechargeable batteries are more favorable nowadays. The development of rechargeable batteries is a long story. To this date, among various existing technologies, such as lead-acid, Ni-Cd, nickel-metal hydride (Ni-MeH), Li-based batteries draw the most attention because of their high energy density and possibility of compact-flexible design, as indicated in **Figure 1.2**. Combining the profound mechanism study and the involvement of advanced materials, they have become the most dominant power source for cell phones, digital cameras, laptops etc. According to the recent market investigation, the share of worldwide sales for Ni–Cd and Ni–MeH batteries are 23 and 14%. However, Li-ion portable batteries take up to 63% of the battery market [5].

The starting point of incorporating lithium metal in battery technology is the fact that lithium is the most electropositive (–3.04 V Vs standard hydrogen electrode) as well as the lightest (specific gravity ρ=0.53 g cm^{-3}) metal which benefits the design of high energy density system [5]. Lithium metal as an anode was firstly reported in 1970 where TiS_2 was used as a cathode [6-8]. However, Li-metal cell encountered many problems. One of shortcomings is redeposition of lithium as a form of metal and uneven dendrite formation during subsequent charge/discharge cycle, as shown in **Figure. 1.3a**. This could lead to a short

circuit problem and thus explosion issues [9]. Therefore, even though Li-metal based cells exhibit the highest energy density as shown in **Figure 1.2**, their practical application is limited. Upon the inspiration of the development on the positive electrode which used Li$x$$MO_2$ (where M is Co, Ni or Mn) as a host material for Li ions [10-11], the Li metal is not necessarily required, therefore a concept so-called Li-ion or rocking-chair battery which introduced a second host material to replace Li metal was emerged to solve the safety issues in rechargeable Li-metal battery, as shown in **Figure 1.3b** [12-15].

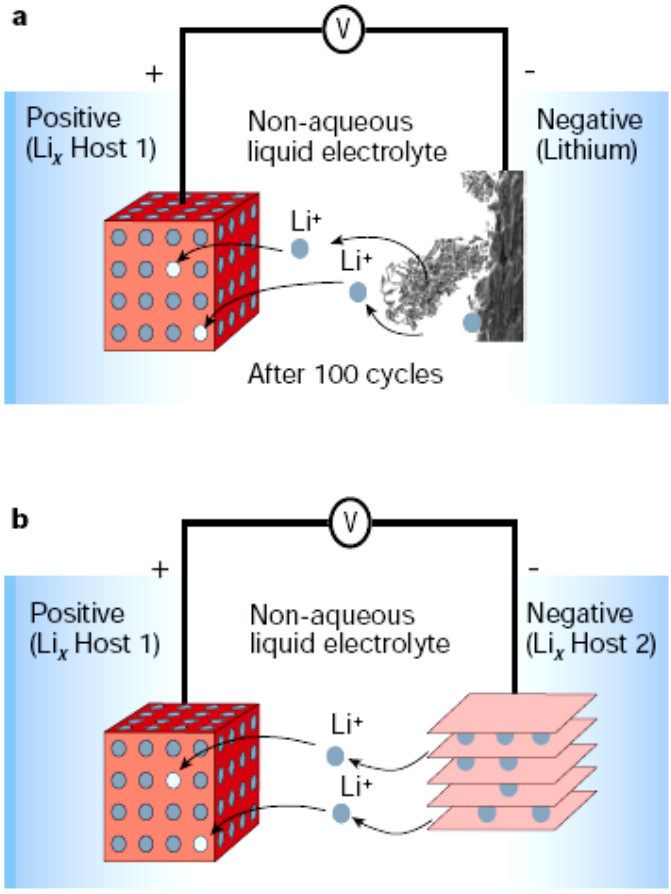

Figure 1.3. Schematic representation of lithium batteries. **a**,

Rechargeable lithium-metal battery, dendrite formation was shown in the negative electrode. **b**, Rechargeable lithium-ion battery. Cited from Ref. [5].

1.3 Rechargeable Lithium Ion Battery

The configuration of Li-ion battery electrodes is two types of lithium host materials (**Figure 1.3b**). The storage capacity of the battery is given by the amount of Li that can be stored reversibly in these two electrodes. To be clear, for rechargeable Li-metal batteries, the positive host electrode does not need to be lithiated before cell assembly since the use of metallic Li as the negative electrode. In contrast, for Li-ion batteries, the positive host electrode usually acts as a source of Li since the common negative electrode such as carbon, Si, transition metal oxide contains no Li. Thus, air-stable Li-based intercalation compounds in positive electrode are required to complete the cell assembly.

The structural stability of the host material during insertion and de-insertion of Li ions is a critical factor since it determines the long term stability of Li-ion battery. Generally, anode materials can be classified into three categories according to the Li storage mechanisms besides graphite: alloying, insertion, conversion. Most of these materials show different disadvantages compared to graphite, as indicated in **Figure 1.4**. In the case of Li alloy (Si, Sn, Ge, Al, Pb etc) and conversion-based electrodes (CoO, Fe_2O_3 etc), the volume change

between the Li-containing states and the corresponding lithium-free states is very large due to the mechanical stresses generated during charge/discharge cycles. Therefore, the cracks are easily produced and thus the electrodes collapse. So the cycle life is very much limited. In the case of insertion based materials (TiO_2, MoO_2 etc), rather low capacity is the key factor needed to be improved. In contrast, materials with two dimensional layered structure such as carbonaceous materials, show good cycling behavior since this kind of Li^+ insertion materials exhibits low mechanical strain with small volume changes [2, 5, 12-15]. At the present time, research and development activities are mainly focused on such highly reversible carbonaceous materials.

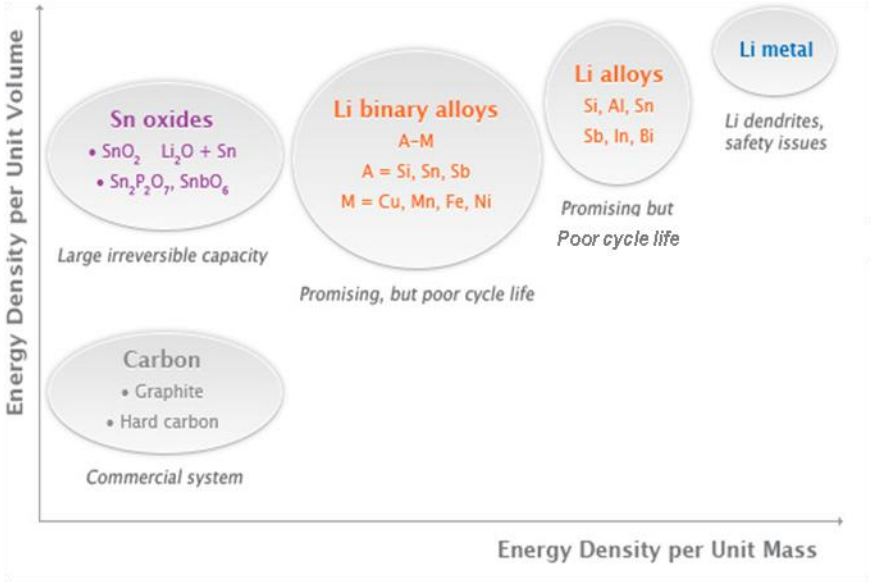

Figure 1.4. Current issues remaining in different types of anode materials.

Bibliography of Chapter 1

[1] M. Winter, R. J. Brodd, *Chem. Rev* **2004**, *104*, 4245.

[2] B. E. Conway, Electrochemical Supercapacitors: Scientific Fundamentals and Technological Applications **1999**.

[3] The plot shown here is based on the data provided by Maxwell Technologies: http://www.maxwell.com.

[4] Alkaline Manganese Dioxide Handbook and Application Manual, **2008**.

[5] J. M. Tarascon, M. Armand, *Nature* **2001**, *414*, 359.

[6] T. Ikeda, H. Tamura, Proc. Manganese Dioxide Symp. **1975,** Vol. 1, (IC sample Office, Cleveland, OH).

[7] M. S. Whittingham, *Science* **1976**, *192***,** 1226.

[8] M. S. Whittingham, US Patent 4009052.

[9] F. Orsini, *et al.*, *J. Power Sources* **1999**, *81***,** 918.

[10] K. Mizushima, P. C. Jones, P. J. Wiseman, J. B. Goodenough, *Mat. Res. Bull.***1980**, *15***,** 783.

[11] M. M. Thackeray, W. I. F. David, P. G. Bruce, J. B. Goodenough, *Mat. Res. Bull.* **1983**, *18***,** 461.

[12] D. W. Murphy, F. J. DiSalvo, J. N. Carides, J. V. Waszczak, Mat. Res. Bull. **1978**, *13***,** 1395.

[13] M. Lazzari, B. Scrosati, *J. Electrochem. Soc.***1980**, *127*, 773.

[14] M. Mohri, *et al.*, *J. Power Sources* **1989**, *26*, 545.

[15] J. R. Dahn, U. V. Sacken, M. W. Juzkow, H. Al-Janaby, *J. Electrochem.*

Soc. **1991**, *138*, 2207.

Outline of Chapter Two

Carbonaceous Materials as an Anode of Li-Ion Battery

CHAPTER TWO

Carbonaceous Materials as an Anode of Li-Ion Battery

2.1 Operation Mechanism of Li-Ion Battery

Carbon as one of the most abundant elements on earth plays a critical role in the development of human society. For thousands of years, human history is closely associated with the struggle to extract and utilize the power from carbon materials. Carbonaceous materials have been adopted in various electrochemical energy storage systems previously. This was motivated by the good electrical conductance of sp^2-hybridized solid carbon, its high chemical stability, and its enormous adaptability to different interface processes [1]. Li-ion battery is one typical example to utilize the carbonaceous materials in energy storage devices. Commercialized LIB usually consists of layered $LiCoO_2$ as a cathode and carbonaceous materials as an anode. These two electrodes are usually separated by a porous polymer membrane and the ionic transport within the cell is ensured by an aprotic organic electrolyte which is a good ionic conductor and electronic insulator [2]. Nowadays, the most common electrolyte is a solution of $LiPF_6$ in a mixture of alkyl carbonates such as ethylene carbonate, diethyl carbonate, and dimethyl carbonate which provides high-permittivity and low-viscosity.

In common Li-ion battery cells, during the charging process, Li ions are extracted from the $LiCoO_2$ electrode (cathode) and simultaneously

inserted/intercalated into the carbon electrode (anode) by forming a lithium/carbon intercalation compound indicated as Li_xC_n, coupled with negatively charged electrons to keep overall charge neutrality, as shown on the left side of **Figure 2.1**. During the discharging process, Li ions are reversibly extracted/deintercalated from the negative electrode and simultaneously inserted into the positive electrode, as shown on the right side of **Figure 2.1**. This charge/discharge process can be summarized by the typical chemical equations as shown below [3]:

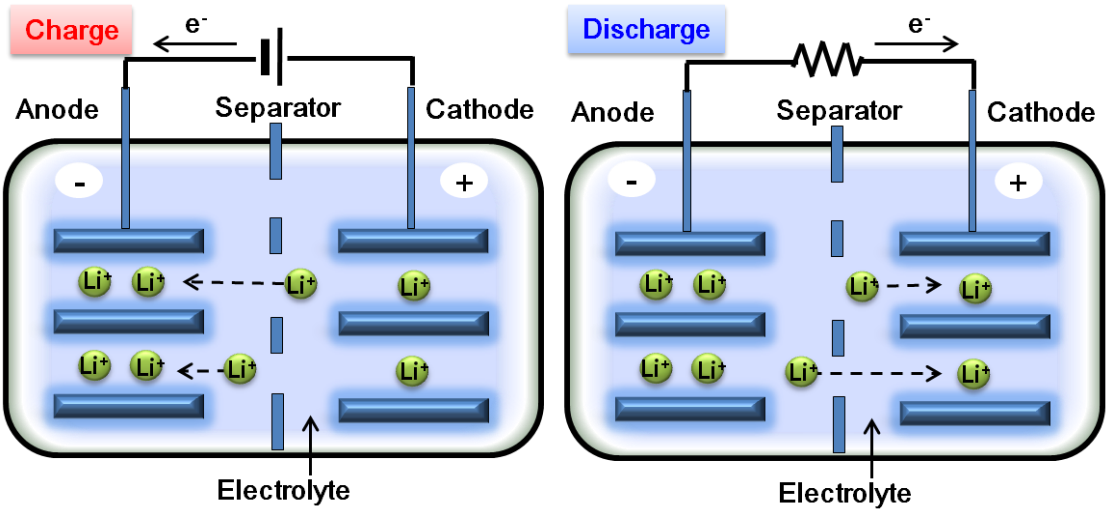

Figure. 2.1. Schematic illustration of detailed charge/discharge process in Li-ion battery.

Positive Electrode: $LiCoO_2 \leftrightarrow Li_{1-x}CoO_2 + xLi^+ + xe^-$

Negative Electrode: $C_n + xLi^+ + xe^- \leftrightarrow Li_xC_n$

Overall: $LiCoO_2 + C_n \leftrightarrow Li_{1-x}CoO_2 + Li_xC_n$

Compared to ECs whose electrodes are composed of same materials which therefore exhibit the same potential, an inherent potential difference exists between $LiCoO_2$ and carbonaceous material in LIB, as simply indicated in **Figure 2.2**. The original potentials of $LiCoO_2$ and carbon materials are usually ~ 4 V and ~ 0.2-0.5 V (depending on types of carbon) vs. Li/Li^+, respectively [2,4]. During the charge process, the cathode will release Li^+ under the influence of external power and the potential of cathode will increase to 4.2 V, whereas the anode potential will decrease to approximately 0.01 V vs. Li/Li^+ upon Li ion insertion, thus delivering an output voltage of nearly 4 V to the external load. Here, the cut off voltage of $LiCoO_2$ and graphite is usually limited to 4.2 (corresponding to a removal of 0.5 mol Li) and 0.01 V in order to maintain the structural stability [5]. On the other hand, during the spontaneous discharge process, $Li_{0.5}CoO_2$ needs to go back to its original potential state which is more energetically stable therefore Li ions go back to $Li_{0.5}CoO_2$ and the electrode potential goes back to the original state, and the system is thus ready for the next charge process.

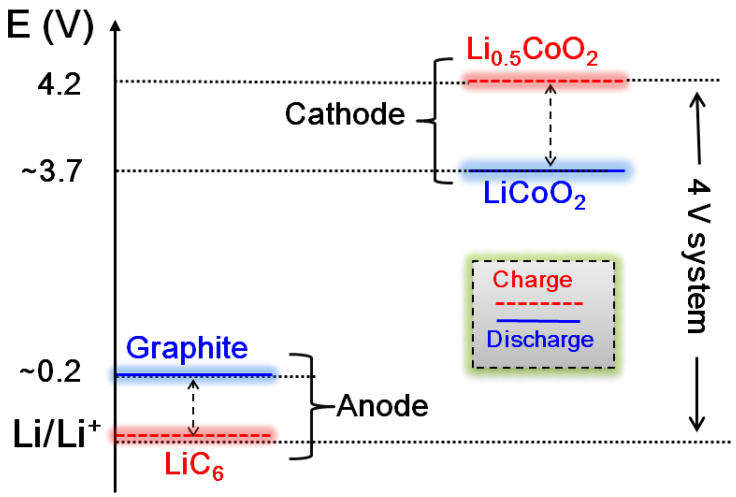

Figure 2.2. Potential profile of anode and cathode during charge/discharge.

The discovery of different carbon allotropes associated with nanoscience and nanotechnology provided us a room to further improve the performance of anode material. Therefore, carbonaceous material used as an anode in LIB is chosen to be the main focus in this work. Before moving to the details, we summarize one more time the advantages of carbon-based anode material. Compared to transition-metal oxides and chalcogenides, carbonaceous materials such as graphite and hard carbons are more preferable not only because of (1) the unstable inherent nature of the transition-metal oxides and chalcogenides materials as mentioned at the end of Chapter 1 and (2) the dimensional stability and good conductivity of carbonaceous materials, but also (3) the lowest potential versus Li/Li^+ which gives higher output cell voltage compared to other composite alloys, three dimensional metal oxides and so on. For instance, the potential of many Li alloys is ~0.3 to ~1.0 V vs. Li/Li^+ whereas it is only ~0.1 V vs. Li/Li^+ for graphite, as indicated in **Figure 2.3** [6].

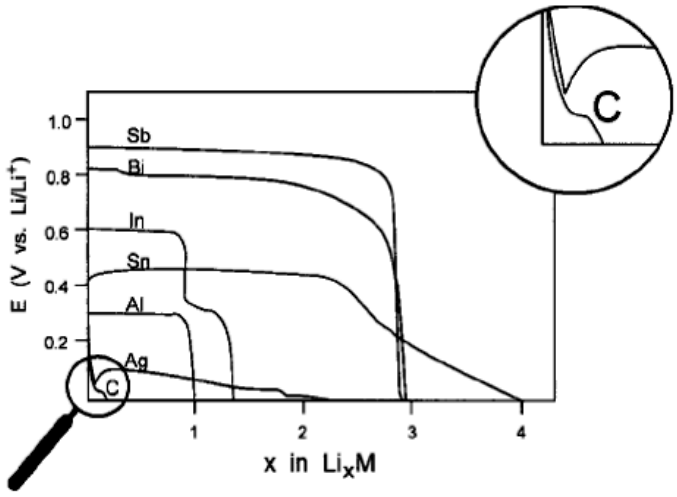

Figure 2.3. Charge curves of different metals (M) with respect to highly oriented turbostratic pitch carbon fibers. Cited from Ref. [6].

One good carbonaceous anode material needs to fulfill high capacity, long cycle life, fast charge etc. in addition to high energy/power density, good conductivity and stability, as mentioned above. A charge/discharge curve can be used as one of the most straightforward tools to demonstrate the storage capability, cyclic ability, rate of charge/discharge. The charge/discharge curve (capacity-voltage curve) is converted from a voltage-time profile with one or several constant current densities that are fixed in advance. The capacity (mAh) therefore equals to the current (mA) multiply the time (h). The charge/discharge curve usually exhibits very different features according to the structure of carbon materials. Thus, in order to further improve the performance of carbonaceous anode and to assist in explaining the phenomenon of nanocarbon-based anode later, the classification of carbon materials upon the structure and also their

associated charge/discharge profiles need to be elaborated first. The related topics are explained in detail in the following section.

2.2 Classification of Carbonaceous Materials

Carbonaceous materials that are capable of reversible lithium reaction can be roughly classified into two categories according to their structures: graphitic and non-graphitic (disordered) carbon. The non-graphitic carbon can be further categorized into soft carbon/hard carbon upon annealing and high specific charge carbon/low specific charge carbon according to the capability of reversible lithium storage. Charge/discharge behaviors of each type of carbon are presented and analyzed in detail in the following context.

2.2.1 Graphitic Carbon

Graphitic carbon is a well-defined layered structure. Normally, a number of structural defects could appear in graphitic carbon. The term of "graphite" was derived from crystallographic point of view which should be only applied to carbons whose layered lattice structure follows a perfect stacking order of graphene layers. That is to say it contains the layer stacking order of either the common AB (hexagonal graphite, **Figure 2.4** and **Figure 2.5a**) or the rather rare ABC (rhombohedral graphite). However, since the transformation energy from AB stacking to ABC stacking (and vice versa) is rather small, perfectly stacked graphite crystals are not readily available. Therefore the term of "graphite" is

often used regardless of well-defined stacking order [7]. The terms of natural graphite, artificial graphite, and pyrolytic graphite are commonly used, although the materials are polycrystalline [8]. The actual structure of carbonaceous materials typically deviates more or less from the ideal graphite structure. Materials consisting of aggregates of graphite crystallites are called graphites as well.

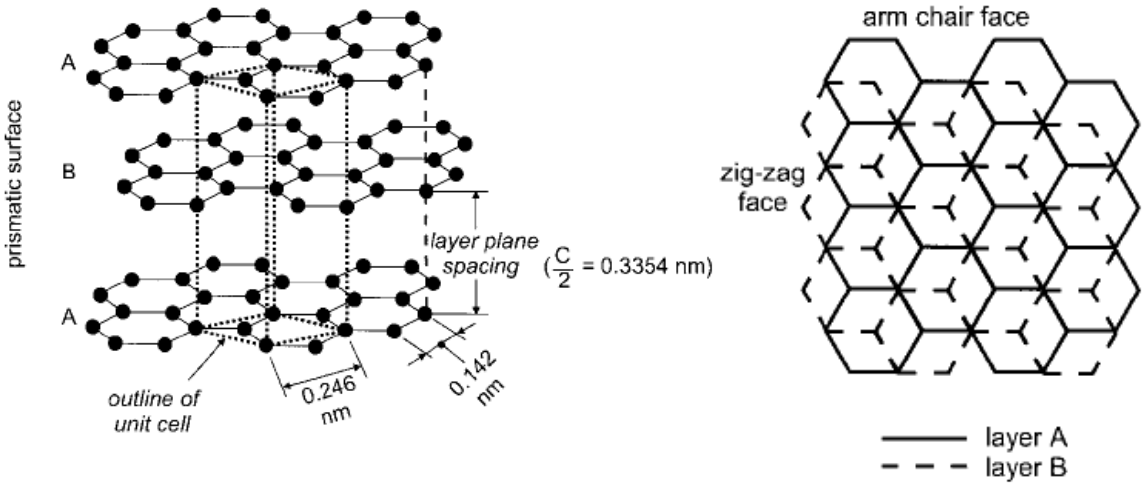

Figure 2.4. Left: Schematics of the crystal structure of hexagonal graphite with an AB stacking order. Right: view perpendicular to the basal plane of graphite. Edges can be subdivided into arm-chair and zigzag faces. Cited from Ref. [7].

2.2.2 Non-Graphitic Carbon

Non-graphitic (disordered) carbonaceous materials consist of carbon atoms that are mainly arranged in a planar hexagonal network but no crystallographic order in the c-direction compared to graphite, as shown in **Figure 2.5c** [7,9]. The

structure of those carbons is characterized by amorphous areas embedded and cross-linked in the network. Non-graphitic carbons are mostly prepared by pyrolysis of organic polymer or hydrocarbon precursors at temperature below ~1500°C [10-12].

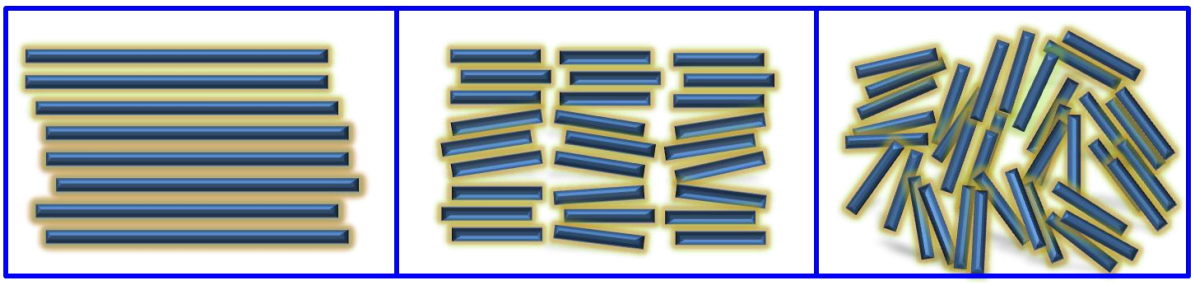

(a) graphite **(b) graphitizable carbon** **(c) non-graphitizable carbon**

Figure 2.5. Schematic indications of (a) graphite and (b) non-graphitic (disordered) carbonaceous material.

Heat treatment of most non-graphitic carbons (from ~1500 to ~3000°C) allows us to further classify non-graphitic carbon into two sub-categories: soft carbon and hard carbon. In the case of soft carbons, crosslinking between the carbon layers is weak and therefore the layers are mobile enough to form graphite-like crystallites and develop the graphite structure continuously during the heating process, as shown in **Figure 2.5b** [9]. In the case of hard carbons, since the carbon layers are immobilized by crosslinking, they show no real development of the graphite structure even at temperatures of 2500 ~ 3000 °C [10]. The representative figure is shown in **Figure 2.5c**.

2.3 Lithium Intercalation into Carbonaceous Materials

2.3.1 Lithium Intercalation into Graphitic Carbon Materials

2.3.1-1 Description

Lithium-intercalated graphitic carbon compounds (GICs) are known with the configuration Li_xC_n. It is well known that Li intercalation reaction occurs only at the edge plane of graphite. Through the basal plane, intercalation is possible only at defect sites [13-16]. The maximum lithium content for highly crystalline graphitic carbons is one Li guest atom per six carbon host atoms (i.e. $n \geq 6$ in LiC_n or $x \leq 1$ in Li_xC_6) at ambient pressure [17]. That is to say it follo ws the equation as below:

$6\,C + x\,Li^+ + x\,e^- \rightarrow Li_xC_6$, where, $x = 1$ in Li_xC_6 (the maximum Li conte nt).

In LiC_6, lithium avoids to occupy the nearest neighbor sites due to the Columbic repulsive force of Li, as shown in **Figure 2.6**. Two major changes in graphite structure point of view occur when Li intercalats into graphite layers: (1) the stacking order of the carbon layers (i.e. graphene layers) shifts to AA stacking, see **Figure 2.6a** and **Figure 2.6c**. (2) The interlayer distance between the graphene layers increases moderately (10.3% has been calculated for LiC_6) due to the lithium intercalation, as indicated in the right panel in **Figure 2.6a** [18-21].

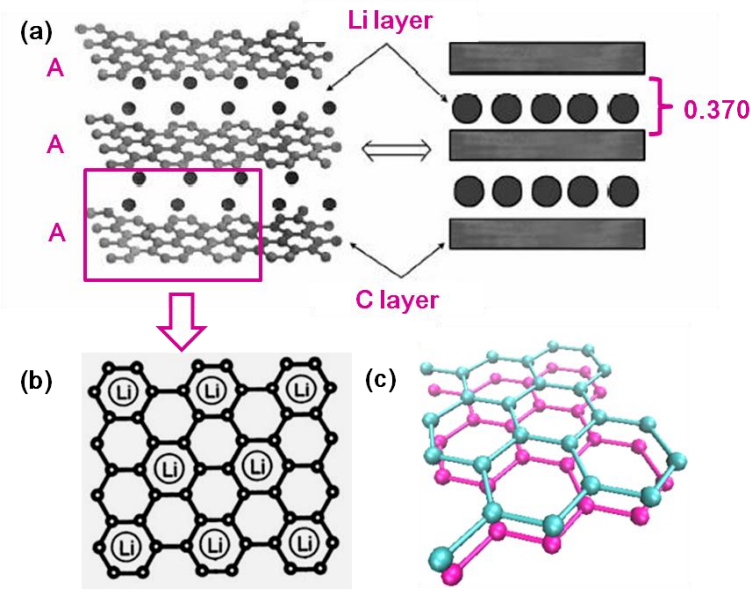

Figure 2.6. Structure indications of LiC_6. (a) Left: schematic drawing showing the AA layer stacking sequence with Li intercalation. Right: simplified representation. (b) Perpendicular view to the basal plane of LiC_6. (c) Enlarged schematic of AA stacking order. Cited and modified from Ref. [20-21].

An important feature of Li intercalation into graphite is the "stage formation". Stage formation means a stepwise formation of a periodic pattern of unoccupied graphitic layer gaps at low concentrations of Li [23-31]. This stepwise process can be described by the stage index, *s* (*s* = I, II, III, IV) which is equal to the number of graphene layers between two nearest guest layers as shown in **Figure 2.7. N**ote that stage IV is not indicated in the figure because Li concentration is too low in graphene layers. It is also known as a dilute stage

when s > IV [32]. Two factors determine the formation of stages during Li intercalation into graphite i) the energy required to expand van der Waals gap between two graphene layers [31,33] and ii) the repulsive interactions between guest species. Therefore, compared to a random distribution of Li in the graphitic layers during charge process, Li ions prefer to occupy van der Waals gaps with high density first to reach an energetically stable state [7].

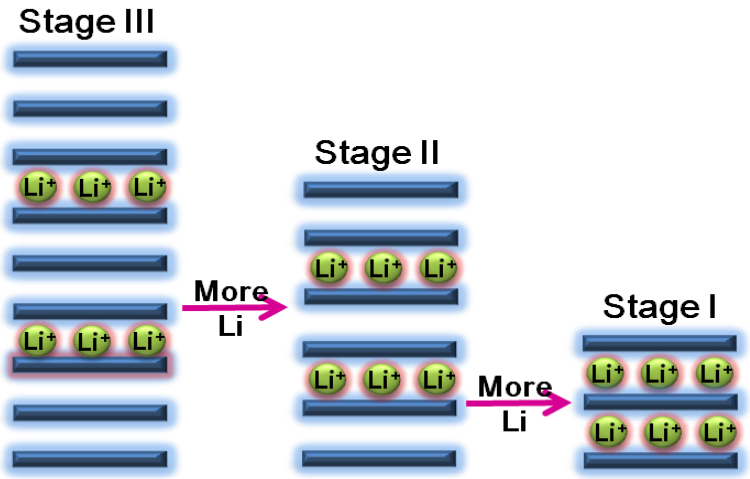

Figure 2.7. Schematic indication of stage formation during Li ion intercalation into graphite layers.

2.3.1-2 Charge/Discharge Profile of Graphitic Carbon Materials

Stage formation as mentioned above is one of the most important characteristic of charge profile for graphitic carbon. It can be easily observed in the form of plateaus by constant current measurement (i.e. in charge/discharge curve), as indicated in **Figure 2.8.** The associated stages are marked in bottom

panel of the figure. The plateaus indicate the coexistence of two phases [24,34]. The formation of stages II, IIL (a transition stage of stage II and stage III), III, and IV have been identified from experimental electrochemical curves [18,35,37-40] and confirmed by X-ray diffraction and Raman spectroscopy [17,25,27-28,35-38]. A schematic potential / composition curve for galvanostatic reduction of graphite to LiC_6 is shown in the bottom panel in **Figure 2.8**.

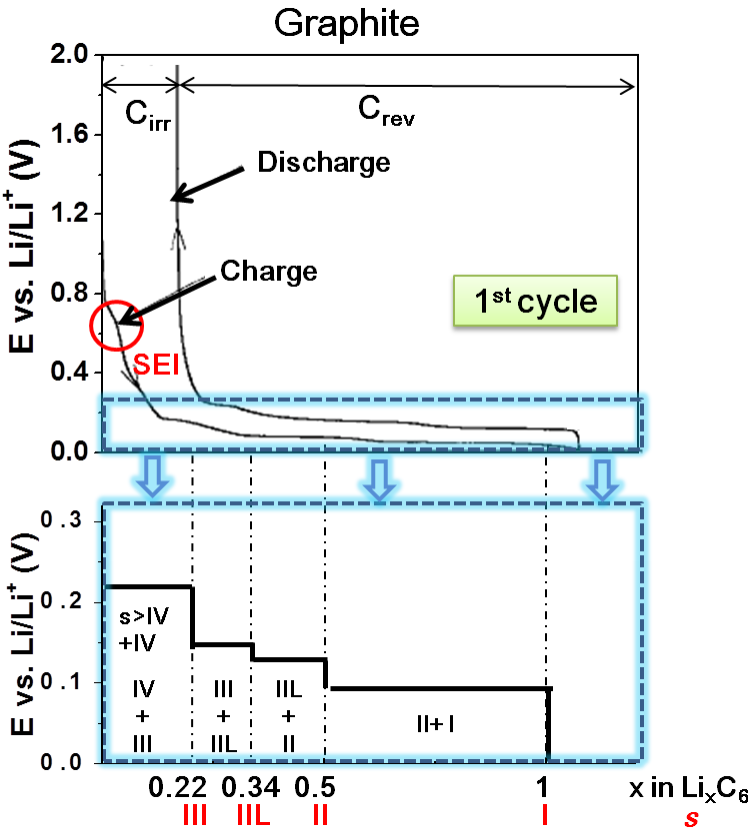

Figure 2.8. Constant current charge/discharge curves of the graphite (Timrex KS 44, C_{irr} is the irreversible specific charge, and C_{rev} is the reversible specific charge). Modified and replotted from Ref. [7].

Ideally, Li^+ intercalation into carbons should be fully reversible and the maximum Li storage capacity should not exceed 372 mAh/g according to LiC_6 configuration. However, the charge accumulated in the first cycle usually larger than the maximum theoretical specific capacity, as shown in **Figure 2.8**. Compared to the first charge, the first discharge capacity is much smaller. The excess charge generated in the first cycle which cannot be recovered can be ascribed to a film formation of the solid electrolyte interface (SEI) which is caused by the decomposition of the Li^+ containing electrolyte, such as propylene carbonate and ethylene carbonate [41-46]. The decomposition of electrolyte usually takes place at less than 1 V vs. Li/Li^+ and appears as the first plateau in the charge curve, as indicated in **Figure 2.8** [47]. The advantage of the SEI formation is that it can prevent further electrolyte decomposition and create a rather stable state for the surface of GIC [48-53]. On the other hand, the formation of SEI is a charge-consuming side reaction in the first few Li^+ intercalation/deintercalation cycles, especially in the 1^{st} charge cycle. Considering that the positive electrode is responsible to provide the Li ion in LIB, the charge and lithium losses are detrimental to the specific energy of the whole cell and have to be minimized. Because of the irreversible consumption of lithium and electrolyte, a corresponding charge loss exists, so called “irreversible specific charge” as indicated in **Figure 2.8**. The reversible lithium intercalation is called “reversible specific charge”.

2.3.2 Lithium Intercalation into Non-Graphitic Carbon Materials

According to the capability of reversible lithium storage, non-graphitic carbons can be further classified into two categories: high specific charge carbon and low specific charge carbon.

2.3.2-1 Low Specific Charge Carbon

(i) Definition

Low specific charge carbons are carbonaceous materials which incorporate only a considerably lower amount of lithium than graphite. That is to say it follo ws the equation as below:

$6C + xLi^+ + xe^- \rightarrow Li_xC_6$, where $x = 0.5 \sim 0.8$ in Li_xC_6 at the maximum stoichiometry.

(ii) Examples of Low Specific Charge Carbon

Cokes [68,77-83] and carbon blacks [81,84-85] are typical disordered carbons with low specific charges. During the charge process, Li intercalation-induced formation of AA stacking is hindered due to the existence of crosslinking of carbon sheets as mentioned in chapter 2.1.2. This will eventually affect the accommodation of a higher Li amount into graphitic sites and deliver a lower specific charge [86-88].

Turbostratic carbon [43,86-90] which can also be classified into the category of graphitizing/soft carbon is one type of low specific charge carbon. The lower amount of Li intercalation than graphite is due to not only the effect of crosslinking as mentioned in cokes and carbon blacks, but also larger amount of wrinkled and buckled structural segments existing in the structure, and thus available lithium intercalation sites is rather low therefore the specific charge is lower than graphite [91-92].

(iii) Charge/Discharge Profile of Low Specific Charge Carbon

Figure 2.9 shows the first Li^+ intercalation/deintercalation cycle of a coke-containing electrode. The potential profile of low specific carbon differs considerably from that of graphite, as the reversible intercalation of Li^+ begins at around 1.2 V vs. Li/Li^+, and the curve slopes without distinguishable plateaus. This behavior is a consequence of the disordered structure providing electronically and geometrically nonequivalent sites, whereas for a particular intercalation stage in highly crystalline graphite, the sites are equivalent [93-94].

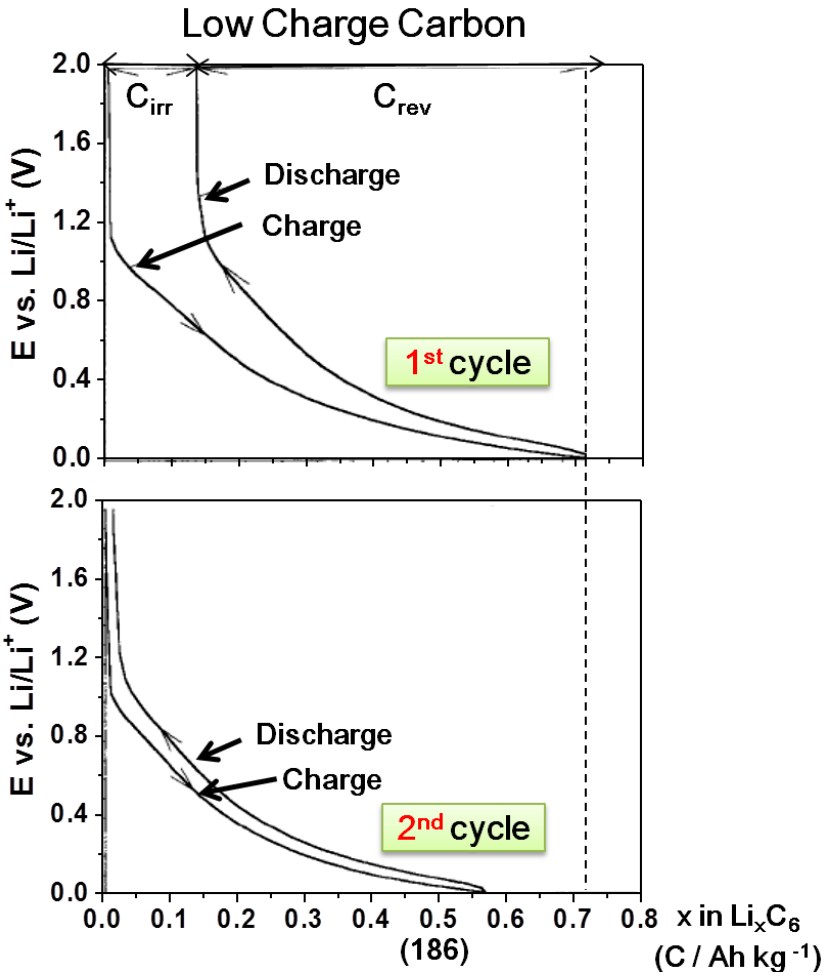

Figure 2.9. Constant current charge/discharge curves of a coke (Conoco). (C_{irr} is the irreversible specific charge, C_{rev} the reversible specific charge). Cited and redrawn from Ref. [7].

2.3.2-2 High Specific Charge Carbon

(i) Definition

High specific charge carbons can store more lithium than graphite. That is to say it follows the equation as below:

$6\ C + x\ Li^+ + x\ e^- \rightarrow Li_xC_6$, where $x > 1$ in Li_xC_6.

Li storage capacity of high specific charge carbons could vary from 400 Ah/kg to ~2000 Ah/kg which corresponding to x = ~1.2 to ~5 in Li_xC_6. The difference in the capacity depends on the heat treatment temperature, organic precursor, and electrolyte. Even though the higher specific capacity (in terms of Ah/kg) is desired in LIB, a larger volume of the carbonaceous matrix is usually needed to accommodate the excess intercalated Li which indicates lower charge density in terms of Ah/L [7].

(ii) Origin of the Excess Charges

Several different scenarios have been proposed in order to explain origin of excess charges. These different models provide the intuitive understanding even though some of them are still debatable [54-58]. A few well known examples are listed below. Extra capacity can be realized through: (1) The formation of Li_2 molecules between layers which indicates that lithium molecules occupy the nearest neighbor sites in intercalated carbons [59]. (2) The presence of charged Li^+ clusters in the cavities [60]. (3) The "adsorption" of lithium on both sides of single-layer sheets that are arranged like a "falling cards" [61]. All of mechanisms are indicated in **Figure 2.10**.

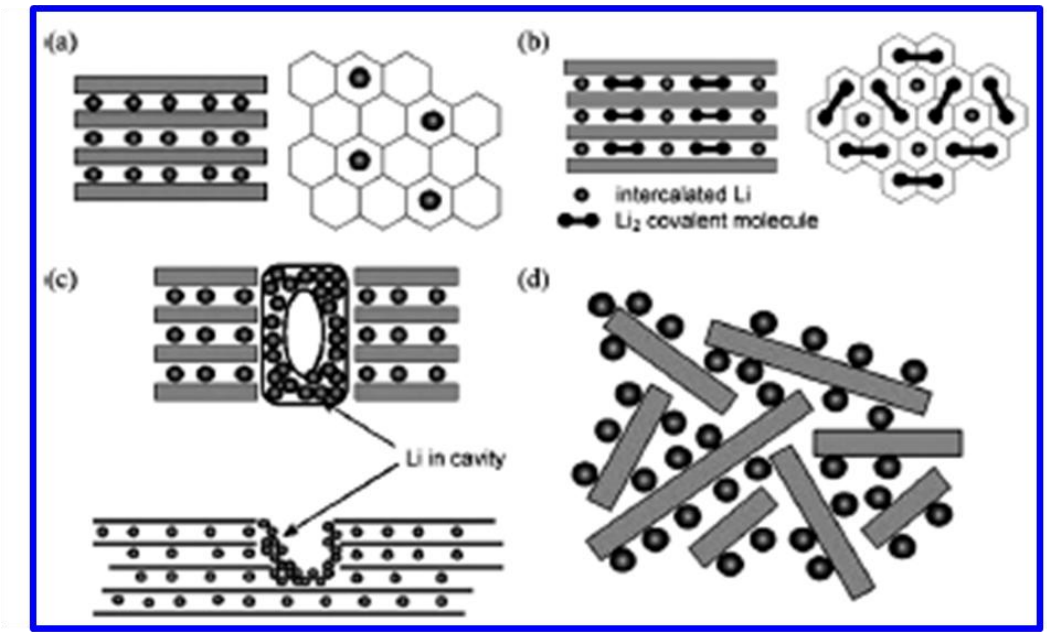

Figure 2.10. a) Storage mechanisms of Li ions in graphite. b) Li storage in a form of Li_2 covalent molecules. c) Schematic model of Li storage in cavities and nanopores. d) Li adsorption on the two sides of an isolated graphene sheet. Cited from Ref. [3].

(iii) Charge/discharge Profile of High Specific Charge Carbon

For both graphitizing (soft) and non-graphitizing (hard) carbons prepared < 1000 ^{o}C, the typical charge/discharge profile is shown in **Figure 2.11**.

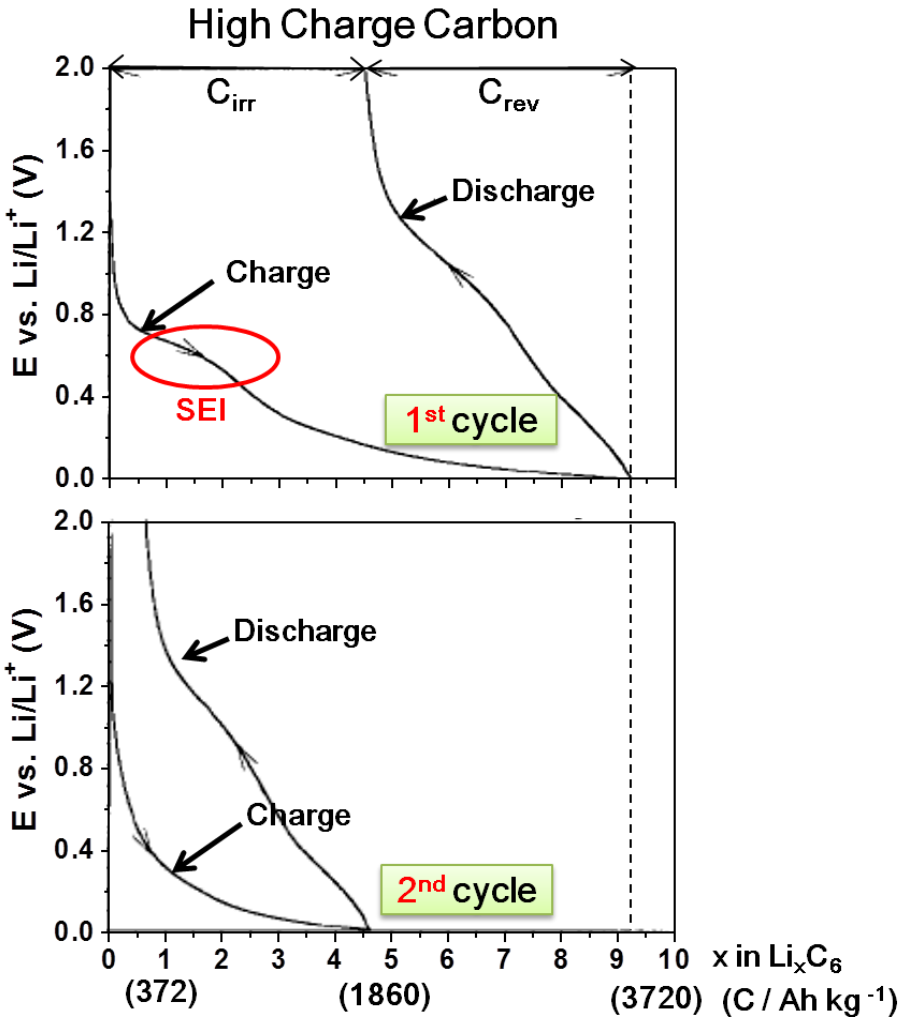

Figure 2.11. Constant current charge/discharge curves (1st and 2nd cycle) of a high specific charge carbon material after heat treatment at 700 °C. (C_{irr} is the irreversible specific charge, C_{rev} the reversible specific charge). Cited and redrawn from Ref. [7].

It is clear to see a SEI-related plateau appears at around 0.6V and a high specific charge of around 3720 Ah/kg was achieved during the first charge, as

shown in the top panel in **Figure 2.11**. The special feature of this kind of carbon material is that it exhibits a larger voltage hysteresis between charge and discharge processes compared to that of graphite (**Figure 2.8**). To be more specific, the second charge/discharge is shown at the bottom of **Figure 2.11** which does not show the effect of SEI. The potential for Li insertion is close to 0 V vs. Li/Li^+ whereas the one for Li de-insertion is much more positive [54-55,62-65] in the second charge/discharge process. According to the previous study, it has been shown that the extent of hysteresis is proportional to the hydrogen content in the carbon since Li is somehow bound near the hydrogen [66-67].

Since hydrogen can be removed with increasing temperature, the specific charges achieved after the removal of hydrogen need to be evaluated. It was found that the value of specific charge after high temperature annealing strongly depend on the structure of the non-graphitic material [55,65,68-75]. (i) In the case of soft carbon, it will deliver a lower value of specific charge ($x < \sim 0.5$ in Li_xC_6) which is similar to the low specific charge carbon [54,75-76], when heat treated at ~1000 °C. And the specific charge again increases when the temperature is > 1000 °C [73,74]. (ii) In the case of hard carbon, it can still display a specific charge of several hundred Ah/kg when heat-treated at ~1000 °C. But Li inserts at a very low potential of a few millivolts versus Li/Li^+ and a smaller hysteresis is shown in charge/discharge profile. In contrast to soft carbon, a drastically reduction of specific charge is observed when the temperature is >

1000 °C [72,76].

Although the high specific charge carbons show much higher specific capacity than graphite, they have some serious drawbacks such as higher irreversible specific charges, larger hysteresis and poorer cycling performance than graphite [54-55,62,95-96,98,100-101,103-104]. Although the cycling performance of non-graphitizing (hard) carbons heat-treated at ~1000 °C is reasonable and almost no hysteresis occurs, the end of the charge potential of the carbons is very close to metallic lithium [62,75,102]. Under such a charging regime, lithium deposition occurs, which will induce safety issue like Li-metal battery [7].

2.4 Summary of Chapter Two

The operation mechanism of Li-ion battery and the charge/discharge behavior based on different types of carbonaceous materials were generally reviewed in this chapter. This kind of information provides fundamental knowledge to characterize and understand the anodic behavior of nanoscaled carbon materials which will be covered in Chapter 3.

Based on this chapter, it is clear to see that there are so many unsolved issues related to carbonaceous materials. In the case of graphite, it exhibits good cyclic performance and structure stability but the capacity is limited. On the

contrary, in the case of high specific carbon, the capacity is higher than that of graphite but the long time stability and safety issues remain unsolved.

Although the current understanding of the origins of excess charge is limited, it is clear that numerous factors such as surface area, crystallinity, defect population, basal/edge plane effects and so on could affect the storage capacity. Compared to graphite, the analysis of non-graphitic carbon is more complicated since so many unpredictable factors exist. Ahead of understanding of Li storage mechanisms and the realization of high capacity anode materials, one preliminary issue still remains unclear, that is the Li diffusion pathway in carbonaceous materials. Therefore, further understanding of Li diffusion pathway through graphene plane and the role of defects in Li diffusion is highly required to provide more information to reveal the mystery of Li-C system. In order to improve the limited capacity of graphite and also to overcome various problems in non-graphitic carbons, incorporation of a second material which contains higher Li storage capacity on rather stable carbon matrix could be an alternative way to satisfy the requirements on anode part. The related issues will be further discussed in Chapter 4.

Bibliography of Chapter Two

[1] S. L. Candelaria, Y. Y. Shao, W. Zhou, X. L. Li, J. Xiao, J. G. Zhang, Y. Wang, J. Liu, J. H. Li, G. Z. Cao, *Nano Energy* **2012**, *1*,195.

[2] J. M. Tarascon, M. Armand, *Nature* **2001**, *414*, 359.

[3] D. S. Su, R. Schlögl, *ChemSusChem* **2010**, *3*, 136.

[4] B. Xu, D. Qian, Z. Wang, Y. Meng, *Materials Science and Engineering R* **2012**, *73*, 51..

[5] T. Ohzuku, A. Ueda, N. Nagayama, Y. Iwakoshi, H. Komori, *Electrochim Acta* **1993**, *38*, 1159.

[6] J. O. Besenhard, J. Yang, M. Winter, *J. Power Sources* **1997**, *68*, 87.

[7] M. Winter, J. O. Besenhard, M. E. Spahr, P. Novák, *Adv. Mater.* **1998**, *10*, 725

[8] H. O. Pierson, *Handbook of Carbon, Graphite, Diamond and Fullerenes*, Noyes, Park Ridge, NJ **1993**, 43.

[9] I. Mochida, S. Yoon, W. Qiao, *J. Braz. Chem. Soc.* **2006**, *17 (6)*, 1059.

[10] R. E. Franklin, Proc. R. *Soc. London A* **1951**, *209*, 196..

[11] K. Kinoshita, *Carbon: Electrochemical and Physicochemical Properties* **1987** Wiley, New York..

[12] K. Inada, K. Ikeda, Y. Sato, A. Itsubo, M. Miyabashi, H. Yui, *in Primary and Secondary Ambient Temperature Lithium Batteries* (Eds: J.-P. Gabano, Z. Takehara, P. Bro), Electrochemical Society, Pennington, NJ **1988**, *88-6*, 530.

[13] T. Tran, K. Kinoshita, *J. Electroanal. Chem.* **1995**, *386*, 221.

[14] K. Persson, A. V. Sethuraman, J. L. Hardwick, Y. Hinuma, S. Y. Meng,

A. Ven, V. Srinivasan, R. Kostecki, G. Ceder, *Phys. Chem. Lett.* **2010**, *1*, 1176.

[15] T. Placke, V. Siozios, R. Schmitz, S. F. Lux, P. Bieker, C. Colle, H.-W. Meyer, S. Passerini, M. Winter, *J. Power Sources* **2012**, *200*, 83.

[16] B. Jungblut, E. Hoinkis, *Phys. Rev. B* **1989**, *40*, 10810.

[17] T. D. Tran, K. Kinoshita, *J. Electroanal. Chem.* **1995**, *386*, 22.

[18] D. Billaud, E. McRae, A. Hérold, *Mater. Res. Bull.* **1979**, *14*, 857.

[19] X. Y. Song, K. Kinoshita, T. D. Tran, *J. Electrochem. Soc.* **1996**, *143*, L120.

[20] H. H. Lee, C. C. Wan, Y. Y. Wang, *Journal of Power Sources* **2003**,*1*,7.

[21] C. Casas, W. Li, *Journal of Power Sources* **2012**, *208*, 74.

[22] E. Jomehzadeh, A. R. Saidi, N. M. Pugno, *Physica E: Low-dimensional Systems and Nanostructures* **2012**, *44 (10)*, 1973.

[23] J. O. Besenhard, H. P. Fritz, *Angew. Chem. Int. Ed.* **1983**, *95*,950.

[24] A. Hérold, *Chemical Physics of Intercalation* **1987** (Eds: A. P. Legrand,S. Flandrois), NATO ASI Series B, *172*, 3.

[25] A. Hérold, *Bull. Soc. Chim. Fr.* **1955**, *187*, 999.

[26] W. Rüdorff, U. Hofmann, Z. Anorg. *Allg. Chem.* **1938**, *238*, 1.

[27] N. Daumas, A. Hérold, C. R. Acad. *Sci. Paris* **1969**, *268C*, 373.

[28] N. Daumas, A. Hérold, *Bull. Soc. Chim.* **1971**, 5, 1598.

[29] L. B. Ebert, *Annu. Rev. Mater. Sci.* **1976**, *6*, 181.

[30] W. Rüdorff, *Advances in Inorganic Chemistry and Radiochemistry* **1959**,

(Eds: H. J. Emeléus, A. G. Sharpe), Academic, New York, *1*, 223.

[31] R. Schlögl, *Progress in Intercalation Research* **1994** (Eds: W. Müller-Warmuth, R. Schöllhorn), Kluwer, Dordrecht, The Netherlands, 83.

[32] D. Billaud, F. X. Henry, M. Lelauraint, P. Willmanns, *J. Phys. Chem. Solids* ***1996 ,*** *l57*(6-8), 775.

[33] J. O. Besenhard, M. Winter, *Proc. of the 2. Ulmer Elektrochemische Tage, Ladungsspeicherung in der Doppelschicht* **1995** (Ed: W. Schmickler), Universitätsverlag Ulm, Germany, 47.

[34] J. R. Dahn, *Phys. Rev. B* **1991**, *44*, 9170.

[35] J. E. Fisher, *Chemical Physics of Intercalation* **1987** (Eds: A. P. Legrand, S. Flandrois), NATO ASI Series B, *172*, 59.

[36] M. Bagouin, D. Guerard, A. Hérold, C. R. Acad. *Sci. Paris* **1966**, *262C*, 557.

[37] C. Casas, W. Li, *Journal of Power Sources* **2012**, *208*, 74.

[38] P. Pfluger,V. Geiser, S. Stolz, H.-J. Güntherodt, *Synth. Met*. **1981**, *3*, 27.

[39] D. Billaud, F. X. Henry, P. Willmann, *Mater. Res. Bull*. **1993**, *28*, 477.

[40] D. Billaud, F. X. Henry, P. Willmann, *Mol. Cryst. Liq. Cryst.* **1994**, *245*, 159.

[41] J. R. Dahn, A. K. Sleigh, H. Shi, B. M. Way, W. J. Weydanz, J. N. Reimers, Q. Zhong, U. von Sacken, *Lithium Batteries: New Materials, Developments and Perspectives* **1994** (Ed: G. Pistoia), Elsevier, Amsterdam, 1.

[42] R. Fong, U. von Sacken, J. R. Dahn, *J. Electrochem. Soc.* **1990**, *137*,

2009.

[43] K. Yokoyama, N. Nagawa, *New Sealed Rechargeable Batteries and Supercapacitors* **1993** (Eds: B. M. Barnett, E. Dowgiallo, G. Halpert, Y.Matsuda, Z. Takehara), Electrochemical Society, Pennington, NJ, PV93-23, 270.

[44] R. Kanno, Y. Kawamoto, Y. Takeda, S. Ohashi, N. Imanishi, O. Yamamoto, *J. Electrochem. Soc.* **1992**, *139*, 3397.

[45] M. Winter, P. Novμk, A. Monnier, *J. Electrochem. Soc*. **1998**, *145*, 428.

[46] F. Joho, P. Novμk, O. Haas, A. Monnier, F. Fischer, *Mol. Cryst. Liq. Cryst.*, in press.

[47] P. G. Bruce, B. Scrosati, J. M. Tarascon, *Angew. Chem. Int. Ed.* **2008**, *47*, 2930.

[48] S. Mori, H. Asahina, H. Suzuki, A. Yonei, E. Yasukawa, *J. Power Sources* **1997**, *68*, 59.

[49] Y. Ein-Eli, B. Markovsky, D. Aurbach, Y. Carmeli, H. Yamin, S. Luski, *Electrochim. Acta* **1994**, *39*, 2559.

[50] D. Aurbach, Y. Ein-Eli, B. Markovsky, A. Zaban, A. Schechter, S. Luski, Y. Carmeli, H. Yamin, *Rechargeable Lithium and Lithium- Ion Batteries* **1995** (Eds: S. Megahed, B. M. Barnett, L. Xie), Electrochemical Society, Pennington, NJ, PV94-28, 26.

[51] D. Aurbach, Y. Ein-Eli, B. Markovsky, A. Zaban, S. Lusky, Y. Carmeli, H. Yamin, *J. Electrochem. Soc.* **1995**, *142*, 2882.

[52] D. Aurbach, Y. Ein-Eli, O. Chusid, Y. Carmeli, M. Babai, H. Yamin, *J. Electrochem. Soc.* **1994**, *141*, 603.

[53] D. Aurbach, Y. Ein-Eli, *J. Electrochem. Soc*. **1995**, *142*, 1746.

[54] T. Zheng, J. S. Xue, J. R. Dahn, *Chem. Mater*. **1996**, *8*, 389.

[55] T. Zheng, Y. Liu, E. W. Fuller, S. Tseng, U. von Sacken, J. R. Dahn, *J. Electrochem. Soc.* **1995**, *142*, 2581.

[56] L. B. Ebert, *Carbon* **1996**, *34*, 671.

[57] J. R. Dahn, T. Zheng, Y. Liu, J. S. Xue, *Science* **1995**, *270*, 590.

[58] P. Zhou, P. Papanek, C. Bindra, R. Lee, J.E. Fischer, *J. Power Sources* **1997**, *68*, 297.

[59] K. Sato, M. Noguchi, A. Demachi, N. Oki, M. Endo, *Science* **1994**, *264*, 556.

[60] M. Winter, J. O. Besenhard, *Lithium Ion Battery: Fundamentals and Performance* **1998** (Eds.: M. Wahihara, O. Yamamoto), Wiley-VCH, Weinheim.

[61] T. Zheng, W. Xing, J. R. Dahn, *Carbon* **1996**, *34*, 1501..

[62] J. S. Xue, J. R. Dahn, *J. Electrochem. Soc.* **1995**, *142*, 3668.

[63] J. R. Dahn, J. S. Xue,W. Xing, A. M.Wilson, A. Gibaud, *Extended Abstracts of the 8th Int. Mtg. on Lithium Batteries* **1996**, Nagoya, Japan, 89.

[64] T. Zheng, J. R. Dahn, *J. Power Sources* **1997**, *68*, 201.

[65] T. Zheng, W. R. McKinnon, J. R. Dahn, *J. Electrochem. Soc.* **1996**, *143*, 2137.

[66] S. Wang, Y. Zhang, L. Yang, Q. Liu, *Solid State Ionics* **1996**, *86*, 919.

[67] P. Zhou, P. Papanek, R. Lee, J.E. Fisher, W. A. Kamitakahara, *J.*

Electrochem. Soc. **1997**, *144*, 1744.

[68] A. Satoh, N. Takami, T. Ohsaki, *Solid State Ionics* **1995**, *80*, 291.

[69] A. Satoh, N. Takami, T. Ohsaki, M. Kanda, *Rechargeable Lithium and Lithium-Ion Batteries* **1995** (Eds: S. Megahed, B. M. Barnett, L. Xie), Electrochemical Society, Pennington, NJ, PV94-28,143.

[70] K. Tatsumi, A. Mabuchi, N. Iwashita, H. Sakaebe, H. Shioyama, H. Fujimoto, S. Higuchi, *Batteries and Fuel Cells for Stationary and Electric Vehicle Applications***1993** (Eds: A. R. Landgrebe, Z. Takehara) Electrochemical Society, Pennington, NJ, PV 93-8, 64.

[71] A. Mabuchi, H. Fujimoto, K. Tokumitsu, T. Kasuh, *J. Electrochem. Soc.* **1995**, *142*, 3049.

[72] K. Tokumitsu, A. Mabuchi, H. Fujimoto, T. Kasuh, *Rechargeable Lithium and Lithium-Ion Batteries***1995** (Eds: S. Megahed, B. M. Barnett, L. Xie), Electrochemical Society, Pennington, NJ, PV94-28,136.

[73] K. Tatsumi, T. Akai, T. Imamura, K. Zaghib, N. Iwashita, S. Higuchi,Y. Sawda, *J. Electrochem. Soc.* **1996**, *143*, 1923.

[74] K. Tatsumi, N. Iwashita, H. Sakaebe, H. Shioyama, S. Higuchi, A. Mabuchi, H. Fujimoto, *J. Electrochem. Soc.* **1995**, *142*, 716.

[75] Y. Liu, J. S. Xue, T. Zheng, J. R. Dahn, *Carbon* **1996**, *34*, 193.

[76] H, Iomoto, A. Omaru, A. Azuma, Y. Nishi, *Lithium Batteries* **1993** (Eds: S. Surampudi, V. R. Koch), Electrochemical Society, Pennington, NJ, PV93-24, 9.

[77] J. R. Dahn, A. K. Sleigh, H. Shi, J. N. Reimers, Q. Zhong, B. M. Way,

Electrochim. Acta **1993**, *38*, 1179.

[78] M. Jean, C. Desnoyer, A. Tranchant, R. Messina, *J. Electrochem. Soc.* **1995**, *142*, 2122.

[79] R. V. Moshtev, P. Zlatilova, B. Puresheva, V. Manev, *J. Power Sources* **1995**, *56*, 137.

[80] J. M. Chen, C. Y. Yao, C. H. Cheng, W. M. Hurng, T. H. Kao, *J. Power Sources* **1995**, *54*, 494.

[81] A. K. Sleigh, U. von Sacken, *Solid State Ionics* **1992**, *57*, 99.

[82] S. Ma, J. Li, X. Jing, F. Wang, *Solid State Ionics* **1996**, *86-88*, 911.

[83] R. Alcµntara, J. M. JiminØz-Mateos, P. Lavela, J. Morales, J. L. Tirado, *Mater. Sci. Eng.* **1996**, *B39*, 216.

[84] K. Takei, N. Terada, K. Kumai, T. Iwahori, T. Uwai, T. Miura, *J. Power Sources* **1995**, *55*, 191.

[85] K. Takei, K. Kumai, Y. Kobayashi, H. Miyashiro, T. Iwahori, T. Uwai, T. Miura, *J. Power Sources* **1995**, *54*, 171.

[86] T. Zheng, J. R. Dahn, *Synth. Met.* **1995**, *73*, 1.

[87] T. Zheng, J. R. Dahn, *Phys. Rev. B* **1996**, *53*, 3061.

[88] T. Zheng, J. N. Reimers, J. R. Dahn, *Phys. Rev. B* **1995**, *51*, 734.

[89] B. Di Pietro, M. Patriarca, B. Scrosati, *J. Power Sources* **1982**, *8*, 289.

[90] K. Sawai, Y. Iwakoshi, T. Ohzuku, *Solid State Ionics* **1994**, *69*, 273.

[91] J. O. Besenhard, *Progress in Intercalation Research* **1994** (Eds: W.

Müller-Warmuth, R. Schöllhorn), Kluwer, Dordrecht, The Netherlands, 457.

[92] J. O. Besenhard, *Soft Chemistry Routes to New Materials**1994*** (Eds: J. Rouxel, M. Tournoux, R. Brec), Materials Science 152, Trans Tech, Aedermannsdorf, Switzerland, 13.

[93] J. R. Dahn, A. K. Sleigh, H. Shi, B. M. Way, W. J. Weydanz, J. N. Reimers, Q. Zhong, U. von Sacken, *Lithium Batteries: New Materials, Developments and Perspectives***1994** (Ed: G. Pistoia), Elsevier, Amsterdam, 1.

[94] J. O. Besenhard, M. Winter, Proc. of the 2. Ulmer Elektrochemische Tage, *Ladungsspeicherung in der Doppelschicht* **1995** (Ed: W. Schmickler), Universitätsverlag Ulm, Germany, 47.

[95] O. Yamamoto, Y. Takeda, N. Imanishi, R. Kanno, *New Sealed Rechargeable Batteries and Supercapacitors***1993** (Eds: B. M. Barnett, E. Dowgiallo, G. Halpert, Y. Matsuda, Z. Takehara), Electrochemical Society, Pennington, NJ, PV93-23,302.

[96] H. Fujimoto, A. Mabuchi, K. Tokumitsu, T. Kasuh, *J. Power Sources* **1995**, *54*, 440.

[97] K. Tokumitsu, A. Mabuchi, H. Fujimoto, T. Kasuh, *J. Power Sources* **1995**, *54*, 444.

[98] S. Yata, H. Kinoshita, M. Komori, N. Ando, T. Kashiwamura, T. Harada, K. Tanaka, T. Yamabe, *Synth. Met.* **1994**, *62*, 153.

[99] S. Yata, K. Sakurai, T. Osaki, Y. Inoue, K. Yamaguchi, *Synth. Met.* **1990**,

33, 177.

[100] S. Yata, Y. Hato, H. Kinoshita, N. Ando, A. Anekawa, T. Hashimoto, M. Yamaguchi, K. Tanaka, T. Yamabe, *Synth. Met.* **1995**, *73*, 273.

[101] Y. Mori, T. Iriyama, T. Hashimoto, S. Yamazaki, F. Kawakami, H. Shiroki, T. Yamabe, *J. Power Sources* **1995**, *56*, 205.

[102] T. Zheng, Q. Zhong, J. R. Dahn, J. Electrochem. Soc. 1995, 142, L211.

[103] M. Alamgir, Q. Zuo, K. M. Abraham, *J. Electrochem. Soc.* **1994**, *141*, L143.

[104] T. Iijima, K. Suzuki, Y. Matsuda, *Synth. Met.* **1995**, *73*, 9.

Outline of Chapter Three

Silicon-Coated Carbon Nanofiber Mat for Anode of Lithium Ion Battery

CHAPTER THREE

Silicon-Coated Carbon Nanofiber Mat for Anode of Lithium Ion Battery

Owing to the current performance deficiencies of micron-sized carbon anode materials such as graphites and hard carbons, researchers have been struggling a long time to develop new materials and new structures to meet the ever-growing market demands. Just as indicated by Richard Feynman in 1959 that "there is plenty of room at the bottom" [1], the emergency of nanoscience and nanotechnology which leads to revolution in basic material science and engineering provided us new opportunities to improve carbonaceous anode performance. The discovery of nanoscaled carbon materials covers carbon nanotubes (CNTs), carbon nanofibers (CNFs), and graphene (Gr) which had profound impact on the development of clean energy storage and conversion systems. Compared to bulk carbon materials, low dimensional carbons exhibit novel properties which are often superior to their bulk counterparts associated with decreased size, unique shape, and defects. Therefore, Li storage mechanism and anodic behavior could be very different from bulk graphite.

Nanocarbon materials enable electrode reactions to occur that cannot take place for materials composed of micrometer-sized particles. The diffusion time constant for Li ions is given by $t=L^2/D$, where L is the diffusion length and D the

diffusion constant [2]. The reduced dimensions increase significantly the rate of lithium insertion/removal and also the electron transport because of the short distances for Li ion transport within the particles [3]. High surface area permits high contact area with electrolyte and hence high Li ions flux across the interface. The strain associated with intercalation is expected to be better accommodated [4] in nanosized carbons. Due to the advantages as mentioned above, nanocarbon materials have been extensively investigated as an anode of LIB.

However, it was found that nanocarbon materials can only provide certain degree of capacity improvement which is still far lower than that people expected. Thus, incorporation of another cheap and high capacity material such as silicon whose specific capacity can reach 3572 mA h g^{-1} at room temperature provides a new way to overcome the above issue [5]. Nevertheless, severe structural pulverization induced by the large volume expansion during charge/discharge makes this material impractical [5]. Therefore, anode capacity improvement by Si while maintaining the structural stability is another big challenge. Thus, the Si-coated CNF mat was synthesized by combining electrospinning and electrochemical deposition in this work. The original idea is to improve the Si structure stability by taking advantage of the entangled three dimensional CNF network which consists of good conductivity and porosity. The structure-related characterization and anode performance of CNF/Si mat will be given in detail. Before that, the relatively popular one dimensional carbon materials such as

CNFs and CNTs will be discussed and compared based on their general properties and the potential to be applied as an anode in LIB. Then the detailed fabrication process of CNF mat through electrospinning method and the anodic performance of as-fabricated CNF mats will be provided in this chaper.

3.1 One Dimensional Carbon Materials as an Anode Material for LIB

One dimensional carbon materials, carbon nanofibers (CNFs) and carbon nanotubes (CNTs) are of great practical and scientific importance. Owing to their similar cylinder shapes, the definitions of CNTs and CNFs are often misleading. Due to the material and structural similarity, common features do exist in their basic properties and Li storage mechanisms. Nevertheless, they are similar in form but distinct in (1) general physical properties, (2) Li storage mechanisms and (3) means of production which will eventually affect the practical application in anode. Therefore, before the detailed discussion of electrospinning fabricated CNF mat, the main anode material applied in this chapter, the general comparison between CNFs and CNTs based on these three different factors is provided here for comprehensive understanding of one dimensional anode materials.

3.1.1 General Physical Property of CNFs and CNTs

If one takes a close look at the basic structure of CNTs and CNFs, the

geometry differences can be easily observed between them. CNFs can be visualized as regularly stacked truncated conical or planar layers along the filament length without hollow core [5 – 8] whereas, CNTs are formed by rolling up graphene sheets to form concentric tubes containing an entire hollow core. In fact, some of the carbon nanotubes being investigated actually qualify as carbon nanofibers because the lack of long-range order as in graphitic materials and/or they have imperfectly rolled graphene sheets. Generally, diameters of CNFs and CNTs can be used as a criterion to distinguish these two kinds of materials, as shown in **Figure 3.1**[9].The diameter of CNTs is around few tens of nanometers whereas the diameter of CNFs is usually larger than hundred nanometers. Both nanomaterials are available in various lengths and could be up to several hundred micrometers depending on the feedstock and the production method.

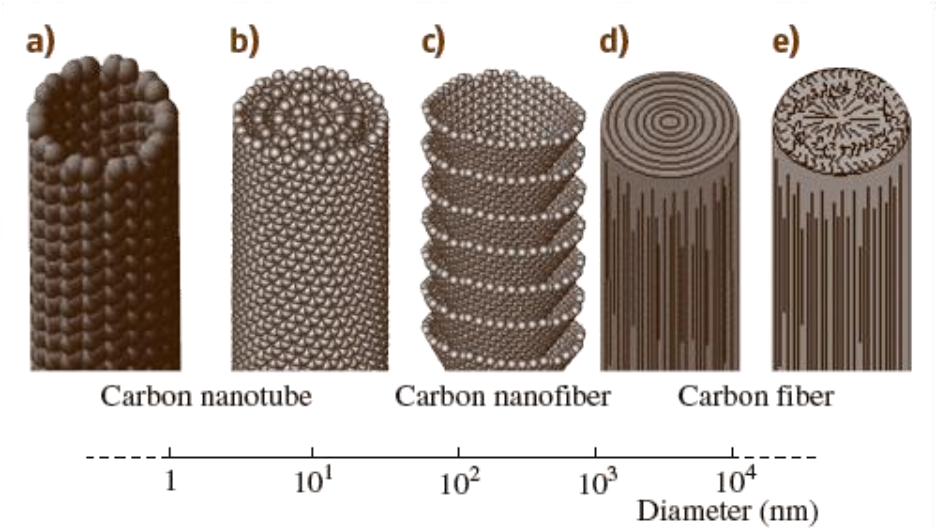

Figure 3.1 Schematic comparison of the diameter dimensions on a log

scale for various types of fibrous carbons. Cited form Ref. [9].

In the case of CNFs, the most important feature is that it exposes large portion of graphene edge planes on its surfaces. In the case of CNTs, since it was formed by rolling up graphene sheets, the basal plane of graphene is exposed, as shown in **Figure 3.2** [10]. This general difference in structure will eventually affect the Li storage mechanism which will be discussed later. Compared to the rather simple configuration of CNFs, CNTs display several different structures based on the number of graphene layers and the rolling direction.

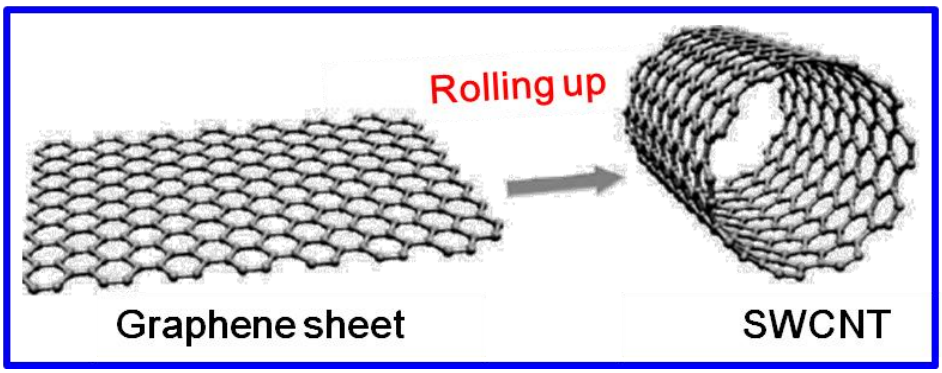

Figure 3.2 Wrapping of graphene sheet to form SWNT. Cited and modified form Ref. [10].

According to the number of graphene layers, CNTs can be further distinguished into SWNTs and MWNTs. SWNT is a single graphene sheet rolled into a form of a tube, whereas MWNTs are composed of several concentric tubes

of graphenes. The diameter of CNTs varies from a few nanometers in the case of SWNTs to several tens of nanometers in the case of MWNTs. The representative TEM figures of SWNT and MWNT are shown in **Figure 3.3** [11].

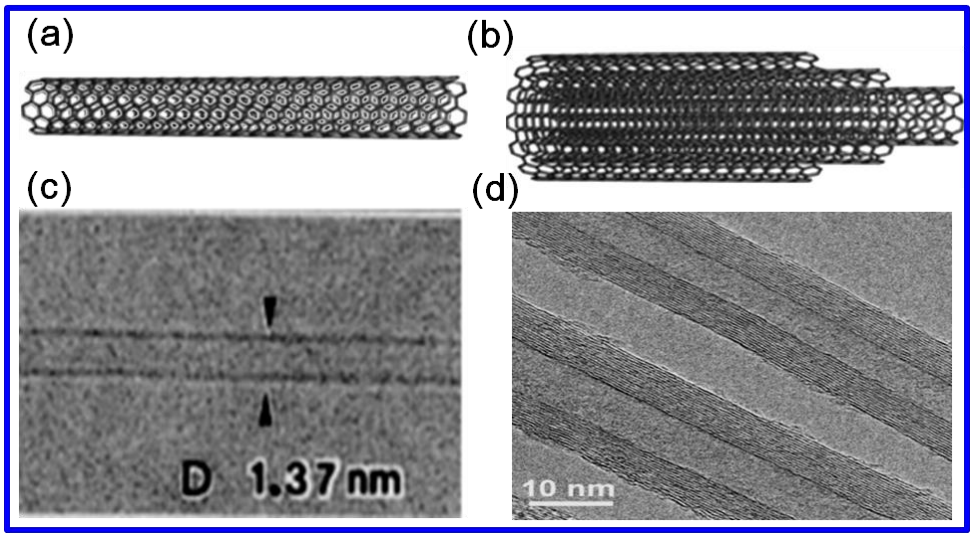

Figure 3.3 Schematic indications of (a) SWCNT, (b) MWCNT, and the corresponding TEM images in (c) and (d). Cited and replotted from Ref. [11].

According to the rolling directions, SWNTs can be completely described by a single vector $\vec{C}$ (called chiral vector), as shown in **Figure 3.4**. Two atoms in a planar graphene sheet are chosen and one set to be origin. The chiral vector $\vec{C}$ is pointed from the first atom toward the second one and is defined by the relation $\vec{C} = n\vec{a_1} + m\vec{a_2}$, where *n* and *m* are integers, $\vec{a_1}$ and $\vec{a_2}$ are the unit cell vectors of the two-dimensional lattice formed by the graphene sheets. The

direction of the nanotube axis is perpendicular to this chiral vector. The angle between the chiral vector and zigzag nanotube axis is the chiral angle θ (**Figure 3.4**). With the integers of *n* and *m* already introduced before, this angle can be defined by $\theta = \tan^{-1}\left((m\sqrt{3})/(m+2n)\right)$. SWNTs can be described by the pair of integers (*n*,*m*) which is related to the chiral vector. Three types of SWNTs are revealed with these values: when $n = m$, the nanotube is called "armchair" type ($\theta = 0^\circ$); when $m = 0$, then it is of the "zigzag" type ($\theta = 30^\circ$). Otherwise, when $n \neq m$, it is a "chiral" tube and θ takes a value between 0◦ and 30◦. The value of (*n*,*m*) determines the chirality of the nanotube and affects the electronic property. SWNTs with $|n-m| = 3q$ are metallic and those with $|n-m| = 3q \pm 1$ are semiconducting (q is an integer) [12].

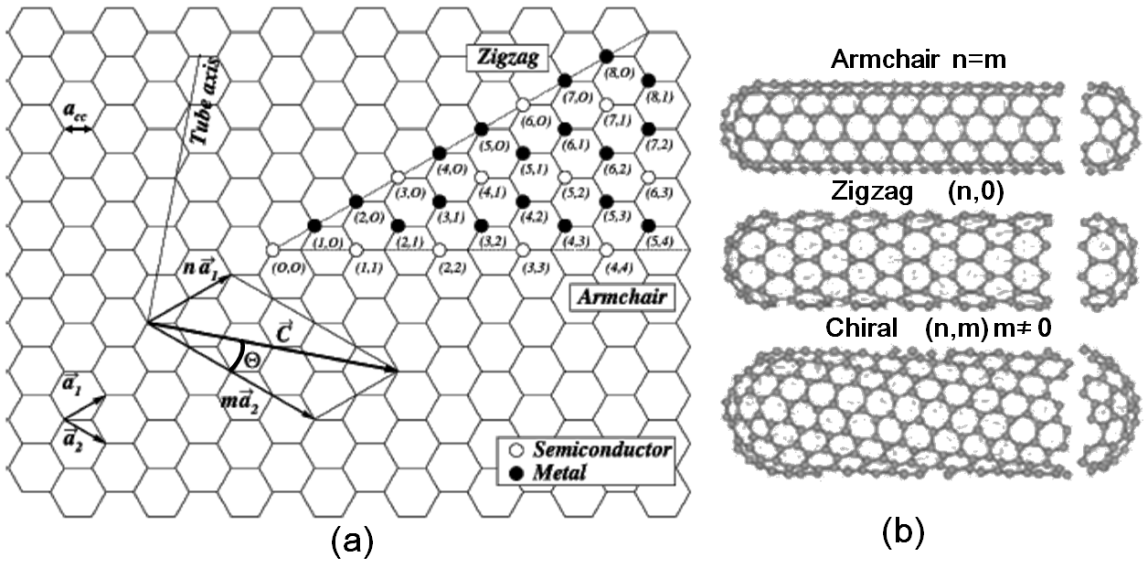

Figure 3.4. Chiral vector $\vec{C}$ and chiral angle Θ definition for a (2, 4) nanotube on graphene sheet. $\vec{a_1}$ and $\vec{a_2}$.are the unit cell vectors

of the two-dimensional hexagonal graphene sheet. The circumference of nanotube is given by the length of chiral vector. The chiral angle θ is defined as the angle between chiral vector $\vec{C}$ and the zigzag axis. Cited and modified from Ref. [12].

Compared to SWNTs which display complex structure-determined electronic properties, MWNTs are multi-surface graphene with various chiral angles and would lose special electronic properties, and thus they reveal an average effect of all chiral tubes and thus usually exhibit a metallic property since their diameters are large. [11]. In comparison with CNTs, CNFs show relatively low conductivity. As a result, in the aspect of material conductivity, CNTs could be better choice for LIB anode.

3.1.2 CNFs and CNTs Using as an Anode Material for LIB

The limited capacity of graphite as introduced in chapter two has hindered the further development of battery technology. The interesting properties of one dimensional carbon materials therefore have been widely studied to substitute graphite as an anode material of LIB. Generally, CNTs and CNFs show similar advanced properties with graphite. On the one hand, they preserve even exceed the common graphite in the sense of high chemical stability and low resistance; On the other hand, they show other favorable characteristics which could further

benefit the performance of anode. For example, CNTs and CNFs exhibit high specific area which increases the contact area of electrode and electrolyte leading to higher charge/discharge rates. The high mechanical strength and flexibility is again superb for a long cycle life [13-16] and potential application in flexible electronics, respectively.

The storage mechanisms of Li in CNFs and CNTs are similar to each other and resemble that of bulk carbon materials combing the characteristics of graphite and non-graphitic carbon. Li ions could be stored through: (1) intercalation (LiC_6 stoichiometry); (2) adsorption and accumulation on the outer surface, (3) void space between bundles, (4) defect sites, cavities and nanopores. These kind of storage mechanisms have been well illustrated in chapter two, see **Figure 2.10** [17-18].

However, one main difference does exist between CNFs and CNTs. In the case of CNTs, lithium insertion through the walls (basal plane of graphene sheet) or the capped ends is energetically not favorable as suggested by Kar et al. who investigated lithium insertion into CNTs by *ab* initio and DFT methods [19]. On the other hand, lithium ions can be inserted through CNF walls since it is mainly composed of edge plane of graphene sheets [5-9]. More comprehensive information related to Li insertion through these two kinds of graphene planes will be provided in chapter 4. Thus, in the aspect of feasibility of Li penetration

which is closely related to the storage capacity and charge/discharge rate, CNFs using as anode material could be more advanced compared to CNTs.

In addition to the differences in basic material property and Li storage mechanism as mention above, one more important factor that needs to be considered is the means of fabrication for one dimensional carbon materials. As a matter of fact, styles of the produced carbon materials, feasibility for further processing into LIB anode, and also cost all have huge influences for the real application of CNFs and CNTs. Thus, the following section will mainly focus on discussion of two popular fabrication methods of CNFs and CNTs.

3.1.3 Fabrication Methods of CNFs and CNTs

3.1.3-1 Chemical Vapor Deposition for CNFs and CNTs

Owing to material and structure similarity, both CNFs and CNTs can be synthesized through chemical vapor deposition (CVD). CVD is a well known production method for carbon based materials. One dimensional CNF/CNT and two dimensional graphene can be fabricated using this method. Three basic elements for CVD growth are catalyst, carbon precursor, and sufficient thermal energy for gas decomposition and reaction to occur. Briefly, the CVD method involves the decomposition of a gaseous or volatile compound of carbon, catalyzed by metallic nanoparticles with external energy supply, which will also

serve as nucleation sites for the initiation of low dimensional carbon growth. The most frequently used catalysts are transition metals, primarily Fe, Co, or Ni. The energy source is heat from a furnace of CVD [11]. By varying the conditions, powder-like samples or film-like samples consist of vertically aligned CNTs or network of CNFs/CNTs which are supposed to benefit the fabrication process of LIB electrodes, can be easily obtained, as shown in **Figure 3.5**. The length, diameter, and morphology of CNFs and CNTs also can be controlled during the synthesis process.

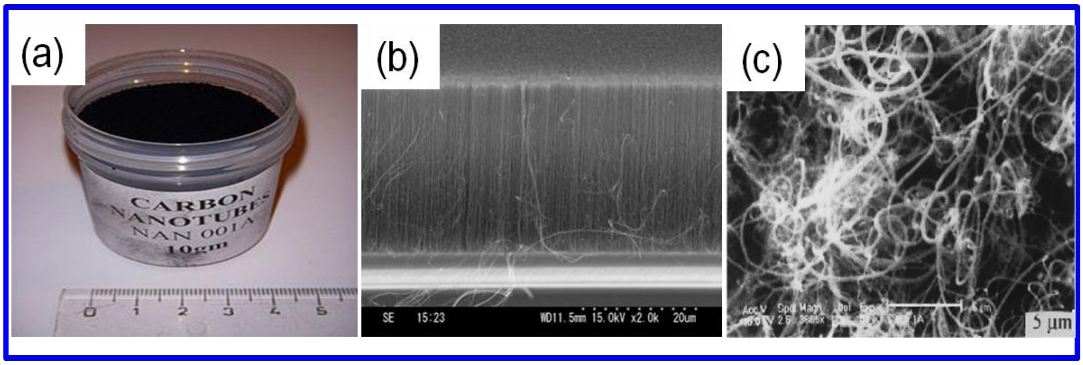

Figure 3.5 CVD process-fabricated (a) CNT power, (b) vertically aligned CNTs, and (c) CNF planar network. Cited from Ref. [11].

One dimensional carbon anode usually consists of a thin layer of CNFs/CNTs which is mounted onto a metal current collector. Compared to vertically aligned CNFs/CNTs electrode, planar network-like (film or mat) morphology is preferred not only because it is suitable to the conventional coin cell battery fabrication but also the short circuit problem triggered by material

piercing through the separator can be avoided. In the case of as-grown CNFs or CNTs network, the remaining impurities such as catalyst for growth and also an appropriate substrate for growth need to be considered before anode preparation. Combining all of the factors, power-like CNFs/CNTs samples are widely used nowadays. In order to form a network style CNFs or CNTs film from the as-synthesized powder, material functionalization and dispersion in liquid are usually required before the electrode fabrication.

Since CNFs expose graphene edge planes on its surfaces, the surface state can be easily modified through chemical functionalization or thermal treatments whenever necessary. Functionalizing and dispersing the CNFs are possible to be performed using traditional, scalable, and fast processing methods. On the other hand, the CNT functionalization was usually performed before dispersion by first creating defect sites along the side walls of tubes, which can then be utilized for attaching functional groups. This kind of method usually reduces the conductivity and mechanical strength of CNTs and requires several processing steps. Thus CNTs are more difficult and more costly to scale-up with respect to CNFs.

Furthermore, in the case of CNTs, due to their smaller sizes than CNFs, van der Waals forces are stronger which induce the formation of ropes or reassemble after being dispersed. Therefore, chemical dispersants or functionalization

techniques are usually required to aid and maintain dispersion. Unlike CNTs, CNFs with a stacked-cup style are less affected by van der Waals forces and tend to stay dispersed for a longer period of time. This difference enables CNFs to be dispersed through purely mechanical processing techniques without the need for additional, and costly, processing steps, making CNFs easier and cheaper to process.

Finally, the prices of CNTs and CNFs are very different depending on the producer but in general, the cost of CNFs is typically an order-of-magnitude lower than that of CNTs. CNFs are available in large volumes (up to 70,000 pounds per year) and range in price from as low as $ 100 per pound to as high as $ 500 per pound. As to CNTs, the price varies widely and is strongly dependent on the quality and purity of the products. One can find commercialized CNT powder with the price as low as $100 per pound to as high as $ 750 per gram or more. Therefore, the costs for just the raw material plus the one for the extra cost of additional processing steps (such as purification and functionalization) are much higher than that of CNFs. The series of post-treatment procedures also significantly increase the complexity of the application of CNTs.

To conclude all of the factors as mentioned above, it is clear that CNFs could be simpler and more cost effective material to be adopted in LIB compared to CNTs. However, CVD method for the production of CNFs still remains

unsolved in many aspects. The complex experimental setup such as certain vacuum level, toxic gases protection, and even plasma or microwave involvement makes it less cost effective. Also, metals that are introduced as catalysts during the synthesis usually exist in the sample which interferes with the desired properties of CNFs and cause a serious impediment in detailed characterization and applications [10-12,20].

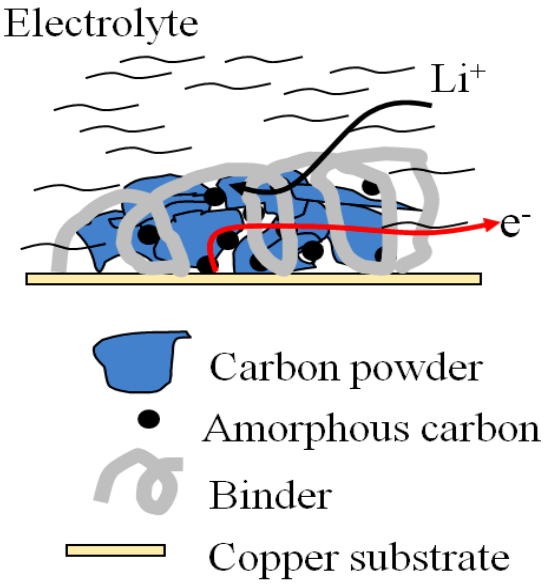

Figure 3.6 Typical anode assembling based on CVD process fabricated carbon powder. Cited and modified from Ref. [20]

Furthermore, it is worth noting that a metal current collector and binders are required to complete the final assembly of CVD-grown CNFs powder electrode, as shown in **Figure 3.6** [20]. The use of metal substrate not only increases the mass of electrode which decreases the specific capacity but also causes a

corrosion-related issue in a long run. As for the use of binder, the conductivity and effective mass of the electrode also will be affected. Therefore, a mature CNF network fabrication method which is catalyst-free, easy, cost-effective combining a mat/film style sample as a final product to avoid the multiple steps of post treatments is highly demanded in the industrial field of anode fabrication.

3.1.3-2 Electrospinning Method for CNF Mat

Fortunately, free-standing CNFs mat can be fabricated by electrospinning as an alternative method of CVD. Electrospinning uses an electrical charge to draw very fine (typically on the micro or nano scale) fibres from liquid. This traditional method usually combines electrospinning of organic polymers and thermal treatment in an inert atmosphere. The electrospinning technique has been considered to be one of the advanced fiber formation techniques from polymer solution by using electrostatic forces [21-24]. Electrospun-based nanofibers exhibited noticeable properties, such as nanosized diameter, high surface area, and thin web morphology, which make them applicable to the fabrication of high-performance nanocomposites and energy storage devices [25-31]. The simple experimental setup and rather easy process compared to CVD are particularly suitable for the production of CNFs in large scale. Since this method was adopted in the research part in this work, the fundamental mechanism and detailed experimental procedures will be further explained as following.

In the electrospinning process, a polymer solution held by its surface tension at the end of a capillary tube is subjected to an electric field. Charge is induced on the liquid surface by an electric field. Mutual charge repulsion causes a force directly opposite to the surface tension. As the intensity of the electric field is increased, the hemispherical surface of the solution at the tip of the capillary tube elongates to form a conical shape known as the Taylor cone [32]. When the electric field reaches a critical value in which the repulsive electric force overcomes the surface tension force, a charged jet of the solution is ejected from the tip of the Taylor cone. Since this jet is charged, its track can be controlled by an electric field. As the jet travels in air, the solvent evaporates, leaving behind a charged polymer fiber which lays itself randomly on a collecting metal screen. Thus, continuous fibers are laid to form a fabric film [32].

The above description of the process suggests that the following parameters affect the process: solution properties including viscosity, conductivity, and surface tension; controlled variables including hydrostatic pressure in the capillary, electric potential at the tip, and the distance between the tip and the collection screen; and ambient parameters including temperature, humidity, and air velocity in the electrospinning chamber. By appropriately varying one or more of the above parameters, fibers with desired properties can be successfully produced [32].

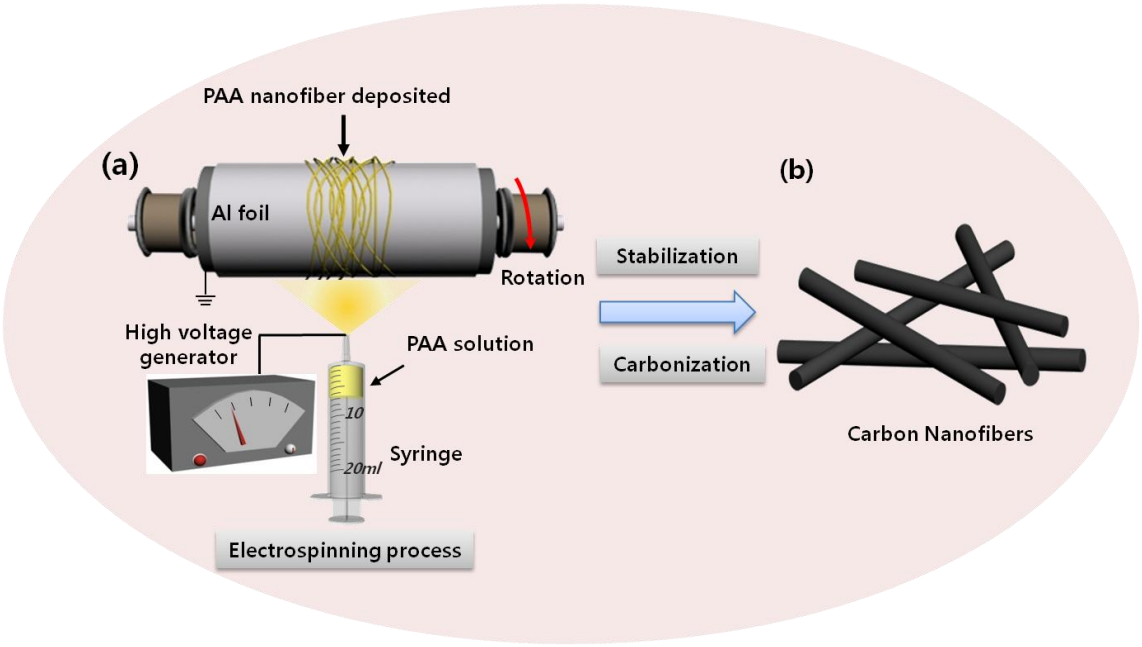

Figure 3.7. Schematic of CNF mat fabrication processes: (a) schematic of electrospinning apparatus and (b) the fabricated nanofiber network.

To be more specific, here, fabrication process of polyimide (PI)-based CNFs which were also characterized as an anode in LIB in the following section are taken as an example. The apparatus used in the electrospinning process is shown in **Figure 3.7**. It consists of a glass syringe with a maximum volume of 20 ml. The glass syringe was filled with a Poly(amic acid) (PAA) solution, inside where a metal needle (figure not shown) was embedded at the tip of the solution. A syringe pump (figure not shown) was used to keep the solution at the tip of the tube and also control the flow rate (injection rate) of solution. The solution was

charged by connecting the metal electrode to a high voltage power supply. A cylindrical collector wrapped with aluminum foil was used as collecting devices for the charged fibers.

The Poly(amic acid) (PAA) was synthesized by pyromellitic dianhydride (PMDA, Sigma Aldrich) and oxydianiline (ODA). PMDA of 4.4 g was added into ODA (4.0 g) pre-dissolved DMF solution (21 g). The mixture was stirred for 30 min with a magnetic bar. 413 μL triethyl amine (TEA) was then added to control the molecular weight. The as-prepared solution was then electrospun into PAA nanofibers. The separation distance between the needle and collector, DC bias voltage, and solution flow rate were 15 cm, 20 kV, and 0.2 mL h-1, respectively. The PAA nanofiber mat with aluminum foil was then put into stabilization oven and converted into polyimide (PI) mat after seven different oxidation steps at a rate of 1°C min^{-1}.[52] The PI mat was then peeled off from the aluminum foil and transferred into high temperature furnace. CNF mat was formed by annealing the PI mat according to three steps annealing procedures (firstly from room temperature to 600 °C in 1 h, then 600 °C to 1000 °C in 1.3 h, and finally maintaining in 1000 °C for 1 h) under argon gas environment by following the previous publication [33].

3.2 Electrospinning Fabricated CNFs Mat as an Anode Material for LIB

3.2.1 SEM and Raman Characterization of CNFs Synthesized Through Electrospinning

The as-fabricated CNFs mat was free-standing film with a large area up to 15 x 15 cm^2. CNF mat were carefully weighted by using the A&D BM-22 microbalance located inside the dry room after cut into a 1.5 cm diameter round shape. The average mass of the film was around 1mg with a thickness of 25 ± 3 μm. Typical SEM images of CNFs mat were shown in **Figure 3.8**. The average diameter of the fiber was around 180 nm and the surface of CNFs was smooth and clean. The micro-Raman spectra was shown in **Figure 3.9**. It clearly showed a G-band near 1592 cm^{-1}, which is related to the optical E_{2g} phonon at the Brillouin zone center indicating sp^2 hybridization of carbon network and a D-band near 1352 cm^{-1}, which corresponds to transverse optical phonon near the K point and indicates sp^3 hybridization of carbon network [34]. The intensity ratio of D band to G band (I_D/I_G) was around 0.83. This fairly high value of I_D/I_G indicates the existence of large amount of disorder carbon phase and rather poor conductivity of CNFs. This could lead to a poor electrochemical cycle performance. Further extensive high temperature (> 1000 °C) and high vacuum treatment could improve the crystallinity of the as-synthesized CNFs mat, but the degree of the flexibility and the extra cost need to be considered.

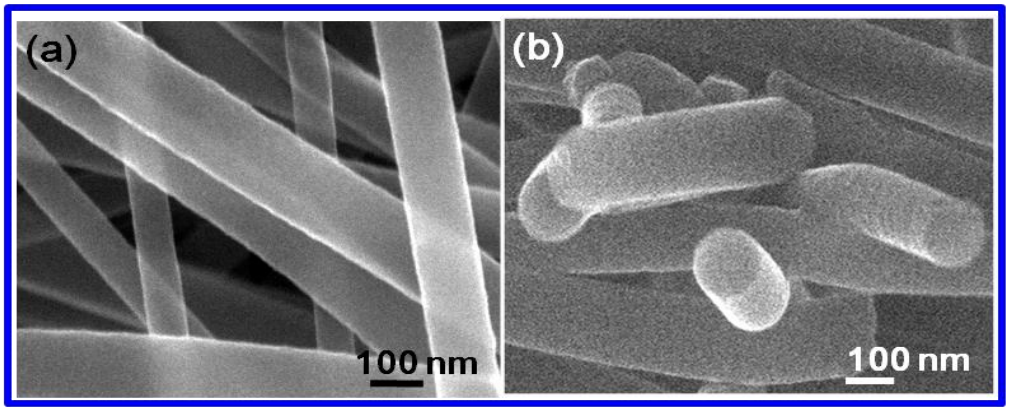

Figure 3.8. SEM images of as-synthesized CNFs with (a) top view and (b) cross-sectional images.

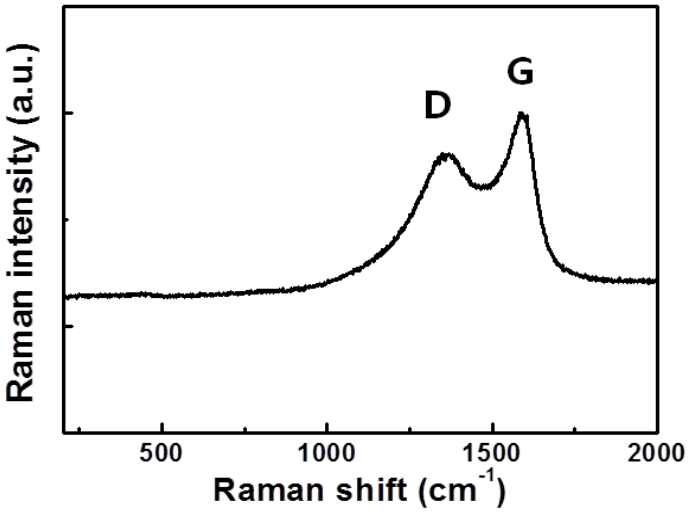

Figure 3.9. Micro-Raman spectra of CNFs mat fabricated by electrospinning method.

This kind of free-standing CNF mat fabricated through a simple electrospinning method is of great interest to be studied as an anode material in LIB because not only the sample exhibits a film-like nature right after the

fabrication, which avoids the use of binder and metal substrate, but also the well-interconnected three-dimensional network structure provides a good porosity and reasonable conductivity compared to common graphite. Therefore, the as-fabricated CNF mat was applied and tested as an anode in the following section.

3.2.2 Anode Performance of CNFs Synthesized Through Electrospinning

The electrospinning fabricated CNF mat were directly used as an anode for LIB test in the section. Electrochemical measurements were carried out with a CR 2032 coin cell using VMP3 instrument (BioLogic Science Instruments). The cell was assembled in a dry room using CR 2032 cell case with bare CNF mat as a working electrode, lithium metal foil as a counter/reference electrode, and 1 M of $LiPF_6$ in a 1:1 (v/v) mixture of ethylene carbonate (EC) and diethyl carbonate (DEC) as electrolyte. No extra metal current collector, binder or conducting agent were used. A glassy carbon microfiber was used as a separator. The cells were charged and discharged galvanostatically between 2.0 and 0.01 V vs. Li/Li^+. Here, we defined 1 C to be 372 mA h g^{-1}. The general charge/discharge profile is shown in **Figure 3.10a**.

The charge/discharge (CD) profiles of CNF mat show a gradual change in a broad voltage window during charge/discharge, revealing a V-shape feature. This is in good contrast with a U-shaped graphite CD curve due to the existence of

disordered carbon phase in our CNF mat [35-36]. In the 1st charge of CNF, a plateau near 0.7 V vs. Li/Li+ can be attributed to the formation of solid-electrolyte interface (SEI) via electrolyte decomposition [35]. In the discharge process, the slope of the curve started approximately at 0.3 V vs. Li/Li^+ and has delivered a specific capacity around 100 mA h g^{-1} below 0.1 V vs. Li/Li^+. The capacity from the potential region above 0.1 V may be ascribed to the faradic capacitance on the surface of CNFs and the capacity from the region lower than 0.1 V can be related to the lithium intercalation into CNFs [36-38]. This is in good agreements with combining effect of graphite and non-graphitic carbon as analyzed in chapter two. The CNF mat delivered a charge and discharge capacity of 776 and 458 mA h g^{-1} in the 1st cycle and nearly saturated to 280 and 281 mA h g^{-1} after 50 cycles. The related capacity of each cycle, the rate performance

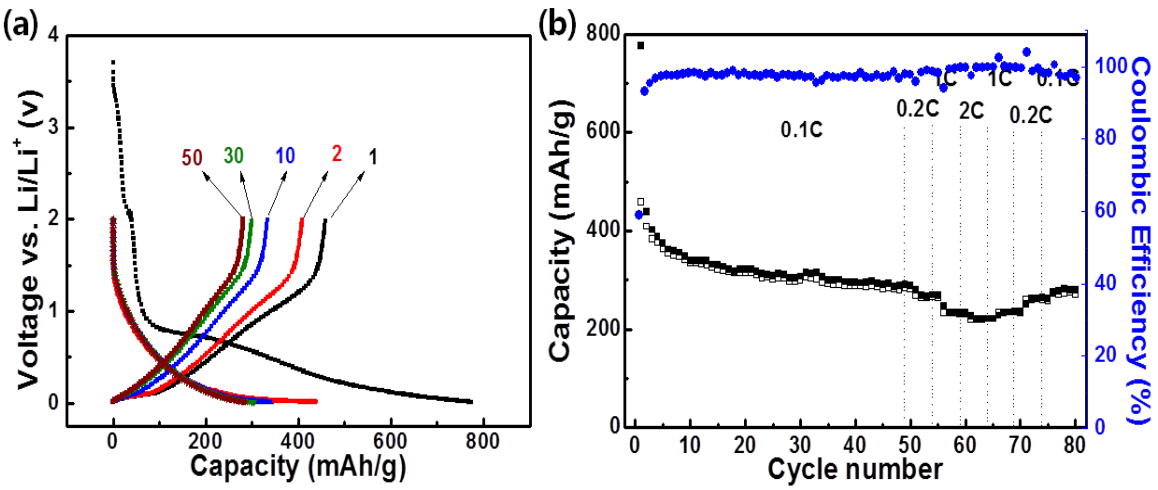

Figure 3.10. (a) Voltage profiles electrospinning fabricated CNF mat between 0.01 and 2 V at a charging rate of 0.1 C. The cycle numbers

are indicated in the figure. (b) Rate performance and columbic efficiency of the above sample.

with higher current and columbic efficiency were summarized in **Figure 3.10b**. It is clear to see the columbic efficiency which is defined as discharge capacity divide by the charge capacity in the first cycle was only 60% and increased to almost 100% in the following cycle. The small columbic efficiency is induced by the large irreversible capacity which is related to the SEI formation as mentioned in chapter two.

In summary, although both lithium intercalation and other storage mechanisms are possible in CNF mat, the slightly higher lithium storage capacity compared to graphite in the beginning of the cycling is far lower than we expected. Furthermore, similar problems of surface-electrolyte interface (SEI) formation and rather large Li insertion potential window as mentioned in non-graphitic carbon in chapter two still exist. As a result, CNFs do not seem to offer a major route to improve the anode performance. Thus, searching for nanomaterial-based alternatives for graphite that combine inherent protection against lithium deposition, low cost, low toxicity, fast lithium insertion/removal speed and also higher capacity still remains challenging.

3.3 Silicon-Coated Carbon Nanofiber Mat for Anode of Lithium Ion

Battery

3.3.1 Introduction

In order to improve the capacity of conventional carbon based materials, researchers have been focusing on the discovery of high capacity materials. Recently, silicon, a high lithium storage capacity material (specific capacity of 3572 mA h g^{-1} at room temperature, corresponding to $Li_{15}Si_4$) has been proposed [39]. Yet, large volume expansion up to 400 % during charge/discharge causes a severe structural pulverization, making this material impractical. For instance, a simple deposition of Si thin film on metal substrate leaves crack formation during cycling and therefore a contact loss between active material and current collector occurs, leading to a poor cyclability, as shown in **Figure 3.11** [40]. Si nanowires/nanotubes (NWs/NTs) fabricated by various methods on metal substrate could be an ideal approach to accommodate the volume change due to existence of sufficient empty space between adjacent NWs/NTs [41-42]. However, poor root adhesion with substrate and its brittle nature usually create troubles in traditional coin cell fabrication process. On the other hand, the major issue for Si nanoparticles, compared to Si NWs/NTs, is the formation and preservation of electrical contact between each nanoparticle and substrate [43]. This means that additional binder and conductive additives are usually needed, which is similar to carbon based powder materials as mentioned in section 3.1.3-1 and will in turn increase the dead mass and thus reduce the capacity of the

electrode.

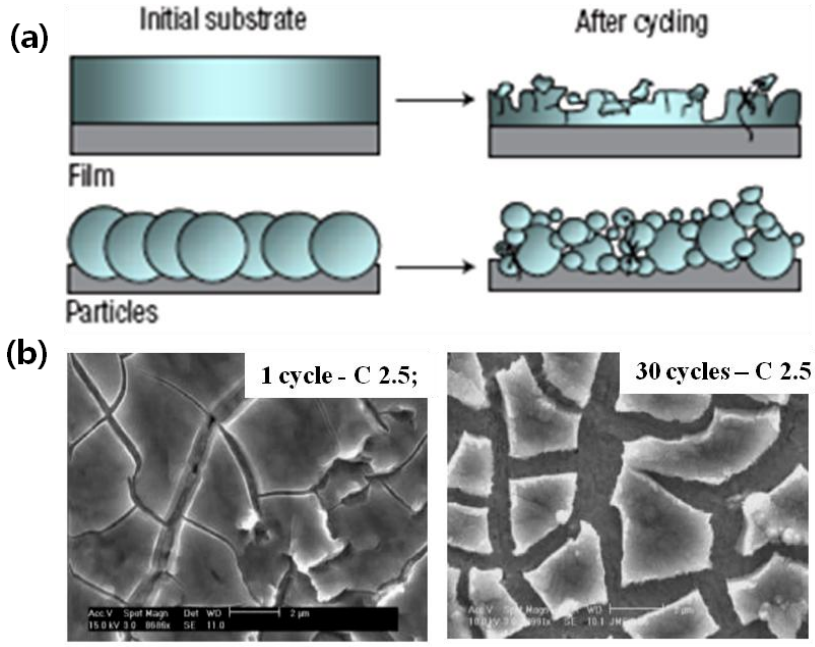

Figure 3.11. (a) Structure deformation indication of Si based film/particles before and after charge/discharge cycling. (b) SEI images of CVD deposited Si thin film on Cu stustrate after 1st and 30th cycles of charge/discharge. Cited and modified from Ref. [20].

Owing to these difficulties, several Si/nanocarbon composites have been proposed. Silicon has been successfully deposited onto carbon fibers or CNFs through chemical vapor deposition or sputtering [44-53]. Although Li storage capacity was improved due to the contribution of deposited Si layers, inhomogeneous deposition of Si atoms on fibers along the depth of the film diminishes the effect of Si layers. Si nanoparticles have been deposited on CNFs

by dispersing them in organic solution and then co-spinning onto metal substrate followed by heat treatment [50-53]. This causes again undefined nature of adhesion between Si nanoparticles and CNFs, which is closely related to the efficiency of charge transport across the interface. Electrochemical deposition of silicon onto CNF substrate is rather promising, since the liquid reaction is easy to handle with low cost and also the shape of silicon can be controlled by the deposition conditions. Apart from the fabrication benefits, the CNF mat is a free-standing three dimensional skeleton and is conductive and porous so that the use of binders and conductive additives can be avoided.

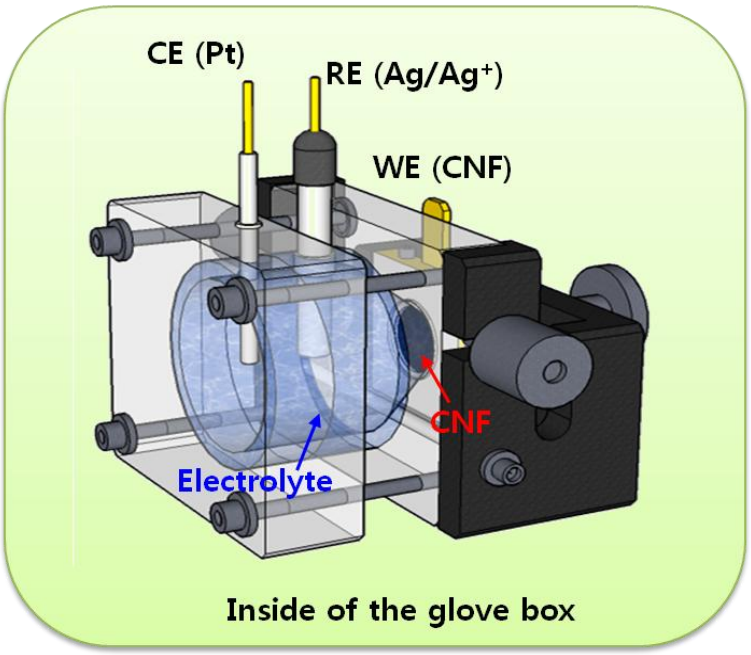

Figure 3.12.Schematic of the apparatus for electrodeposition of Si. The cell consists of three electrodes: woking electrode (as-fabricated CNF mat), counter electrode (Pt wire) and reference electrode

(Ag/Ag^{+}). During the deposition, a Si-containing electrolyte ($SiCl_4$ in PC) was add into the cell and a cyclic voltage scan (20 mV s^{-1}) was applied to the electrodes.

In this study, the free-standing CNF mat was fabricated by using electrospinning of polymer solution followed by stabilization and carbonization, as introduced in section 3.1.3-2. Si was deposited on the surface of CNFs by electrodeposition method through a home-made three-electrode cell. The cell configuration was shown in **Figure 3.12**. By varying the deposition conditions, a spaghetti-like Si layer with high surface area and porosity was formed. Si layer was uniformly coated over nanofibers independent of the depth of the film. More importantly, volume expansion was easily accommodated on the cylindrical fibers and highly porous network of CNF mat. High temperature annealing of 1000 °C was performed to improve material purity and construct stable Si and CNF interface by forming Si-C bond. This free-standing Si-coated CNF mat was directly used as an anode material for LIB without using any additional metal substrate or extra binder materials. The capacity of Si/CNF mat anode was clearly improved by almost twice compared to that of graphite material. The detailed electrochemical analysis was provided in conjunction with structural properties.

3.3.2 Characterizations of CNF-Si Mat

Figure 3.13a shows typical cyclic voltammograms (CVs) at a scan rate of 20 mV s^{-1} for CNF in PC electrolyte with/without adding $SiCl_4$. It is clear to see a reduction peak centered at around -2.0 V only in the case of electrolyte containing $SiCl_4$. This suggests that Si ion is reduced into Si and deposited onto CNF mat during CV test following the electrochemical reaction $SiCl_4 + 4\ e^- \rightarrow Si + 4Cl^+$. Si loading amount on CNF mat was controlled by varying number of CV deposition cycles, as shown in **Figure 3.13b**. Mass (thickness) of Si/CNF mat keeps increasing from ~ 1 mg to ~ 4 mg (from ~ 25 μm to 130 μm), as the number of Si deposition cycles increased to 1000 cycles.

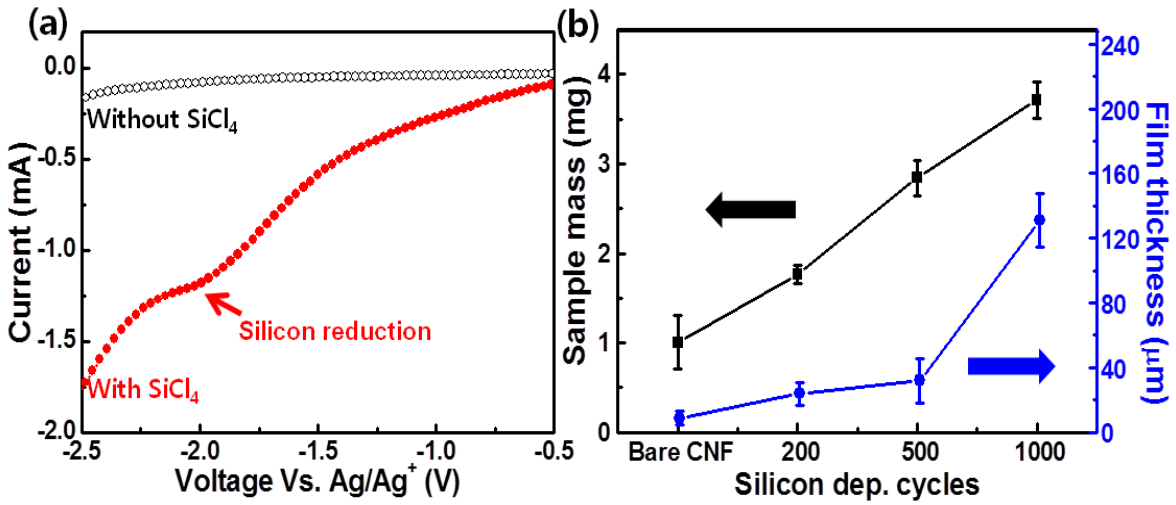

Figure 3.13. (a) Cyclic voltammograms of silicon electrodeposition in PC solution with/without $SiCl_4$ at a scan rate of 20 mV s^{-1}. (b) Mass and thickness of Si/CNF mat with respect to different silicon

deposition cycles. The error bar is added in the figure.

A series of structure characterizations of Si/CNF mat of with 200 cycles CV deposition are shown in **Figure 3.14.** Micro-Raman spectra of bare CNF mat (also shown in **Figure 3.9**) and pristine Si/CNF mat (without annealing, indicated as Si-200-p) in **Figure 3.14a** shows intensity ratio of D band to G band (I_D/I_G) remained unchanged (~ 0.83) between bare CNF and Si-200-p after electrodeposition of Si, indicating that carbon material is remarkably stable compared to traditional metal substrate in severe electrochemical environment [37]. However, in the case of Si/CNF mat after 1000 °C annealing (indicated as Si-200-a), the value of I_D/I_G slightly decreased to ~ 0.79, suggesting an improved graphitization in the CNF network. It is of note that no Si related peak can be found in Si-200-p. This could be ascribed to the highly disordered nature of the deposited Si which is caused by electrostatic clustering with alkyl terminators and also the presence of deposited electrolyte residues on the surface, as shown in **Figure 3.15a** [54]. On the other hand, three additional Si related peaks were shown in the spectrum of Si-200-a. It is known that first order transverse-optical (TO) phonon mode of crystalline Si (c-Si) will display a sharp peak at 520 cm^{-1} which usually becomes broaden and is downshifted when the long-range order in Si is lost [55]. In our case, the peak located at around 500 cm^{-1} was assigned to microcrystalline or nanocrystalline (μc/nc) Si and a broad band at the low energy side originated from the presence of amorphous Si (a-Si). The peak near 300 cm^{-1}

resembles transverse acoustic (TA) phonon mode of c-Si and could be softened in a-Si [55-57]. In addition, c-Si usually exhibits a small peak at 950 cm^{-1} which is related to the chemisorption of atomic/molecular oxygen species [58]. Here, we also found a softened peak at 920 cm^{-1} in Si-200-a. A red shift of 30 cm^{-1} is possibly caused by the existence of a-Si [57]. All of these factors demonstrate that as-deposited Si is completely disordered and evolves into more distinct a-Si and μc/nc-Si with additional oxygen species after high temperature annealing.

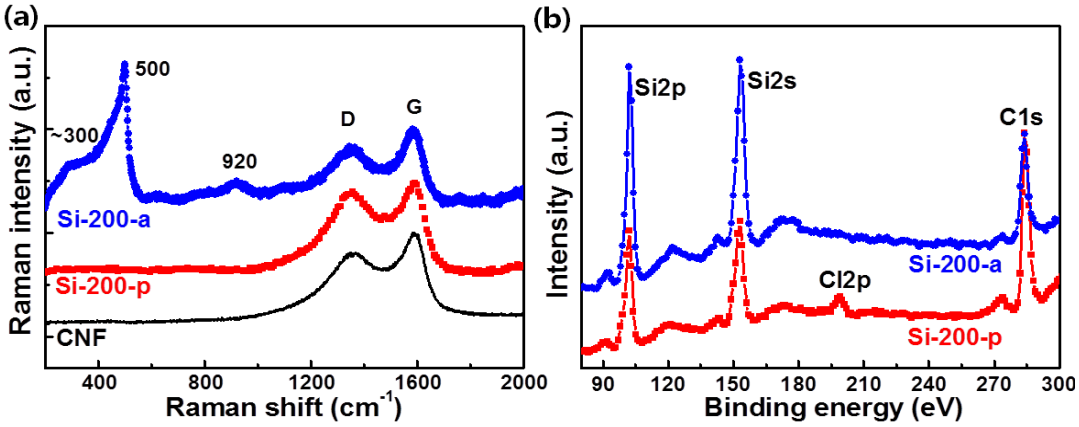

Figure 3.14. (a) Micro-Raman spectra of bare CNF mat and Si/CNF mat with 200 cycles of Si deposition before/after annealing, indicated as Si-200-p and as Si-200-a in the figure. (b) XPS spectra of the electrode surface with active materials consisting of Si-200-p and Si-200-a, respectively.

Figure 3.14b plots the XPS spectra of Si/CNF mat with 200 cycles

deposition before and after1000 °C annealing. It is obvious to see that the intensities of Si 2s and Si 2p peaks increased clearly while the C 1s peak relatively decreased. In addition, Cl 2p peak which appeared in Si-200-p disappeared after annealing. After Si electrodeposition, certain amount of electrolyte could be decomposed and remained on the Si surface. After annealing, the residual film which mainly contained C, O, and Cl was removed, as seen in **Figure 3.15**. This is also in good corroboration with **Figure 3.14a**.

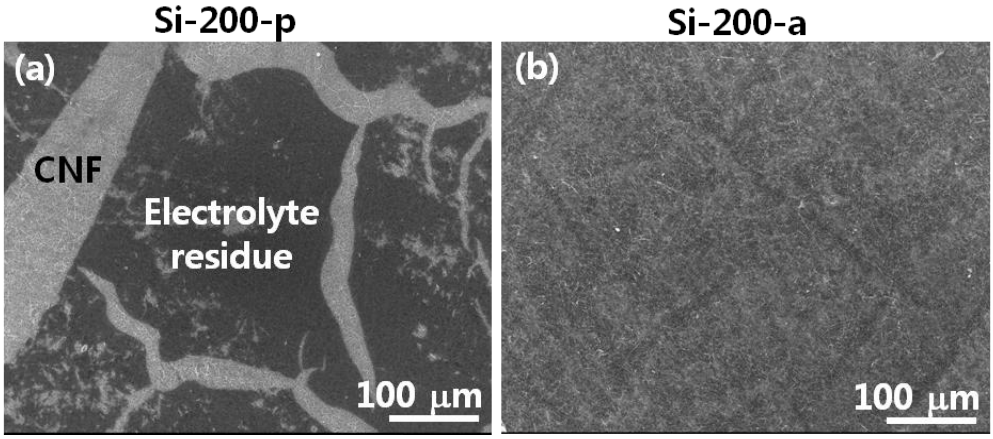

Figure 3.15. SEM images of (a) Si-200-p and (b) Si-200-a samples. Dark color portion indicates electrolyte residues on the surface of CNF mat. After 1000 °C annealing, the uniform mat surface was observed by the removal of electrolyte, as shown in (b).

Figure 3.16a is the SEM image of the bare CNF mat which already explained in **Figuer 3.8.** On the other hand, the Si-200-a sample displayed a

rough spaghetti-like surface, as shown in **Figure 3.16b**. The cross sectional view of Si-CNF core-shell structure was shown in the inset of **Figure 3.16b**. It is of note that the core-shell structure was formed uniformly independent of the depth over hundred micrometers, which is in good contrast with other methods such as sputtering and CVD, in which Si is not uniformly deposited along the depth of the sample. AFM morphology of the same sample was provided in **Figure 3.16c** with an amplified phase image in **Figure 3.16d**, again demonstrating rough Si surface on the surface of CNFs. This unique spaghetti-like Si structure provided large surface area compared to the flat Si thin film which can facilitate the charge transfer at the electrolyte/Si interface. Moreover, the volume expansion can be accommodated to certain degree by the high porosity of Si under the condition of 200 cycles deposition which is certainly better than the thick Si layers.

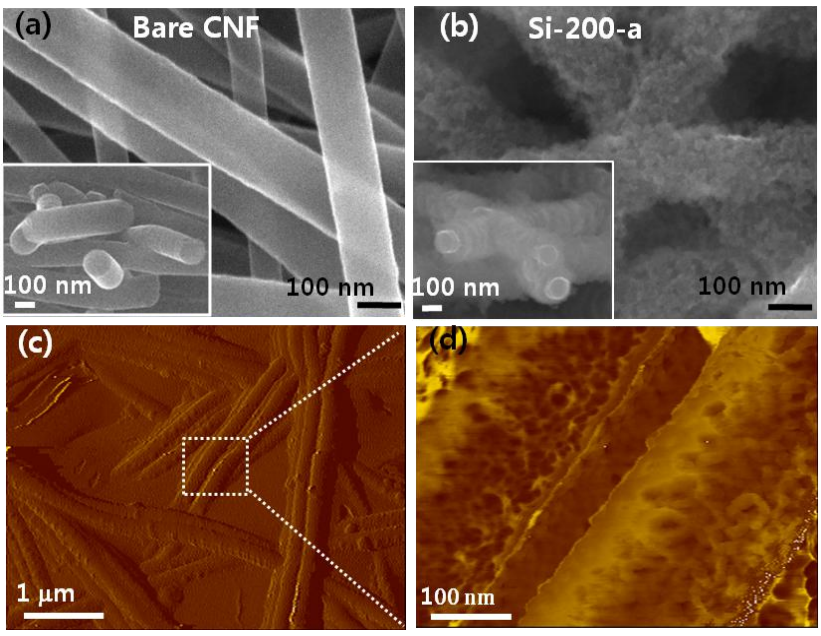

Figure 3.16. (a) SEM images of as-synthesized bare CNFs and (b) Si-200-a. The cross-sectional images are shown in the insets. (c) AFM image of Si-200-a. The high resolution image of dashed square in (c) is shown in (d).

Figure 3.17a is the TEM image of the Si-200-a sample. The layer thickness of deposited Si was ~ 20 nm in this case. The existence of Si on the surface of CNF was again confirmed by EDS line profile along the dashed line in the TEM figure, as shown in **Figure 3.17b**. The spaghetti shape of Si was not visible here probably due to the sample damage during TEM sample preparation process with sonication. Since the thin film of electrodeposited silicon is highly active and therefore can be oxidized immediately upon exposure to air during transfer from the glove box to TEM, or X-ray diffraction (XRD) measurements, the crystalline nature of the electrodeposited Si film is unlikely to be directly observed [59].

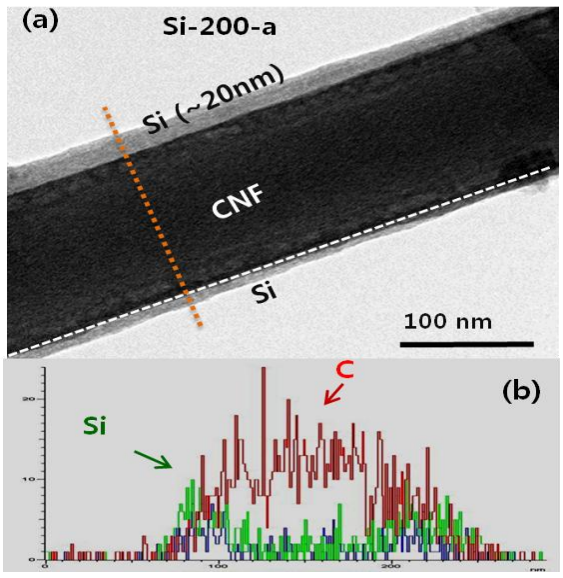

Figure 3.17. (a) TEM image of Si-200-a. The EDS line profile along the dashed line is shown in (b).

To obtain information of interface between CNF and Si, C 1s and Si 2p peaks in XPS were deconvoluted, as shown in **Figure 3.18.** C 1s peaks before and after annealing were clearly distinct with each other. Clear Si-C peak near 283 eV was visible in addition to small sp^2 and sp^3 peaks after annealing, while only intense sp^2 and sp^3 peaks were shown before annealing [60-61]. It is of note that the ratio of sp^3 to sp^2 peak was slightly reduced after annealing (from 62 % reduced to 48 %), revealing similar trend to the change of D/G ratio in Raman spectra, shown in **Figure 3.14a**. In addition, CO_x peak near 288 eV slightly increased after annealing [62]. Similar phenomenon was observed in Si 2p peak (**Figure 3.18c, d**). Before annealing, the main peak near 102.2 eV was SiO_x peak with additional Si-Si peak near 99.3 eV [62]. After annealing, SiO_x content was slightly increased due to ambient oxidation, in good agreement with C 1s peak analysis. More importantly, Si-C peak near 100.8 eV appeared after annealing [60]. The Si-C peak shown in C 1s and Si 2p after annealing comes from chemical bonding between CNF and Si at the interface. This peak is small due to narrow interface region, which is hardly observable by Raman spectroscopy, as shown in Figure 3a. The presence of such Si-C bonds at the interface may not contribute to Li storage but plays an important role in strengthening adhesion of Si layer to CNFs and furthermore efficient charge transfer at the interface during

lithiation/delithiation process [63-64].

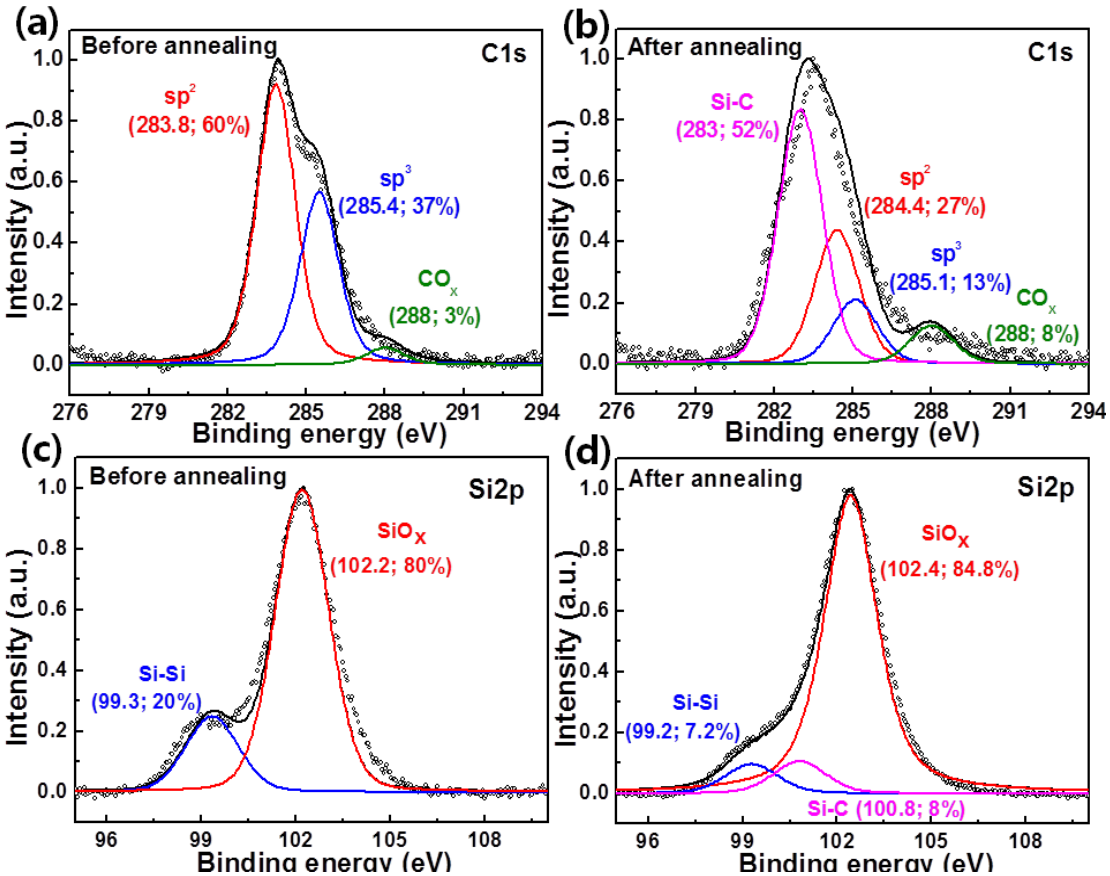

Figure 3.18. High-resolution XPS spectra of Si/CNF with 200 cycles of Si deposition before and after annealing. Figure (a) and (c) are C 1s and Si 2p fitted peaks before annealing. (b) and (d) are C 1s and Si 2p fitted peaks after 1000 °C annealing. Peak positions and relative ratios are shown in the figure.

3.3.3 Anode Performance of CNF-Si Mat

The electrochemical performance of bare CNF and Si/CNF mat was investigated in $LiPF_6$/EC+ DEC solution. For better comparison, the bare CNF

mat was annealed (indicated as CNF-a) at the same condition as the composite mat. The electrochemical performance comparison between CNF-a and non-annealed CNF was shown in **Figure 3.19.** In **Figure 3.19a**, lithiation/delithiation occurred below ~ 0.3 V in the cathodic/anodic scan which resembled the characteristic of hard carbon in the case CNF [35,38]. However, the cathodic peak below 0.1 V and the anodic peak at ~ 0.1 V belong to the characteristic of Li intercalation/deintercalation into graphitic layers in CNF-a [65-66].This manifests that our as-fabricated CNF mat contains a certain degree of graphitization and disordered phase which is consistent with **Figure 3.14a** and **Figure 3.18** and also the improved graphitization degree of CNFs after 1000 °C annealing. In **Figure 3.19b**, the impedance profiles show decrease of both series resistance (the starting point) and charge transfer resistance (the radius of semicircle) after 1000 °C annealing. This again can be attributed to the higher graphitization degree of CNF after annealing.

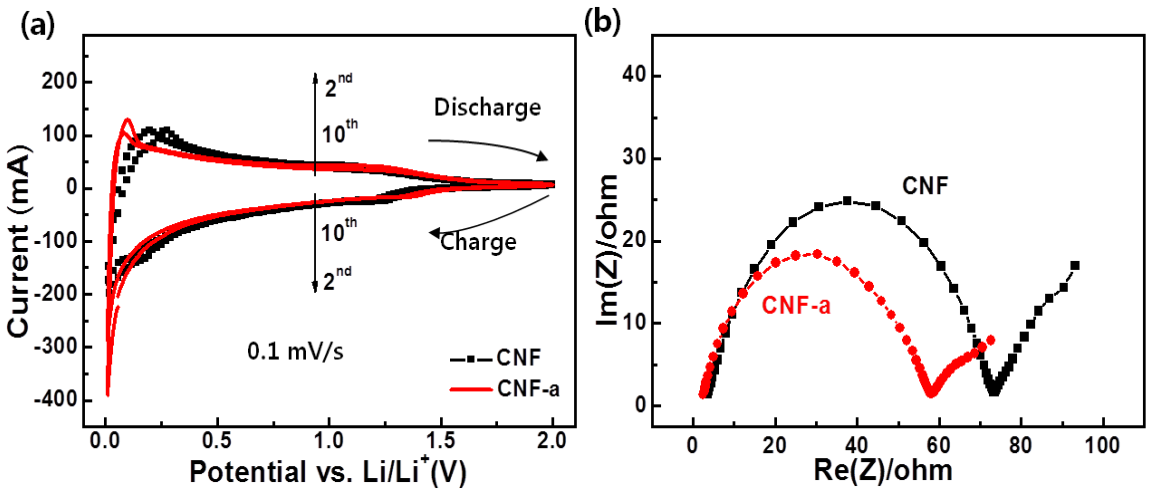

Figure 3.19. (a) CV profile comparison between bare CNF mat and CNF mat after 1000 °C annealing. The curves were recorded after 1st CV scan between 0.01 to 2 V at a scan rate of 0.1 mV s^{-1}. (b) AC impedance spectra of the above two electrodes. The spectra were recorded right after the cell assembling before cycling.

The CV curves of CNF-a and Si/CNF mat with 200 cycles of Si deposition were shown in **Figure 3.20a**. In the case of Si/CNF mat, no appreciable peaks related to Li_xSi alloy formation were observed in Si-200-p (dashed line). On the contrary, two pairs of redox reaction peaks were observed in Si-200-a (solid line). The sharp cathodic peak at ~ 0.01 V can be attributed to a combination effect of CNF mat and c-Si/a-Si. The cathodic peak (Li alloy) at 0.2 V and anodic peaks (Li dealloy) at 0.37 V and 0.52 V are due to the formation of amorphous Li_xSi phase and delithiation back to a-Si, respectively [67-68]. The increase of the peak intensities of a-Si with increasing the scan cycle numbers can be ascribed to the conversion of the μc/nc-Si into amorphous phase during the repeated CV scans. The electrochemical analysis in **Figure 3.20a** provides us further understanding of the Si crystallinity which is again in good agreement with **Figure 3.14a**.

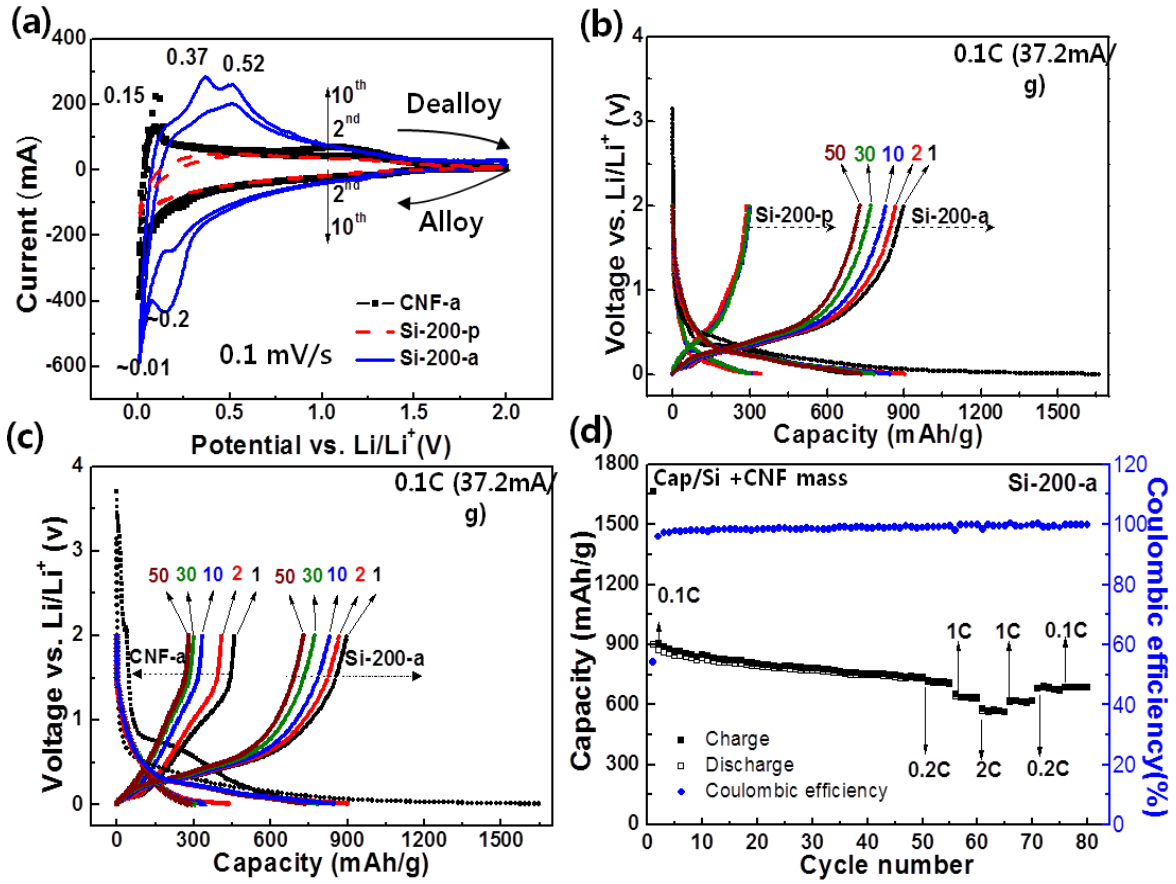

Figure 3.20. (a) The 2nd and 10th cyclic voltammograms of CNF-a (square), Si-200-p (dashed line) and Si-200-a (solid line) mats between 0.01 and 2 V at a scan rate of 0.1 mV s^{-1}. (b) and (c) are voltage profiles of Si-200-p/Si-200-a and CNF-a/Si-200-a between 0.01 and 2 V at a charging rate of 0.1 C. The cycle numbers are indicated in the figure. (d) Charge/discharge capacity and Coulombic efficiency of Si-200-a for the first 80 cycles.

The 1, 2, 10, 30, 50th galvanostatic charge/discharge (CD) profiles between

0.01 and 2 V of Si/CNF mat with 200 cycles deposition before/after 1000 °C annealing are plotted in **Figure 3.20b.** The CD rate was 0.1 C, where 1 C is defined to be 372 mA h g^{-1}. Compared to Si-200-p which delivers a capacity around 300 mA h g^{-1}, Si-200-a exhibited much higher capacity of almost 900 mA h g^{-1} at 1^{st} discharge and 730 mA h g^{-1} at 50^{th} discharge according to the total mass of Si and CNF with an average fading rate of 0.34 % per cycle. This can be attributed to the presence of a mixed phase of Si (c-Si and a-Si) and also the improved material purity after annealing by removing the electrolyte residues as discussed. **Figure 3.20c** is the galvanostatic CD profiles of CNF-a mat and Si-200-a. The CD profiles of CNF-a mat has already explained in **Figure 3.10**. Compared to CNF-a mat, the Si-200-a sample showed a large capacity of 1650 mA h g^{-1}in the 1^{st} charge and a higher capacity by almost three times (730 mA h g^{-1}) after 50^{th} cycles, since Si contains a higher Li storage capacity than carbon. However, the large capacitance loss of the first cycle related to the formation of the SEI layer was observed. **Figure 3.20d** shows capacity retention of the Si-200-a sample at the specific charging rates. The discharge capacity at the 2^{nd} cycle was 710 mA h g^{-1} at 0.2 C, 637 mA h g^{-1} at 1 C and 565 mA h g^{-1} at 2 C. The Coulombic efficiency is defined as the ratio of the discharge to charge capacity and plotted in the same figure. The Coulombic efficiency of Si-200-a sample approached to 54 % at the 1^{st} cycle due to the SEI formation and increased to 99 % after 20 cycles at 0.1 C rate. The value was smaller than the ideal efficiency because of the reformation of SEI layer on newly exposed Si during cycling with

a cost of Li consumption [69]. Compared to the Si thin film on the two dimensional Cu substrate, the improved cyclic life was attributed to the highly porous three dimensional CNF substrate and also the unique Si spaghetti structure, which can both accommodate Si volume expansion. The comparison between our work and previous publications with respect to the different fabrication methods of Si/CNF composite structure was shown in **Table 3.1**. It is clear to see that our result showed reasonable capacity and also capacity retention. More importantly, our structure involved no metal substrate compared to others.

Table 1. Anode performance comparison of silicon/CNF composites fabricated by different methods. CNF film is usually fabricated by mixing CNF powder with a binder. CNF mat is binder-free freestanding film fabricated by electrospinning method.

Structure	Si deposition Method	Mass [mg cm^{-2}]	Si mass ratio	Current density [mA g^{-1}]	Capacity@cycles [mA h g^{-1}] *[a]*	Capacity retention	Remarks	Structural features
Si@CNF[44]	CVD	2	75 %	500	1600@55	80 %	film	Metal substrate
Si@CNF[45]	CVD	4	37 %	50	766@20	80.3 %	film	CF mesh as a substrate
Si@Hollow CNF[46]	CVD	—	25 %	0.5C*[b]*	750@100	68.2 %	film	Metal substrate
Si@CNFs[47]	Sputtering	0.4	16 %	50	1200@105	90 %	film	Metal substrate
Si@VACNFs[48]	Sputtering	0.2	49 %	323	2752@ 100*[c]*	89 %	—	VACNFs grown on metal substrate
SiNWs@CNF[49]	VLS	3.6	80 %	342	1400@40	77 %	film	—
Si/CNF[50]	Si NPs in DMF & electrospinning	—	16 %	100	773@20	90.4 %	mat	Metal substrate
Si/CNF[51]	As above	1.6	26 %	50	726@40	46.8 %	mat	Metal substrate
Si-CNF core-shell[52]	As above	—	50 %	240	1300@100	1	film	Metal substrate
Si/CNF[53]	Si NPs in DI & electrospinning	—	41 %	35	892@50	—	mat	Metal substrate
Si/CNF (Ours)	**Electro-deposition**	**1**	**43 %**	**37**	**730@50**	**85 %**	**mat**	**No substrate No binder**

[a] Capacity is calculated based on silicon & carbon mass. *[b]* C rate is not mentioned in the reference. *[c]* Capacity is calculated based on silicon mass.

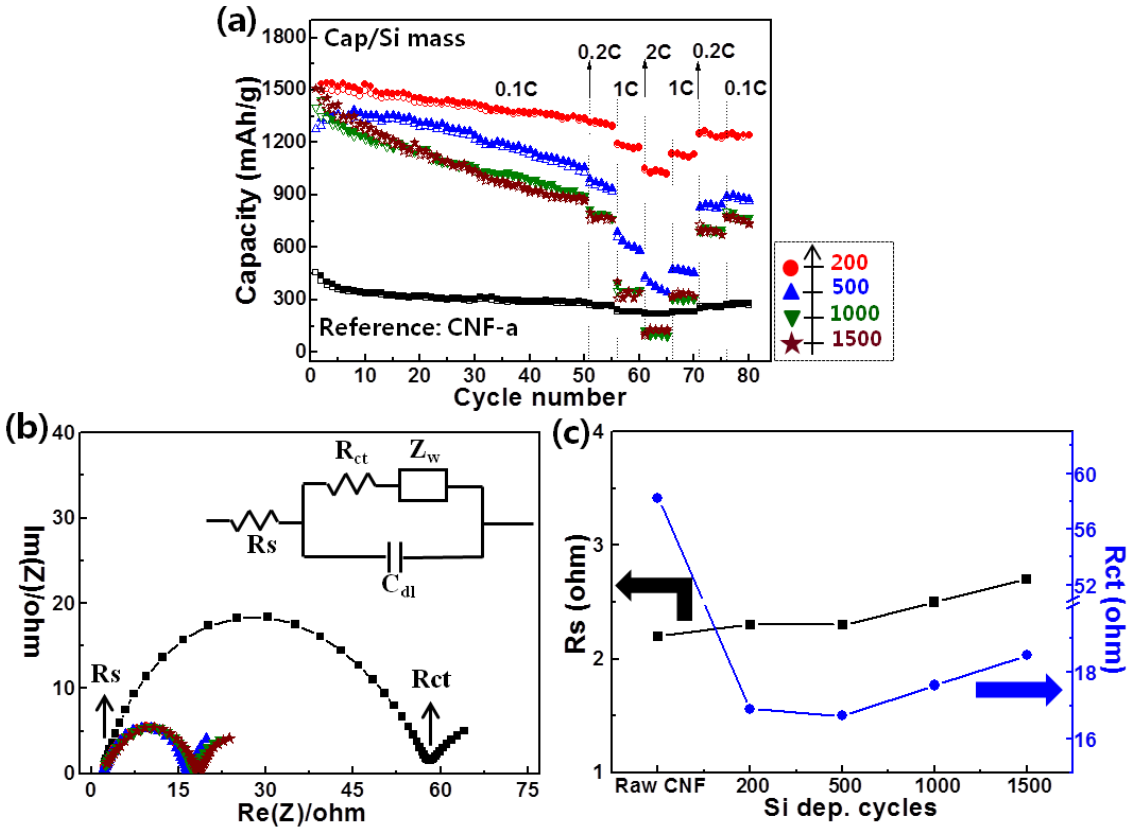

Figure 3.21. (a) Charge (filled symbols)/discharge (open symbols) capacity in terms of different numbers of silicon deposition cycles after high temperature annealing. Capacity was calculated based on silicon mass only. Sample indications are shown in the right dashed square. (b) AC impedance spectra of the above five electrodes. The spectra were recorded right after the cell assembling before cycling. The equivalent circuit is shown in the inset. The related resistance value in Figure (b) was plotted in Figure (c) with respect to different silicon deposition cycles.

For better understanding of the structure-related Li storage capacity, different Si amount was deposited on the CNF mat by varying the number of electrodeposition cycles. The capacity retention of Si/CNF mats (all after 1000 °C annealing) upon the different Si deposition cycle numbers are summarized in **Figure 3.21a.** Here, the specific capacity was expressed in terms of net Si mass excluding carbon mass. The specific capacity with respect to net Si mass from the composite was calculated from the following equation:

$$Q_{Si} = m_{CNF}/m_{Si} \{Q_{composite} (1+ m_{Si}/m_{CNF}) - Q_{CNF}\}$$

where "$Q_{composite}$" is the total capacity of CNF-Si composite according to the total mass of Si+CNF electrode. Q_{Si} (Q_{CNF}) is the specific capacity based on the net mass of Si (CNF). Here m_{Si} (m_{CNF}) is the mass of deposited Si (CNF) in the composite. The values of specific capacity was ~ 1545 mA h g^{-1} at the beginning of charge/discharge and were similar to each other regardless of the Si deposition cycle numbers. However, capacity retention became poorer as the Si loading amount increased, for example, the capacity of 200 and 1500 Si electrodeposition cycles was 1354 mA h g^{-1} and 873 mA h g^{-1}, respectively. As the Si thickness increases, deformation energy of Si increases as well, inducing more crack initiation and propagation. In other words, in the case of thicker Si layers, crack generation caused by volume variation is more significant [43]. Therefore, thicker Si layer peels off easily and eventually the capacity degradation occurs more severely than that of thinner Si layer. The cohesive energy of Si-C bonds at

the interface between Si and CNF is helpful for structure stabilization against the increased deformation energy. Deformation energy is proportional to the thickness, while interfacial energy is constant. When deformation energy exceeds interfacial cohesive energy at critical layer thickness of Si, the structure of Si breaks down. On the other hand, Si shape transformation was observed from spaghetti-like to granule-like when CV deposition cycles keep increasing from 200 to 1500, as shown in **Figure 3.22**. The thin Si layer fabricated with 200 cycles CV deposition revealed a highly porous structure (See **Figure 3.16**), and therefore the volume expansion can be minimized compared to the thick granular shape Si layers.

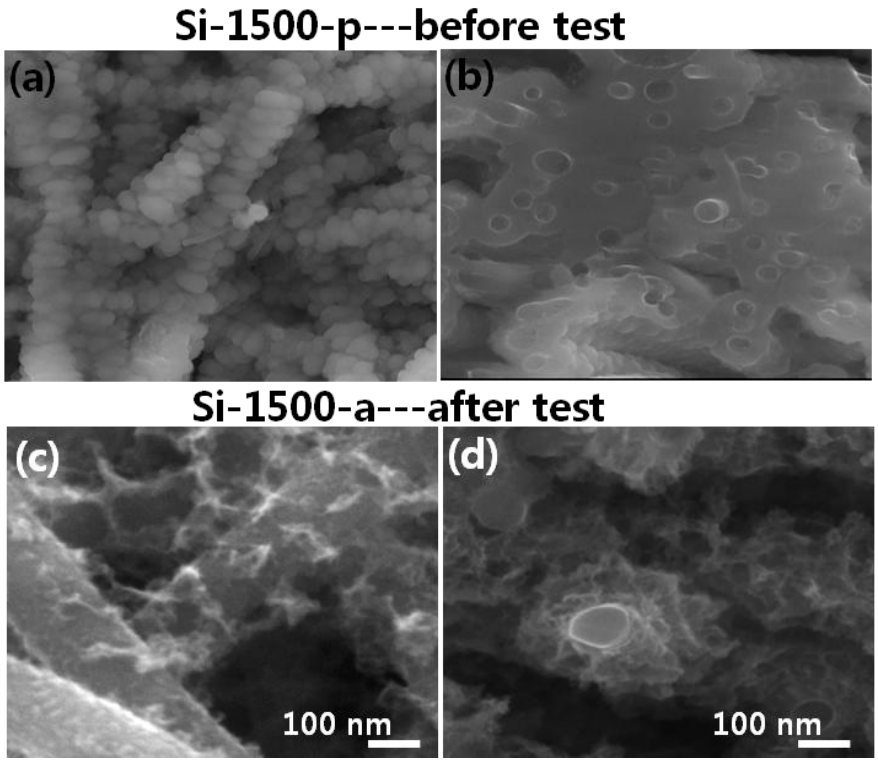

Figure 3.22. SEM images of (a-b) Si-1500-p and (c-d) Si-1500-a samples.

Nyquist plots of Si/CNF mat with different Si loading masses are plotted in **Figure 3.21b**. The curves were collected right before electrochemical charge/discharge cycling. All of the curves showed a depressed semicircle and a tail, which indicates the mixed kinetics and diffusion process. The semicircle in the high frequency range indicates the charge transfer resistance (R_{ct}) at the interface between electrode and electrolyte. The tail at low frequency region implies a diffusion-controlled process. An equivalent circuit is shown in the inset where R_s, C_{dl}, and Z_w represent respective series resistance of electrolyte/electrolyte contact, double layer capacitance, and Warburg impedance related to the diffusion of ions in the bulk electrode [70-71]. The value of R_s (first point) and R_{ct} (diameter of semicircle) were extracted from **Figure 3.21b** and replotted in **Figure 3.21c**. As the Si loading amount increased, R_s slightly increased due to lower conductivity of Si. The R_{ct} decreased sharply with Si deposition and then increased gradually as the Si coating amount increased. The origin of large value of R_{ct} observed in bare CNF-a sample compared to the Si-coated CNF sample could be the morphology difference between CNF-a and Si. The Si shell exhibited much rougher surface than that of bare CNF-a (**See Figure 3.16**), which benefited the charge transfer process through large surface area. The different lithiation mechanisms between silicon and carbon may also play a role

here. The increase of R_{ct} in Si/CNF mat with increasing Si deposition cycles is attributed to the larger granular size and less porosity of the deposited Si layers (See **Figure 3.22a**). The straight line can be interpreted as the resistance for the diffusion process of lithium ions into the electrode. The smaller angle between real axis and the straight line as the Si loading amount increases simply indicates again the limited diffusion of Li ions with increasing Si loading amount.

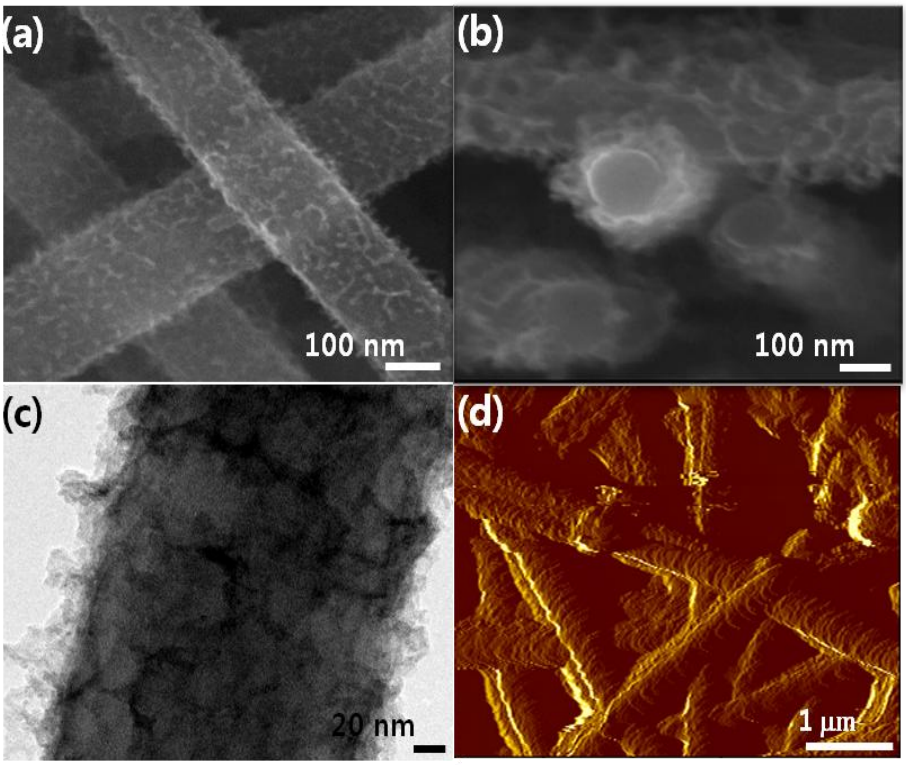

Figure 3.23. Charaterizations of Si-200-a electrode after 80 cycles charge/discharge. (a) Top-view SEM image, (b) Cross-sectional SEM image, (c) High resolution TEM image, and (d) AFM image. The SEI layer was selectively removed by washing the sample with acetonitrile

and diluted HCl.

Figure 3.23a and b show SEM images for the structural changes of Si-200-a after cycling test. The SEI layer was selectively removed by using acetonitrile and then HCl prior to imaging [72]. Si layer became rough hairy and highly porous, compared to the one before cycling test in **Figure 3.16**. The lower density of Si suggested that some spaghetti type Si at the outermost surface was removed, as can be seen in the TEM image of **Figure 3.23c**. This is why capacity was degraded during cycling. Nevertheless, compared to the sample with hgiher Si loading amount **(Figure 3.22c**,**d**), the major portion of Si remained after cycling test (See AFM image of **Figure 3.23d**), retaining relatively high capacity and reasonable capacity retention. This is in fact corroborated to the robust Si-C bonds formed at the interface between Si and CNF which was achieved by 1000 °C annealing. Free-standing CNF mat assembled through electospinning process without a binder or a metal substrate is a good platform to provide such robust Si-C bonds due to abundant existence of sp^3 bonds at the surface of CNF, as discussed in **Figure 3.14** and **Figure 3.18**.

3.4 Summary of Chapter Three

In this chapter, general introduction of common one dimensional carbon materials like CNFs and CNTs has been given. Compared to higher conductivity of CNTs, CNFs exhibit an easier Li insertion pathway and a cost effective

property which make them a good candidate for anode of LIB. Especially, the electrospinning method synthesized free-standing CNF mat has been intensively studied in this work since it prevents the use of metal substrate, binder and conducting polymers which usually increase the mass of electrode, degrade the long term stability and reduce the anode capacity. Due to the unsatisfied capacity of as-fabricated CNF mat, Si, a high capacity media was introduced into the three dimensional CNF network through electrochemical deposition. Once again, the structure involves neither a metal substrate nor binders. This could help us in designing anode structures with high capacity and long cycle life in an economic way. Thermal annealing of the combined mat at 1000 °C was necessary to remove undesired residues formed during electrodeposition process and to form strong Si-C bonds at the interface between Si layer and CNFs, which eventually improved adhesion of Si to CNF and furthermore facilitated efficient charge transfer between Si and CNF during lithiation/delithiation. This resulted in clear improvement of the capacity of carbon materials more than twice for most of cases. Optimization to improve composite structures for capacity, charge transfer, and cycle life is further required for industry applications.

Bibliography of Chapter Three

[1] R. Feynman, Caltech's Engineering and Science Magazine **1960**.

[2] Y. Ren, R. A. Armstrong, F. Jiao, G. P. Bruce, *J. Am. Chem. Soc.* **2010**,*132,* 996.

[3] D. S. Su, R. Schlögl, *ChemSusChem* **2010**, *3*, 136.

[4] A. S. Airco, P. Bruce, B. Scrosati, J.Tarascon, W. V. Schalkwijk, *Nature Mater*. **2005**, *4*, 365.

[5] N.M. Rodriguez, A. Chambers, R.T.K. Baker, Langmuir **1995**, *11*, 3862.

[6] M. Endo, Y.A. Kim, T. Fukai, T. Hayashi, K. Oshida, M. Terrones, T. Yanagisawa, S. Higaki, M.S., Appl. Phys. Lett. **2002**, *80,* 1267.

[7] S.H. Yoon, S. Lim, Y. Song, Y. Ota, W.M. Qiao, A. Tanaka, I. Mochida , Carbon **2004,** *42*, 1723.

[8] S.H. Yoon, C.W. Park, H.J. Yang, Y. Korai, I. Mochida, R.T.K. Baker, N.M. Rodriguez, Carbon **2004,** *42*, 21.

[9] Springer Handbook of Springer Handbook of Nanomaterials 2011, chapter 7.

[10] J. Prasek, J. Drbohlavova, J. Chomoucka, J. Hubalek, O. Jasek, V. Adamc, R. Kizek, *J. Mater. Chem.* **2011**, *21*, 15872.

[11] N. Saifuddin, A. Z. Raziah, A. R. Junizah, *J. Mater. Chem.* **2013**, http://dx.doi.org/10.1155/2013/676815.

[12] T. Belin, F. Epron, *Materials Science and Engineering B* **2005**, *119*,105.

[13] J. Zhao, A. Buldum, J. Han, *Phys. Rev. Lett*. ***2000***, *85,* 1706.

[14] A.S. Claye, J.E. Fischer, C.B. Huffman, A.G. Rinzler, R.E. Smalley, *J.*

Electrochem. Soc. **2000**, *147*) 2845

[15] W. Lu, D.D.L. Chung, *Carbon* **2001,** *39*, 493 – 496.

[16] H. Shimoda, B. Gao, X.P. Tang, A. Kleinhammes, L. Fleming, Y.Wu, O. *Zhou, Phys. Rev. Lett. 2002, 88. 015502.*

[17] H. H. Lee, C. C. Wan, Y. Y. Wang, Journal of Power Sources 2003,1,7.

[18] C. Casas, W. Li, *Journal of Power Sources* **2012**, *208*, 74.

[19] T. Kar, J. Pattanayak, S. Scheiner, *J. Phys. Chem. A* **2001**, *105*, 10397.

[20] C. K. Chan, H. Peng, G. Liu, K. McIlwrath, X.Zhang, R. A. Huggins, Y.Cui. *Nature Nanotech.* **2007**, *3*, 31.

[21] S. Ramakrishna, K. Fujihara, W.-E. Teo, T.-C. Lim, Z. Ma, *World Scientific*, Singapore **2005**.

[22] D.H. Renecker, A.L. Yarine, H. Fong, S. Koombhongse, *J. Appl. Phys.* **2000,** *87*, 4531.

[23] Y.M. Shin, M.M. Hohman, G.C. Martin, Polymer **1999**, ***40***, 7397.

[24] I.D. Norris, M.M. Shaker, F.K. Ko, A.G. MacDiarmid, Synth. Met. **2000,** *114*, 109 – 114.

[25] F. Ko, Y. Gogotsi, A. Ali, N. Naguib, H. Ye, G. Yang, C. Li, P. Willis, Adv. Mater. **2003**, *15*, 1161.

[26] C. Vozzi, C.J. Flaim, F. Bianchi, A. Ahluwalia, S. Bhatia, *Sci. Eng.* **2002,** *20*, 43.

[27] C. Kim, K.S. Yang, *Appl. Phys. Lett*. **2003,** *83*, 1216.

[28] R. Dersch, M. Steinhart, U. Boudriot, A. Greiner, J.H. Wendorff, Polym. Adv. Technol. **2005**, *16*, 276.

[29] K. Aoki, Y. Usui, N. Narita, N. Ogiwara, N. Iashigaki, K. Nakamura, H. Kato, K. Sano, N. Ogiwara, K. Kametani, C. Kim, S. Taruta, Y.A. Kim, M. Endo, N. Saito, Small **2009**, *5*, 1540.

[30] C. Kim, K.S. Yang, M. Kojima, K. Yoshida, Y.J. Kim, Y.A. Kim, M. Endo Adv.Funct. Mater. **2006**, *16*, 2393.

[31] R. Bacon: Production of graphite whiskers, *J. Appl. Phys.* **1960,** *31*, 283.

[32] J. Doshi, D. H. Reneker, *Journal of Electrostatics* **1995,** *35*, 151**.**

[33] N. T. Xuyen, E. J. Ra, H. Z. Geng, K. K. Kim, K. H. An, Y. H. Lee, *J. Phys. Chem. B* **2007**, *111*, 11350.

[34] K. Nakamoto, in *Infrared and Raman spectra of inorganic and coordination compounds. Part A: theory and applications in inorganic chemistry – 6th ed.* Wiley **2009**

[35] P. G. Bruce, B. Scrosati, J. M. Tarascon, *Angew. Chem. Int. Ed.* **2008**, *47*, 2930.

[36] E. J. Yoo, J. Kim, E. Hosono, H. S. Zhou, T. Kudo, I. Honma, *Nano Lett.* **2008**, *8*, 2277.

[37] F. Yao, F. Günes, H. Q. Ta, S. M. Lee, S. J. Chae, K. Y. Sheem, C. S. Cojocaru, S. S. Xie, Y. H. Lee, *J. Am. Chem. Soc.* **2012**, *134*, 8646.

[38] C. C. Li, X. M. Yin, L. B. Chen, Q. H. Li, T. H. Wang, *J. Phys. Chem. C* **2009**, *113*, 13438.

[39] T. D. Hatchard, J. R. Dahn, *J. Electrochem. Soc.* **2004**, *151*, A838.

[40] J. P. Maranchi, A. F. Hepp, A. G. Evans, N. T. Nuhfer, P. N. Kumta, *J. Electrochem. Soc.* **2006**, *153*, A1246.

[41] C. K. Chan, H. L. Peng, G. Liu, K. Mcilwarth, X. F. Zhang, R. A. Huggins, Y. Cui, *Nature Nanotechnology* **2008**, *3*, 31.

[42] H. Wu, G. Chan, J. W. Choi, I. Ryu, Y. Yao, M. T. McDowell, S. W. Lee, A. Jackson, Y. Yang, L. B. Hu, Y. Cui, *Nature Nanotechnology* **2012**, *7*, 310.

[43] H. Wua, Y. Cui, *Nano today* **2012**, *7*, 414.

[44] L. F. Cui, Y. Yang, Ch. M. Hsu, Y. Cui, *Nano Lett.* **2009**, *9*, 3370.

[45] G. K. Simona, B. Maruyama, M. F. Durstock, D. J. Burton, T. Goswami, *J. Power Sources* **2011**, *196*, 10254.

[46] J. Y. Howe, D. J. Burton, Y. Qi, H. M. Meyer III, M. Nazri, G. A. Nazri, A. C. Palmer, P. D. Lake, *J. Power Sources* **2013**, *221*, 455.

[47] P. C. Chen, J. Xu, H. T. Chen, C. W. Zhou, *Nano Res.* **2011**, *4*, 290

[48] S. A. Klankowski, R. A. Rojeski, B. A. Cruden, J. W. Liu, J. Wu, J. Li, DOI: 0.1039/c2ta00057a.

[49] J. W. Choi, L. B. Hu, L. F. Cui, J. R. McDonough, Y. Cui, *J. Power Sources* **2010**, *195*, 8311.

[50] L. W. Ji, K. H. Jung, A. J. Medford, X. W. Zhang, *J. Mater. Chem.* **2009**, *19*, 4992

[51] L. W. Ji, X. W. Zhang, *Energy Environ. Sci*. **2010**, *3*, 124.

[52] T. H. Hwang, Y. M. Lee, B. S. Kong, J. S. Seo, J. W. Choi, *Nano Lett.* **2012**, *12*, 802.

[53] X. Fan, L. Zou, Y. P. Zheng, F. Y. Kang, W. C. Shen, *Electrochemical and Solid-State Lett.* **2009**, *12*, A199.

[54] H. J. Kim, M. H. Seo, M. H. Park, J. P. Cho, *Angew. Chem. Int. Ed*. **2010**, *49*, 2146.

[55] M. Holzapfel, H. Buqa, L. J. Hardwick, M. Hahn, A. Würsig, W. Scheifele, P. Novák, R. Kötz, C. Veit, F. M. Petrat, *Electrochimica Acta* **2006**, *52*, 973.

[56] G. Kanellis, J. F. Morhange, M. Balkanski, *Physical Review B* **1980**, *21*, 1543.

[57] J. E. Smith, Jr., M. H. Brodsky, B. L. Crowder, M. I. Nathan, A. Pinczuk, *Phys. Rev. Lett.* **1971**, *26*,642.

[58] K. Nakamoto, in *Infrared and Raman spectra of inorganic and coordination compounds. Part A: theory and applications in inorganic chemistry – 6th ed.* Wiley **2009**.

[59] X. Chen, K. Gerasopoulos, J. Guo, A. Brown, C. Wang, R. Ghodssi, J. N. Culve, *Adv. Fun, Mater.* **2011**, *21*, 380.

[60] S. Contarini, S. P. Howlett, C. Rizzo, B. A. De Angelis, *Applied Surface Science* **1991**, *51*, 177.

[61] M. Rybachuk, J. M. Bell, *Carbon* **2009**, *47*, 2481.

[62] N. Fourches, G. Turban, B. Grolleau, *Applied Surface Science* **1993**, *68*, 149.

[63] A. M. Wilson, J. R. Dahn, *J. Electrochem. Soc.* **1995**, *142*, 326.

[64] W. Wang, P. N. Kumta, *J. Power Sources* **2007**, *172*, 650.

[65] K. A. Striebel, A. Sierra, J. Shim, C. W. Wang, A. M. Sastry, *J. Power Sources* **2004**, *134*, 241.

[66] M. D. Levi, C. Wang, J. S. Gnanaraj, D. Aurbach, *J. Power Sources* **2003**, *119–121*, 538.

[67] X. L. Chen, X. L. Li, F. Ding, W. Xu, J. Xiao, Y. L. Cao, P. Meduri, J. Liu, G. L. Graff, J. G. Zhang, *Nano Lett.* **2012**, *12*, 4124.

[68] Y. Yao, M. T. McDowell, I. Ryu, H. Wu, N. Liu, L. B. Hu, W. D. Nix, Y. Cui, *Nano Lett.* **2011**, *11*, 2949.

[69] P. R. Abel, Y. M. Lin, H. Celio, A. Heller, C. B, Mullins, *ACS Nano* **2012**, *6*, 2506.

[70] K. Naoi, N. Ogihara, Y. Igarashi, A. Kamakura, Y. Kusachi, K. Utsugi, *J. Electrochem. Soc.* **2005**, *152*, A1047.

[71] J. B. Gong, H. Q. Wu, *Electrochimica Acta* **2000**, *45*, 1753.

[72] H. Wu, G. Y. Zheng, N. Liu, T. J. Carney, Y. Yang, Y. Cui, *Nano Lett.* **2012**, *12*, 904.

Outline of Chapter Four

Diffusion Mechanism of Lithium Ions through Basal Plane of Layered Graphene

CHAPTER FOUR

Diffusion Mechanism of Lithium Ions through Basal Plane of Layered Graphene

Recently, graphene, composed of monolayer of carbon atoms arranged in a honeycomb network, has emerged explosively and attracted much attention in the fields of materials science and condensed-matter physics. High mobility of graphene is probably the most fascinating properties for physicists and engineers, which is attributed to the linear band dispersion, leading to massless Dirac quasiparticle feasture. On the other hand, as the thinnest carbon material, graphene and graphene-based materials have promising applications in numerous energy sciences, for instance, Li-ion batteries (LIBs), fuel cells, and solar cells. In particular, these materials have superior electrical conductivities to graphitic carbons and higher surface area of over 2600 m^2/g than CNTs, and a broad electrochemical window that would be more advantageous in energy storage. Thus, a series of research works on LIB based on graphene were performed intensively with the similar routes to the CNTs-based electrode materials for LIB [1-6]. Some scientists used graphene sheets directly as an anode material for LIB and found that they had improved electrochemical properties. For example, the first reversible specific capacity of the prepared graphene sheets with a specific surface area of 492.5 m^2/g was as high as 1264 mAh g^{-1} at a current density of 100 mA/g. After 40 cycles, the reversible capacity was still kept at 848 mAh g^{-1} at a current density of 100 mA/g, higher than that of CNTs or CNF electrodes [7].

The interesting single atomic layer structure of Gr can also be used for fundamental science and a good candidate for the fundamental study of Li ion diffusion pathway in addition to its real applications as an anode in LIB. Large area single layer graphene (SLG) which consists of a clean basal plane for the study of Li insertion prevents the coexistence of both edge plane and basal plane in graphite that often hinders the understanding of lithium ion diffusion mechanism. Therefore, in this chapter, after a brief introduction which includes the general properties and production methods of Gr, the diffusion mechanism of lithium ion through basal plane of layered graphene has been intensively studied. In this case, two types of graphene samples were prepared by chemical vapor deposition (CVD): i) well-defined basal plane single layer graphene grown on Cu foil, ii) edge plane-enriched graphene layers grown on Ni film. Electrochemical performance of graphene electrodes has been examed based on different number of graphene layers and also different defect population on graphene basal plane. Density functional theory calculations were also provided to clarify the diffusion barrier heights for various types of defects.

4.1 Brief Introduction of Two Dimensional Graphene

4.1.1 General Physical Properties of Graphene

Graphene, as a two-dimensional (2D) honeycomb lattice structure consists of sp^2-hybridized carbon atoms in the form of one-atom thick planar sheet. This

unique material is a basic building block for many other carbon-based graphitic materials such as zero-dimensional (0D) fullerenes, one-dimensional (1D) carbon nanotubes, and three-dimensional (3D) graphite and is an excellent basic model for many other 2D materials (**Figure 4.1**) With its unique structure, graphene exhibits extraordinary thermal, mechanical, and electrical properties, which makes it a popular material in many different research areas, theoretically and experimentally.

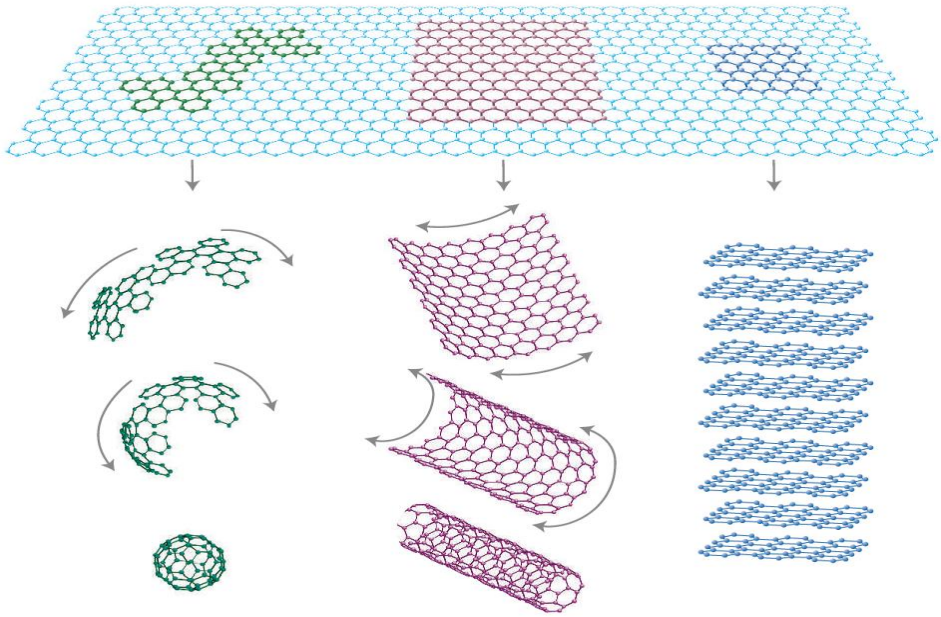

Figure 4.1. Graphene is a basic 2D building block for other carbon allotropes with different dimensionalities. Cited from Ref.[8].

The unusual electronic properties of graphene are originated from its unique

band structure. In the lattice of graphene, carbon atoms are located at each corner of hexagons binding with three neighboring carbon atoms. Carbon atom has four valance electrons, of which three of them were used for covalent σ-bonding with adjacent carbon atoms in graphene lattice. The remaining π-orbital determines the electronic structure of graphene which is "coupled" with the other π-electrons on adjacent carbon atoms. Each π-electron is delocalized, i.e., has a "field of influence" of 360 degrees around its own carbon atom within an individual graphene layer. The unit cell of graphene contains two π-orbitals (π and π*), which disperse to form two π-bands that can be considered as bonding (the lower energy valence band) and anti-bonding (the higher energy conduction band) in nature.

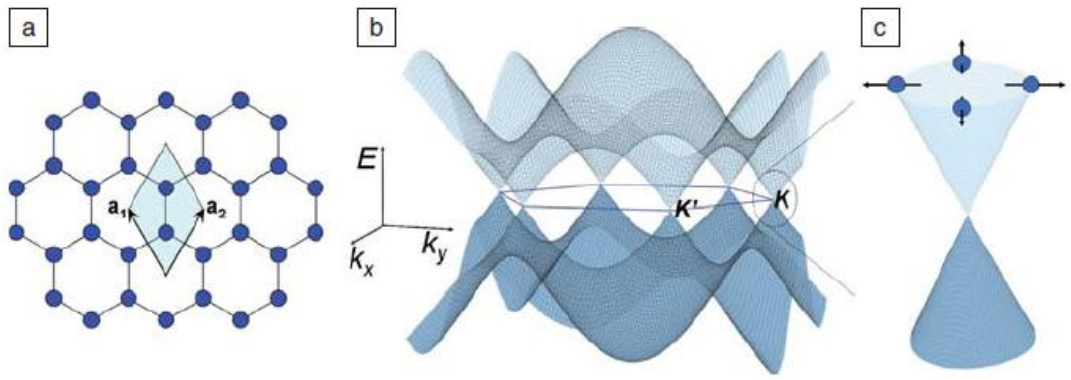

Figure 4.2. a) Honeycomb lattice of graphene with two carbon atoms per unit cell. b) Tight-binding band structure of graphene π-bands, considering only nearest neighbor hopping. c) Band structure near K point showing the linear dispersion relation. Cited from Ref. [9].

The bonding-antibonding gap closes at the corners of the Brillouin zone, or the K points. (See **Figure 4.2**) As a result, the π-band dispersion is approximately linear around the K points: $E = \hbar v_F |k|$ where k is the wave vector measured from K, $\hbar$ is Planck's constant, h divided by 2π, and v_F is the Fermi velocity in graphene, approximately 10^6 m/s. Since the electrons in graphene have kinetic energies exceeding their mass energy, electrons behave like photons or ultra-relativistic particles with an energy-independent velocity v_F that is approximately 300 times smaller than the speed of light in vacuum, allowing relativistic effects to be observed in graphene without using particle accelerators [9]. These quasiparticles, called massless Dirac fermions, can be seen as electrons that have lost their rest mass m_0 or as neutrinos that acquired the electron charge e [10]. This linear (or "conical") dispersion relation at low energies, electrons and holes near these six points, two of which are inequivalent, behave like relativistic particles described by the Dirac equation for spin 1/2 particles [11]. Dirac fermions behave in unusual ways when compared to ordinary electrons if subjected to magnetic fields, leading to new physical phenomena [12-14] such as the anomalous integer quantum Hall effect (IQHE) measured experimentally [14-15]. The IQHE in graphene can be observed at room temperature because of the large cyclotron energies for "relativistic" electrons [16]. In fact, the anomalous IQHE is the signature of Dirac fermion behavior. With these properties, graphene is a perfect mixture of semiconductor (zero density of states) and a gapless metal which is quite different from other metals

and semiconductors with its very long mean free paths (**Figure 4.3**).

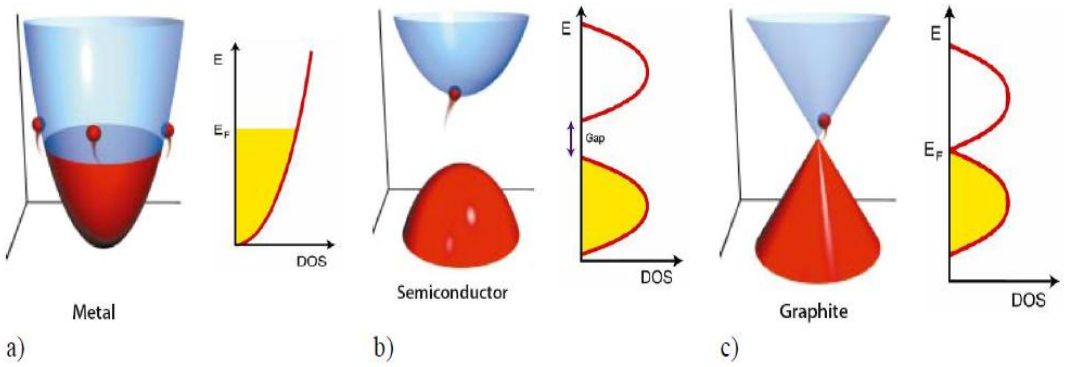

Figure 4.3. Electronic Structure of: a) Metal: Finite Density of States (DOS) at Fermi energy. b) Semiconductor: Gap at Fermi energy. c) Graphene: Zero gap Semiconductor. Zero DOS metal. Cited from Ref. [18].The interesting 2D structure of graphene makes it a good candidate for electronic device applications [17]. Unlike an ordinary metal, in which any impurities in the crystal scatter electrons and so lead to energy loss, the electrical resistance in graphene is independent of the number of impurities. This means that electrons can travel for several microns without colliding with impurities, making graphene a promising material for a potential high-speed electronic switching devices called a "ballistic transistor". Experimental transport measurements show that graphene has a unusual high electron mobility even at room temperature in excess of 15,000 $cm^2v^{-1}s^{-1}$, of which mobilities for holes and electrons are nearly same [9,14,18-19].

Graphene has a number of other extraordinary properties such as strong

mechanical properties and high flexibility allowing strain based graphene electronics [20-21]. Another important aspect of graphene is its high thermal conductivity up to 5000 W/mK at room temperature, 20 times higher than that of copper, which could be exploited to applications in microelectronics and thermal management structures [22]. Its optical properties are strongly related to its electronic properties such as its low energy electronic structure where conical bands of electron and hole meet at the Dirac point resulting in unexpected high opacity. An atomic monolayer of graphene absorbs $\pi\alpha \approx 2.3\%$ of white light, where α is the fine-structure constant [23]. It has been shown that graphene system exhibits electrochromic behavior, allowing tuning of both linear and ultrafast optical properties [24-25].

4.1.2 Synthesis Methods of Graphene

First attempts to understand graphene basic properties was made by micro-cleavage method, which is a simple method to isolate graphitic layers from graphite into monolayer graphene flakes with the help of a cohesive tape [26]. Although many basic electronic properties of graphene such as the bipolar transistor effect, ballistic transport of charges, large quantum oscillations, *etc.*, was explored by this method, for the large area graphene applications it was necessary to find other synthesis methods (**Figure 4.4**). For this purpose, epitaxial synthesis of graphene on different substrates was realized. Many

important graphene properties have been identified in graphene produced by SiC substrate. In this method, the face of SiC, silicon or carbon-terminated, is used for graphene formation in ultra high vacuum furnaces at very high temperatures (>1100 ^{o}C) to decompose SiC into graphene [27]. Another approach for epitaxial growth of graphene is studied on metal substrates, such as ruthenium, iridium, and nickel [28-30]. Although these substrates have been employed to obtain graphene, the interaction of graphene with underlying substrate and conducting behavior of these substrates necessitated the transfer of graphene layers onto other substrates for the application. Synthesis of large area few-layered graphene together with transferring onto another substrate has been realized by chemical vapor deposition (CVD) method on polycrystalline metallic substrates such as Ni and Cu [31-33]. Unlike the epitaxial growth techniques, CVD method has been realized by decomposition of carbon gases such as ethylene and methane followed by either carburization-precipitation, or surface adsorption of carbon gases. To fabricate devices, graphene, then, can be transferred by polymethylmethacrylate (PMMA) as a supporting layer after dissolving the underlying metallic substrate in a metal etchant and "fishing" the single-layer graphene up onto a desired substrate (*e.g.*, SiO_2/Si). This method will be explained in detail later. Graphene has been also derived from graphite oxide by thermal annealing or chemical reduction by hydrazine [34-35]. This method combining with the typical powder process (involves metal current collector and binders) as mentioned in chapter three has been considered as one of the most

popular one used in battery electrode fabrication. However, graphene produced by graphite oxide reduction is lower in quality compared to graphene obtained by aforementioned production methods due to incomplete removal of various functional groups by existing reduction methods.

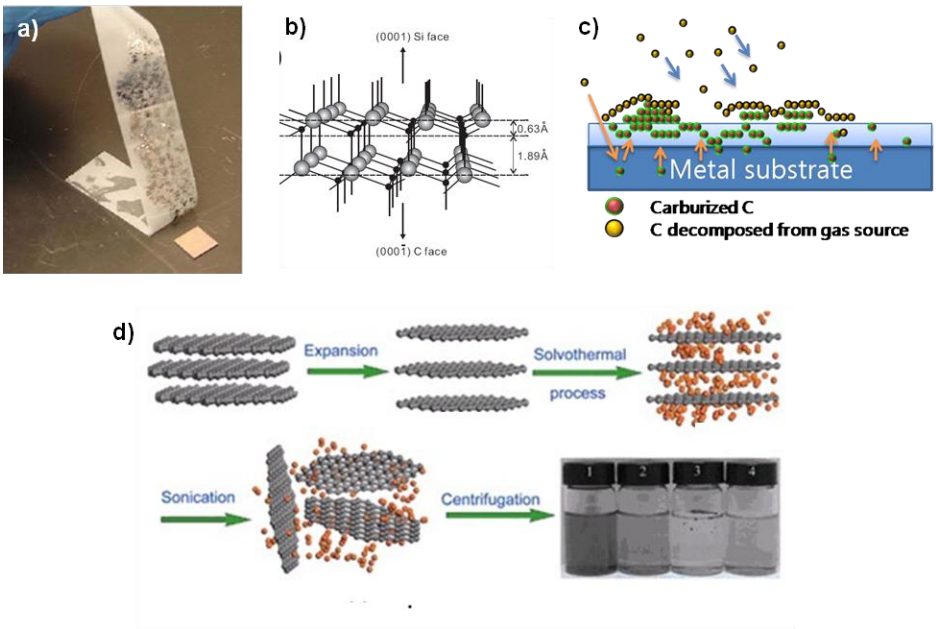

Figure 4.4 Production techniques of graphene: a) Micro-cleavage method, isolating graphitic layers from graphite into monolayer graphene flakes with the help of a cohesive tape, b) epitaxial growth of graphene by decomposition of SiC into graphene, c) chemical vapor deposition method by decomposition of hydrocarbon gases on metal substrates, and d) chemical exfoliation of graphite oxide by weakening van der Waals cohesive force via insertion of reactants into interlayer space.

4.2 Diffusion Mechanism of Lithium Ions through Basal Plane of Layered Graphene

Graphite has been widely used for anode material in lithium ion battery due to its well defined layered structure for lithium intercalation, low operating potential, and remarkable interfacial stability [36]. Graphite has two characteristic planes: basal plane and edge plane which are parallel and perpendicular to the c-axis, respectively. It is known in general that the basal plane and edge plane exhibit different physical and chemical activities in many aspects, leading to different lithiation capabilities in graphite [37-38]. The diffusion time constant for Li ion insertion within the active graphitic flakes is governed by the formula $\tau = L^2/2D$, where L is the diffusion length (or radius of spherical flake) and D is diffusion coefficient [39]. Although lithium diffusion through basal plane is rather limited, lithium diffusion may still occur through several defect sites such as vacancies and grain boundaries [40-41]. Lithium diffusion through edge plane of graphitic flakes can be easily facilitated but further complicated by the presence of different functional groups such as hydroxyl and carboxyl groups. In other words, lithiation through these two different planes is highly anisotropic [42-46].

One ambiguity in understanding diffusion pathway of lithium ions in graphite is the coexistence of both edge plane and basal plane in the sample. The presence of these two different interfaces is unavoidable in conventional graphite [32,47]. Currently available highly oriented pyrolytic graphite (HOPG), which is

well known as highly ordered crystallographic structure, has a finite size of flakes whose edge planes are still abundant in addition to basal planes. Therefore, lithium ion diffusion through basal plane cannot be observed exclusively [40-43].Thus, a well defined basal plane of graphite with large area is required to have a comprehensive picture of lithium diffusion mechanism in lithium ion battery.

Recently large area monolayer and multi-layer graphene have been synthesized by chemical vapor deposition (CVD) [32,47]. This paves a new route for exploring numerous new fundamental sciences and moreover developing numerous technological breakthroughs in electronics and energy storage [48-50]. Large area graphene can be transferred onto any substrate by a simple transfer process and therefore an anode electrode with layered graphene without leaving edge plane (or negligible portion of edge plane) is easily attainable. This provides an opportunity to study diffusion of lithium ions exclusively through the basal plane of graphene.

On the other hand, in lithium ion battery, corrosion of conventional current collectors such as Al, Cu, and stainless steel (SUS) can adversely affect life time and safety through increased internal resistance, passivation of active materials, and consumption of electrolyte/ active electrode materials [51-57]. Anode performance of thin graphene layers can be misguided by the strong substrate

reaction since the most reactive lithium ions exist in electrolyte [58-59]. It has been proposed that monolayer graphene can be used as a protective layer for substrate against air oxidation and mild electrochemical reaction [60-61]. Therefore, information on the critical layer thickness of graphene (l_c) to minimize the substrate effect and the influence of defects to l_c are key ingredients to understand electrochemical reaction and protective nature of graphene layers under severe electrochemical condition.

The main purpose of this work is twofold: i) To clarify lithium diffusion pathway through basal plane of graphene layers and ii) to investigate the influence of defect population to lithium ion diffusion and the protective ability of graphene layers. In this article, we prepared Cu-grown monolayer graphene (SLG) samples and Ni-grown multi-layered graphene (MLG) samples that are dominated with graphene basal plane and edge plane, respectively. We found that the electrochemical performance of few-layer graphenes (FLGs) which are overlapped up to three layers of SLG is strongly affected by the substrate reaction. Experiments with Ar plasma treatment indicated that 6 layers of basal plane-enriched large area graphene were needed to provide sufficient substrate protection. Combing the experimental results and density functional theory calculations, we proved that basal plane hindered lithium ion diffusion with a high diffusion barrier height, whereas divacancies and higher order defects can be shortcuts for lithium ion diffusion.

4.2.1 Material Preparation

Large area SLG was synthesized on copper foil by atmospheric pressure (AP) CVD. Cu foil purchased from Nilaco (Lot No. 113321, 99.96 %, 100 μm in thickness) was preannealed to 1060 °C for two hours with 100 sccm of Ar gas and 200 sccm of H_2 gas to enlarge Cu grain size and then chemico-mechanically polished with $FeCl_3$ solution for flattening. The prepared Cu foil was then brought into the growth chamber. The temperature of the chamber was heated up to 1060 °C with 1000 sccm of Ar gas and 200 sccm of H_2 gas for 20 min. Methane (5sccm) was then introduced with 10 sccm H_2 gas for 5 min. After growth, the sample was cooled down to room temperature naturally in the same atmosphere. In the case of MLG synthesis, Ni thin film (300 nm) was deposited on SiO_2 (300 nm)/Si by a thermal evaporator. This was placed in rapid thermal CVD chamber. Temperature was increased to 1000 °C in 5 min in vacuum. Ni surface was reduced by flowing 45 sccm H_2 gas at 1000 °C. The gas mixing ratio of C_2H_2:H_2 was optimized to 2:45 sccm and flown for a minute. After completion of growth, the gas supply was terminated and the chamber was cooled down to room temperature. The detail has been described elsewhere [62-63].

4.2.2 Transfer Process of a Graphene

PMMA (e-beam resist, 950 k C4, Microchem) was spin-coated on the graphene/Cu foil (Ni film) at 1000 rpm for 60 s. To etch away Cu foil (Ni film), the sample was submerged in a copper etchant (CE-100, Transene) for ~30 min

(4 hours for Ni film). After rinsing by deionized water for a few times, PMMA/graphene layer was fished onto the CR 2032 cell case coated with lithium-reaction resistive polymer, as shown in **Figure 4.5**. PMMA was removed by acetone later after graphene was completely dried and attached onto the cell case. The transferred sample was then annealed up to 650 °C for 5 h in high vacuum (1 x 10^{-6} Torr) for further removal of PMMA [63-64].

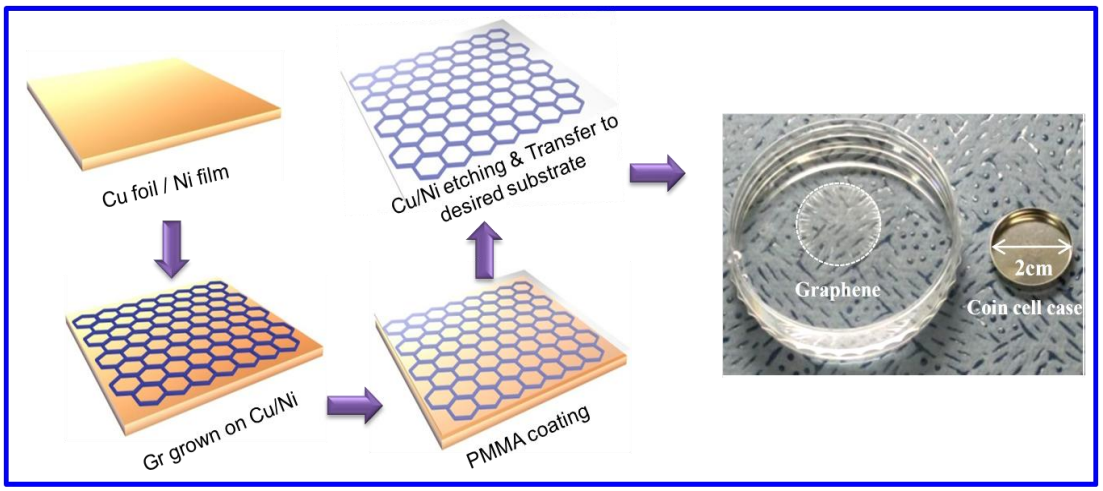

Figure 4.5. Schematic of fabrication process with Cu-grown SLG or Ni-grown MLG (left panel). Bilayer and trilayer graphene can be fabricated by transferring monolayer graphene repeatedly. Photograph of as-prepared monolayer graphene (PMMA on top) floating in water and CR 2032 coin cell case (right panel).

4.2.3 Characterization of a Graphene

Figure 4.6 shows a schematic of the CR 2032 coin cell type battery. The half cell was then fabricated with a counter/reference electrode of Li foil for the test of Li diffusion through well defined basal graphene plane (Figure 1f). Bilayer and trilayer graphene coin cells were also fabricated by transferring monolayer graphene repeatedly. MLG was synthesized on Ni film to represent graphene where the edge plane was enriched and the half cell was fabricated similarly.

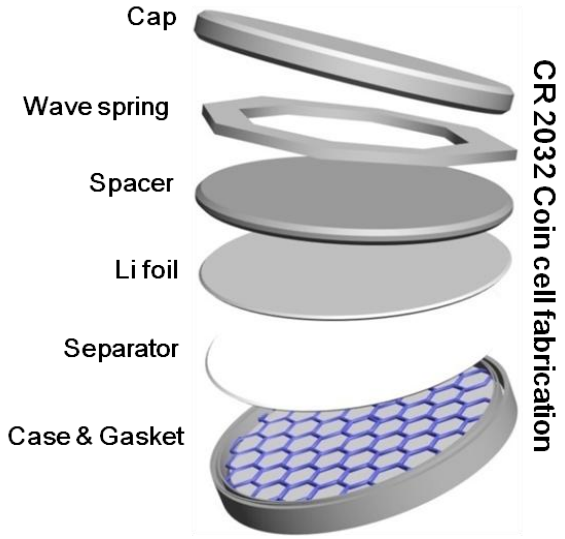

Figure 4.6. Schematic of a coin cell structure with Cu-grown SLG or Ni-grown MLG. Bilayer and trilayer graphene coin cells were fabricated by transferring monolayer graphene repeatedly.

In order to clarify the quality and layer number of graphene, a series of characterization was done, as shown in **Figure 4.7**. **Figure 4.7a** and **b** are optical

micrographs of the transferred SLG and MLG on SiO_2/Si substrate, respectively. The SLG grown on Cu foil was rather flat except small portion (~ 4%) of bilayer and trilayer graphene domains represented by the dark spots (arrows) in the image (**Figure 4.7a**). Some wrinkles indicated by the white dashed lines introduced during transfer process were also visible. Contrary to this, Ni-grown MLG showed multi-layered flakes represented by the white spots (arrows) in **Figure 4.7b**, creating numerous edge planes, as can be visualized in **Figure 4.7c**. Micro-Raman spectra in **Figure 4.7d** clearly show G-band near 1590 cm^{-1}, which is related to optical E_{2g} phonon at the Brillouin zone center indicating sp^2 hybridization of carbon network, and G'-band around 2694 cm^{-1}, which is also known as 2D-band, an overtone of D-band, in both samples [66]. Large G'/G intensity ratio (~ 2) with a small D-band near 1350 cm^{-1}, which corresponds to transverse optical phonon near the K point and indicates sp^3 hybridization of carbon network, was observed in SLG, indicating high quality monolayer graphene. On the other hand, the intensity ratio of G'/G which is less than one reveals multi-layered properties of Ni-grown graphene. Defect distribution was shown in the images of confocal Raman mapping of D/G intensity ratio in **Figure 4.7e** and **Figure 4.7f**. Defects indicated by bright spots were scattered uniformly over the surface, while grain boundary lines were faintly visible in SLG. Small flakes were visible in MLG (**Figure 4.7f**). Although D-band intensity was barely visible in **Figure 4.7d**, we clearly observed from D/G band mapping that some defects were distributed in both samples. Transmittance of

each graphene layer transferred onto PET substrate was provided in **Figure 4.7g**. The transmittance of SLG was 96.5%, slightly smaller than HOPG value of 97.7%, which may be attributed to some portion of multi-layered domains formation as described in **Figure 4.7a** [67]. Correspondingly, bilayer and trilayer graphene samples revealed a systematic reduction in the transmittance. The Ni-grown MLG showed 63.6% of transmittance, corresponding to 15 layers in average by assuming 2.3 % absorption per each layer [68]. Optical photographs were provided to visualize different transmittances with different number of graphene layers in **Figure 4.7h**.

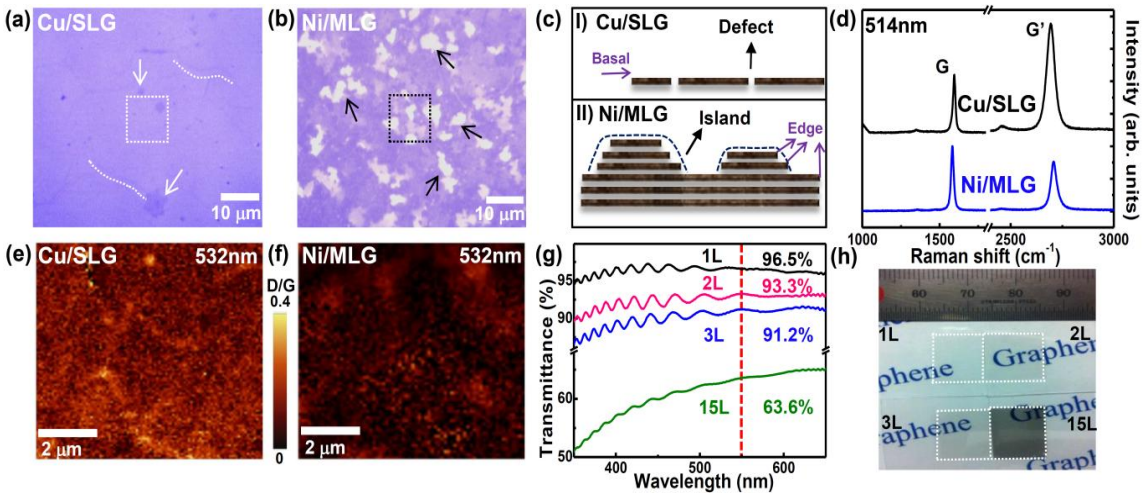

Figure 4.7. Optical micrographs of (a) Cu-grown SLG and (b) Ni-grown MLG on SiO_2/Si substrate. White dashed lines indicate wrinkles. Some portion of thicker graphene is indicated by arrows. (c) Schematic of (i) SLG with a well defined basal plane and (ii) edge plane enriched MLG. (d) Micro-Raman spectra of SLG and

MLG. Confocal Raman mapping of D/G intensity ratio of (e) SLG and (f) MLG from squared positions of (a) and (b). The contrast is normalized to 0.4 to visualize the defect distribution for both images. (g) Wavelength-dependent transmittance (values are provided at a wavelength of 550 nm) and (h) optical photographs of different number of graphene layers on PET substrate.

4.2.4 Anode Performance of a Graphene

Electrochemical measurements of different layers of Gr samples were performed with a CR2032 coin cell using VMP3 instrument (BioLogic Science Instruments). The cell was assembled in a dry room using CR 2032 cell case with different number of graphene layers and bare foil (SUS 316) as a working electrode, lithium metal foil as a counter/reference electrode, and a 1 M of LiPF6 in a 1:1 (v/v) mixture of ethylene carbonate (EC) and diethyl carbonate (DEC) as an electrolyte. A glassy carbon microfiber was used as a separator. The cells were charged and discharged galvanostatically between 3.0 and 0.01 V at a constant current of 5 μA/cm^2. The AC impedance spectra were obtained by applying a sine wave with an amplitude of 10 mV over a frequency range of 100 kHz to 10 mHz [69]. **Figure 4.8a** shows cyclic voltammograms (CV) of different number of graphene layers at a scan rate of 0.1 mV/s from 0.01 V to 3 V. The bare SUS electrode showed an anodic peak near 1.03 V (S_O) and a cathodic peak around 0.78 V (S_R). These redox peaks involve chemical reactions with Li ions

and possibly electrolytes. Both anodic and cathodic peaks were reduced in the monolayer graphene electrode. These peaks were reduced consecutively in bilayer and trilayer graphene electrodes. It is obvious to see that the redox reaction of the bare SUS electrode was suppressed by the coated graphene layers. An additional cathodic peak appeared near 0.28 V in bilayer and trilayer samples. Origin of these peaks could be ascribed to defect-associated lithium adsorption [41]. At MLG (15 layer graphenes) sample, a sharp cathodic peak near 0.01 V (Li_{In}) is identified as lithium intercalation and a rather broad peak near 0.12 V (Li_{De}) is related to decomposition of graphitic intercalation compound (GIC) stages [58]. It is of note that the bare SUS-related peak was nearly compressed in this case. Both Li_{De} and Li_{In} peaks appeared in this case, in good contrast with FLG samples in which only a clear Li_{In} peak was observed, suggesting that no GIC stages were formed in FLGs. The distinct CV behavior of FLGs and MLG demonstrates that lithium ion intercalation becomes more effective in MLG induced by the considerable amount of edge planes, as shown in **Figure 4.7b**.

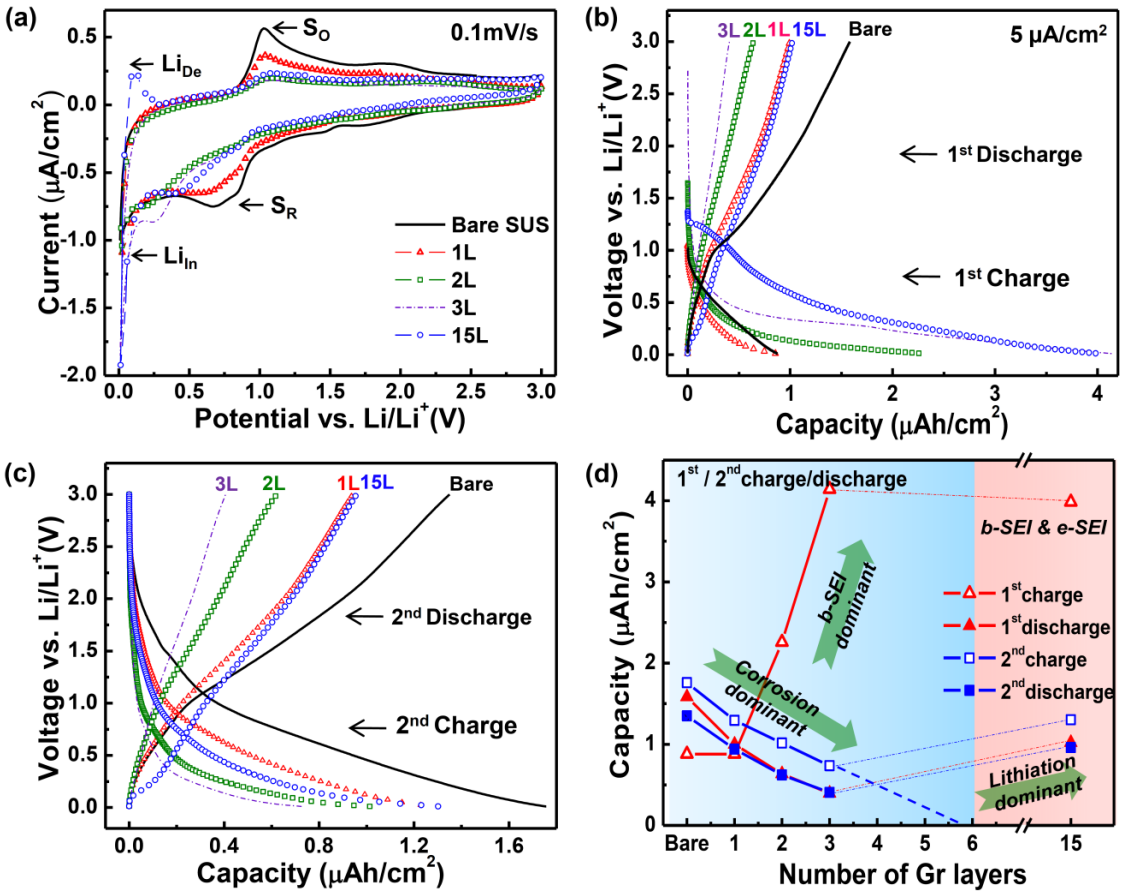

Figure 4.8. (a) Cyclic voltammograms of different number of graphene layers samples at a scan rate of 0.1 mV/s. SUS-related redox reaction peaks (S_O, S_R) and lithium intercalation/deintercalation related peaks (Li_{In}/Li_{De}) are marked in the figure. (b) 1st and (c) 2nd galvanostatic charge/discharge profiles of different number of graphene layers at a current density of 5

μA/cm^2. (d) The related layer-dependent capacities. Two regimes of corrosion-dominant and lithiation-dominant are indicated.

Figure 4.8b shows the 1st galvanostatic charge/discharge profile with a voltage sweeping range of 0.01 ~ 3 V at a constant current of 5 μA/cm^2. As the number of graphene layers increased, long tail appeared in the charge curve at low voltage region. At MLG sample, a plateau appeared in the range of 1.25 - 0.6 V. In graphitic material, the solid-electrolyte interface (SEI) formation via electrolyte decomposition takes place in the range of less than 1.0 V [43, 68, 70-71]. The SEI formation potential varies with types of graphite planes. In general, SEI forms at higher potential in edge plane than in basal plane [72-74]. Therefore, we ascribed this plateau in MLG to edge plane-related SEI formation. In the 2nd cycle, the voltage profile shows a gradual change in a wide range of voltages during charge/discharge, revealing a V-shape curve, i.e., no plateau region, as shown in **Figure 4.8c**. This is in good contrast with a U-shape curve in graphite electrode, where the edge plane intercalation is dominant in the plateau region of low voltage within 0.1 V [68,75] Capacities of graphene coated electrodes in **Figure 4.8c** were consistently smaller than that of the bare electrode, and furthermore much smaller by about 30 times than the recently reported graphene battery result [51]. The huge capacity difference comes from the use of different substrates, as shown in **Figure 4.9**.

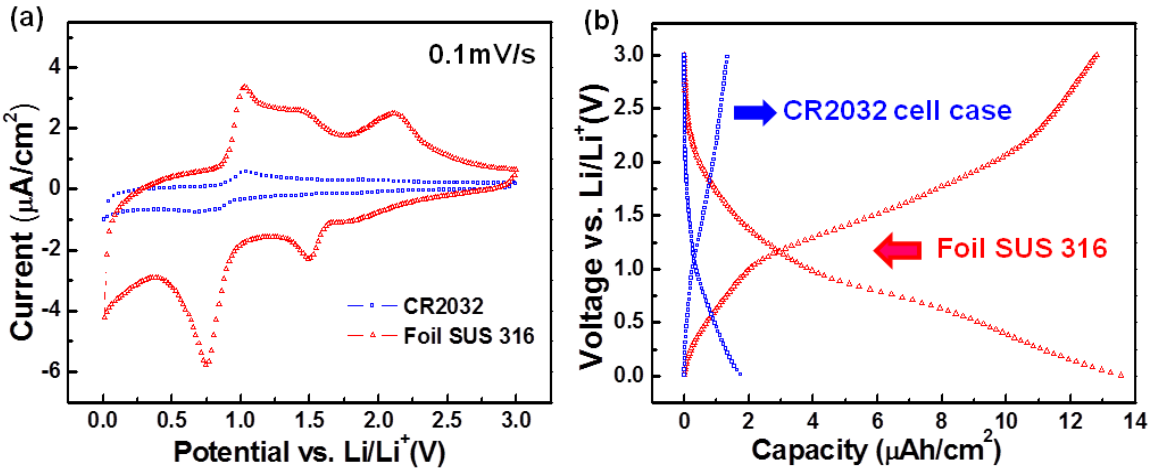

Figure 4.9. Cyclic voltammograms at a scan rate of 0.1 mV/s (a) and 2nd galvanostatic charge/discharge profiles (b) at a current density of 5 μA/cm^2 of bare CR2032 coin cell case and foil SUS 316.

Abundant reaction peaks and larger area of CV curve indicate that more severe corrosion reaction occurs in the case of foil SUS 316 in **Figure 4.9a**. The capacity indicating substrate corrosion intensity obtained from the cell case in **Figure 4.9b** shows almost 8 times smaller than that of the SUS 316. This huge capacity difference can be attributed to the corrosion resistive polymer coated on the cell case. The capacity of bare foil SUS (~14 μAh/cm^2) is still smaller than the reported value for graphene on Cu substrate (~ 40 μAh/cm^2) in Ref. 53, i.e., Cu reaction is much stronger than SUS 316 reaction. Therefore, the relative higher capacity can be understood by the effect of Cu substrate.This also implies

that in spite of graphene layers coated on the electrode with well defined basal plane, the reaction with electrode did occur inevitably.

The related layer-dependent capacities are summarized in **Figure 4.8d**. As the number of graphene layers increased, the 1st charge capacity increased rapidly up to trilayer graphene electrode and saturated at the MLG electrode. As described in the schematic of **Figure 4.7c**, the basal plane is exposed during lithiation up to three layers, whereas both edge plane and basal plane are present in 15 layers. Two different types of SEI are formed: i) basal-plane associated SEI (b-SEI) which is formed up to 3 graphene layers and ii) edge-plane associated SEI (e-SEI) which is formed in MLG sample. It has been known that b-SEI formed at lower potential is associated with solvent reduction, while e-SEI formed at higher potential is associated with salt ions [72-74, 43]. Since our basal plane contains abundant defect sites, as observed from **Figure 4.7d** and **e**, some decomposed solvent molecules may further diffuse into the subjacent layers along with Li ions or in a form of lithium salvation and form additional b-SEI layer. This is why b-SEI increases as the number of graphene layers increases at FLG samples. At MLG electrode, both b-SEI and e-SEI are formed. Although e-SEI increases in this case, b-SEI is reduced compared to FLG electrodes due to the decrease of effective basal plane area of 15 layers (See **Figure 4.7c**) and therefore the capacity from SEI formation is saturated in the 1st charge.

On the other hand, the 1st discharge capacity decreased gradually up to three layer graphene electrode and increased at 15 layer electrode. Similar trend was also observed in the 2nd charge/discharge profile. The discharge capacities of the 2nd cycle were not much different from those of the 1st cycle. Large capacity of the bare SUS electrode was reduced by coating graphene layers up to three layers. This gradual reduction was also expected from the reduced areas of CV curves in FLGs (**Figure 4.8a**). This implies several facts: i) SUS substrate reaction is systematically suppressed with increasing number of graphene layers ii) Because lithium ions can diffuse through basal plane of graphene, monolayer graphene is not sufficient to prohibit substrate reaction. Since the pure basal plane presumably does not allow Li diffusion, the diffusion may be provoked through some defect sites that exist on the graphene plane, as observed from the D/G intensity ratio of confocal Raman mapping in **Figure 4.7e**. This will be described later in detail. In FLG samples, If we presume capacity only to be contributed from intercalation (0.028 $\mu Ahcm^{-2}$ / interlayer in the case of LiC_6), the intercalation capacity reaches 0.056 $\mu Ah/cm^2$ at trilayer graphene sample. This value is negligible to the capacity (0.73 $\mu Ah/cm^2$) observed in our experiment. This tells us that even if intercalation of lithium ions was invoked, the observation was still obscured by the dominant SUS redox reaction. By noting a linear decrease of the capacity and hence extrapolating to a minimum capacity, l_c to sufficiently prohibit the SUS redox reaction is predicted to be ~ 6

layers. As the number of graphene layers increases, the capacity from the SUS redox reaction decreases, while the capacity reduction will be compensated by the intercalation capacity between graphene layers. After 6 layers, the capacity starts increasing by the pure intercalation. We can define substrate corrosion-dominant region up to 6 layers and lithiation-dominant region after 6 layers, as visualized in **Figure 4.8d**.

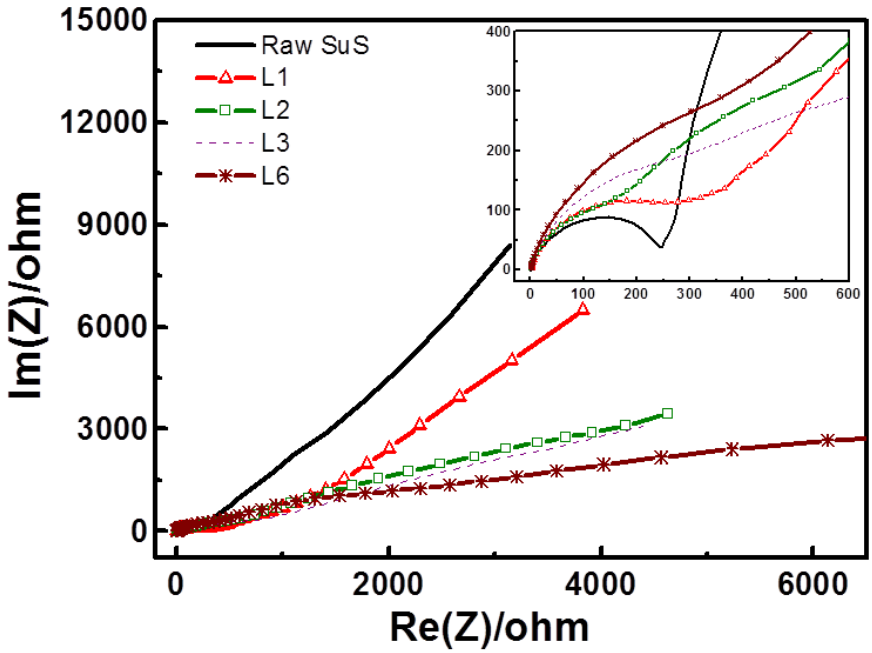

Figure 4.10. AC impedance spectra obtained by applying a sine wave with an amplitude of 10 mV over a frequency range from 100 kHz to 10 mHz. The inset shows impedance at higher frequency region to demonstrate charge transfer resistance.

In order to get the complete image of substrate-related corrosion behavior, we performed AC impedance measurement to 6 layers of graphene in the full frequency range of 100 kHz to 10 mHz by applying a sine wave with an amplitude of 10 mV, as shown in **Figure 4.10**. All of the impedance spectra consisted of a depressed semicircle in higher frequency (**Figure 4.10** inset) and a straight line with different angles to the real axis in the lower frequency range. The depressed semicircle usually can be deconvoluted into two semicircles, resulting from SEI formation and charge transportation. Since this measurement was carried out without any charge/discharge test, the formation of the SEI would be minimized. Therefore, the main contribution of this semicircle could be attributed to the charge transport. The charge transport resistances of graphene-coated samples were obviously larger than that of bare SUS coin cell case which can be indicated by the increased diameters of semicircles. Smaller angles of graphene electrodes than SUS electrode in the straight line region again demonstrated difficulty of lithium ion diffusion into graphene electrodes. All of these proved that graphene can be a good protective layer by limiting the ion diffusion process at the SUS/graphene interface. Especially, at six layers of graphene electrode, the charge transport resistance is largest and the angle of straight line is smallest compared to the electrodes coated with one, two, and three layers of graphene. This is because further overlapping of larger area

graphene can further minimize lithium ion diffusion which will provide much better protective ability compared to less number of graphene layers.

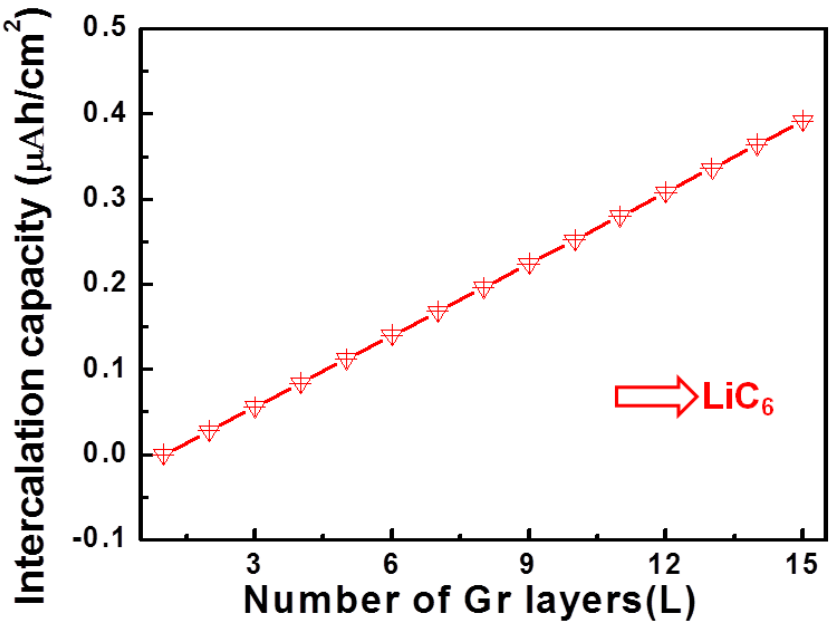

Figure 4.11. Theoretically estimated capacity based on LiC_6 intercalation. No absorption of Li ions occurs at monolayer graphene.

The theoretically estimated capacity at 15 layers (or effectively 9 layers, see **Figure 4.11**), is 0.2 μAh/cm^2. However, this value is still far smaller than the observed value of 1.30 μAh/cm^2. This extra capacity could be ascribed to the lithium adsorption on defects of the graphene surface, which can be supported by the widely distributed defects observed from confocal Raman mapping in our experiments (**Figure 4.7f**). In the 2nd cycle, the discharge capacity was smaller

than the charge capacity consistently, nearly independent of the thickness of graphene layers. This difference of 0.35 μAh/cm^2 in the charge/discharge capacity is irreversible capacity and can be ascribed to strongly adsorbed lithium ions on defects such as vacancies or grain boundaries formed on the graphene layers. This will be discussed in the theory section later.

Since defects on graphene basal plane seem to play an important role in lithium diffusion, a systematic study is required for comprehensive analysis. Thus, structural defects of graphene were created by Ar^+ bombardment with different plasma powers (15W, 100W) for one minute. The transferred graphene was brought into vacuum chamber with a base pressure of 1 x 10^{-6} Torr and then filled with Ar gas of 100 sccm for a minute, followed by the plasma ignition. This was repeated layer by layer to obtain Ar^+ plasma-treated FLG samples. **Figure 4.12a** shows Raman spectra of Ar plasma-treated monolayer graphene. At 15 W plasma power, D/G intensity ratio was increased to 0.56 from 0.19 in no plasma-treated pristine graphene, implying structural defect formation in the graphene plane. At 100 W, one additional peak near 1620 cm^{-1} (D') appeared in addition to further increase of D-band intensity (D/G intensity ratio is 1.66), indicating plausible formation of structural defects. No peak splitting of G-band into G^+ and G^- peaks indicates that our process does not involve strain-induced effect. **Figure 4.12b** shows CV diagrams for SLG electrode with different plasma powers at a scan rate of 0.1 mV/s. It is obvious to see that the redox

reaction peak intensities of S_O and S_R related peaks were enhanced and the related peak positions were also shifted after plasma treatment. Those peaks are a combination of defect-associated adsorption and SUS substrate reaction, as mentioned in **Figure 4.8a**. Additional redox reaction due to the generated basal plane defects by plasma treatment is provoked. Since the protective layer is monolayer graphene, extra lithium ions adsorbed on defects could easily reach the SUS substrate, thus increasing the substrate redox reaction. The 2^{nd} galvanostatic charge/discharge capacity of SLG increased accordingly compared to the pristine graphene sample, as shown in **Figure 4.12c**. The enhanced capacity was attributed to the increased adsorption of Li ions on defects and increased substrate reaction, as mentioned in **Figure 4.12b**. The 2^{nd} charge capacity kept increasing with increasing plasma power, independent of the number of graphene layers, as summarized in **Figure 4.12d**. The substrate redox reaction was also suppressed, which is identified by the capacity decrease with increasing number of graphene layers similar to that of pristine graphene samples.

Smaller capacity was increased in FLG electrodes compared to that of SLG after plasma treatment and generated different slopes, as shown in **Figure 4.12d**. The absolute slope increased from 0.26 to 0.56 with increasing the plasma power. Extrapolation of these slopes, which determines the critical layer thickness to prohibit substrate reaction, gave rise to l_c of ~ 6 layers independent of the plasma power, i.e., defect population. This is rather surprising, because creation of more

defects in the basal plane is expected to increase basal-plane diffusion of Li ions which will eventually increase substrate redox reaction (See **Figure 4.12b, c**) and thereby larger critical layer thickness should be required after strong plasma treatment. In order to explain this contradictory phenomenon, a schematic of Li diffusion through defects in the basal plane is provided in **Figure 4.12e**. In the case of SLG, Li ion diffusion is allowed through defect sites and no lateral diffusion limitation is expected, since the graphene layer is fully surrounded by Li ions in electrolyte. Therefore, higher defect population will enhance Li ion adsorption and also substrate reaction. In the case of FLGs where large area basal plane is dominant, graphene layers are overlapped with each other so that Li ions will diffuse through defects perpendicular to the plane of top layer first and diffuse along the plane of subjacent graphene layer until they meet another defect site. Since these Li ions may accumulate near the defect sites generated by Ar plasma, Li diffusion along the plane direction will be limited by the steric hindrance from aggregated Li atoms, which is different from the SLG case. Therefore further Li diffusion through graphene basal planes in FLGs is constrained severely by the lateral diffusion at higher defect density. Thus, when FLGs are used as a protective layer, the defects-related lithium adsorption on subjacent graphene layers and actual lithium ion reaction with substrate are suppressed, which is again consistent with the reduction of reaction with substrate are suppressed, which is again consistent with the reduction of the peaks in CV diagram. As a consequence of these phenomena, the critical layer

thickness gives rise to the same value, independent of the defect population. It will be worth mentioning the possibility of forming oxygen-related functional groups on defect sites. Li ions can be also adsorbed on such sites and thus our argument of lateral diffusion suppression by the steric hindrance is still valid.

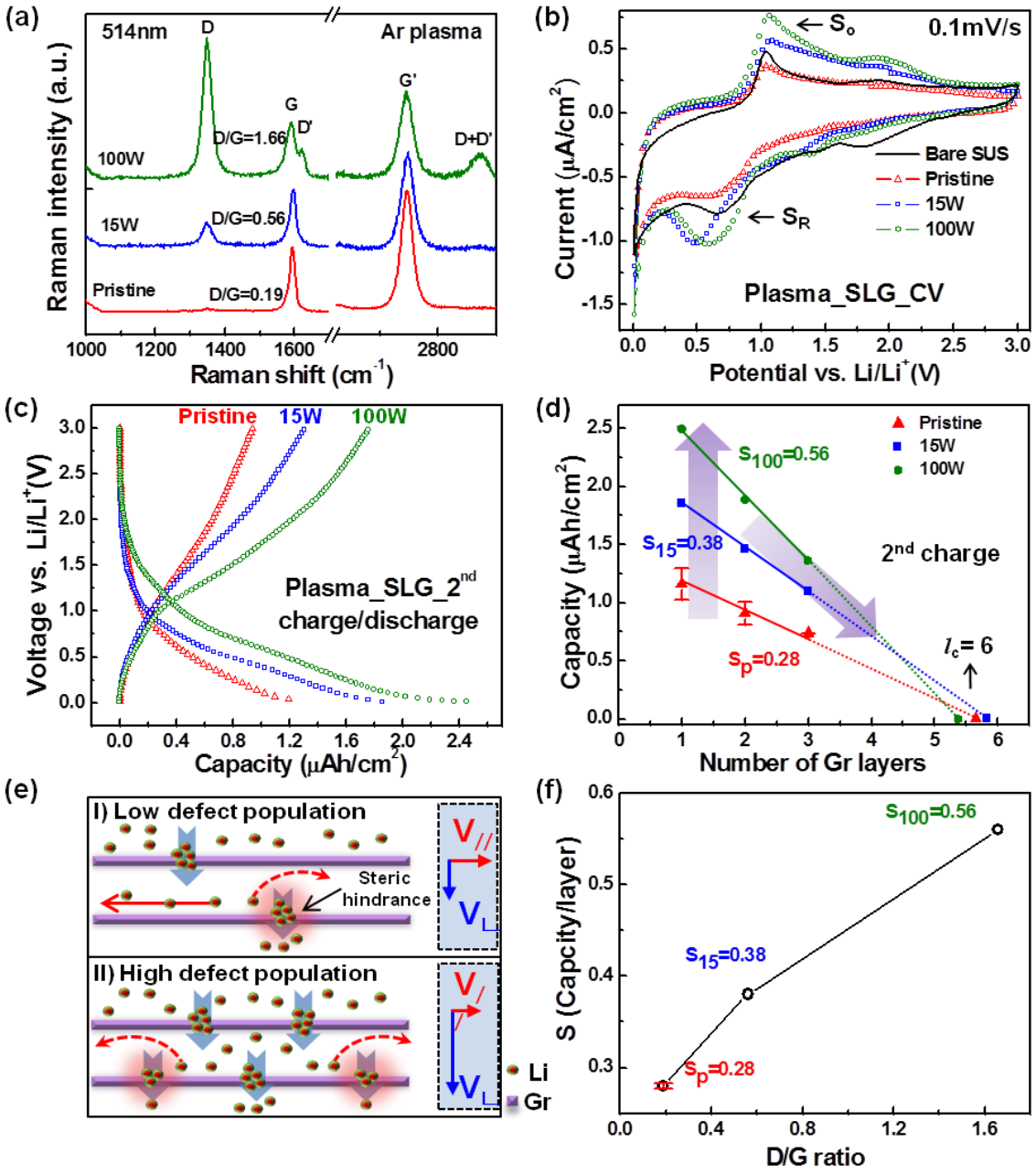

Figure 4.12. (a) Raman spectra, (b) cyclic voltammograms at a scan rate of 0.1 mV/s, and (c) 2nd galvanostatic charge/discharge profiles at a current density of 5 A/cm^2 for monolayer graphene treated by Ar plasma with different plasma powers (15 W and 100 W). (d) Capacity of 2nd charge as a functional of number of graphene layers under different Ar plasma powers. Absolute slopes according to different plasma powers and critical layer thickness (l_c) are indicated in the figure. (e) Schematics of proposed Li diffusion mechanism through defects on the basal plane with different defect population. Broad down arrows indicate Li ion diffusion through defect sites of basal plane. Red glows represent steric hindrance for Li ion diffusion formed by the accumulated Li ions or functional groups. The inset in the right indicates the relative magnitude of diffusion coefficient. (f) Relationship of D/G ratio with the extracted slope from (d).

It is intriguing to see the relationship between D/G intensity ratio from Raman spectra and the slope extracted from charge/discharge profiles, as shown in **Figure 4.12f**. The slope which indicates Li diffusion through graphene layers is correlated to the population of defects in the graphene plane. The larger slope implies the slower diffusion rate and vice versa. Li ion diffusion is limited by the Li aggregates adsorbed on the increased defect sites described in the schematic

Figure 4.12e. Thus, information of Li diffusion obtained from electrochemical test could be used as a metric for evaluating the graphene crystallinity, an important material parameter of graphene.

In order to understand what type of defects allows Li ion diffusion through basal plane of graphene, we conducted density functional theory calculations for various defects: ideal hexagonal site (H site), Stone-Wales defect (SW), monovacancy (V1), and divacancy (V2). The density functional theory calculations were performed within generalized gradient approximation as implemented in DMol3 code. All electron Kohn-Sham wave functions were expanded in a local atomic orbital basis set with each basis function defined numerically on an atomic centered spherical mesh. A double numeric polarized basis sets (DNP) were used for all elements. The dangling bonds of graphene edge were saturated by hydrogen atoms and the atomic cluster structure which consists of 120 carbon atoms and 48 hydrogen atoms were relaxed fully until the force on each atom is less than 10^{-4} eV/Å and the total energy change is less than 5×10^{-5} eV. The damped atom-pairwise dispersion corrections of the form C_6R^{-6} were also considered for calculations. Li adsorption energy was calculated by $E_{ad}(Li) = E_{tot}(Li+carbon) - E_{tot}(Li)- E_{tot}(carbon)$, where $E_{tot}(Li)$ is the self energy of lithium atom and $E_{tot}(carbon)$ is the total energy of carbon system. Various local charges were also calculated using Mulliken, Hirshfeld, and electrostatic potential (ESP).

Table 4.1. Defects related Li adsorption energy, and Li atomic charges calculated by Mulliken, Hirshfeld, and electrostatic potential (ESP) at the minimum energy configurations (M) and the barrier states (B). Positive charge indicates charge depletion from lithium atom.

Binding site	Adsorption energy (eV)	Diffusion barrier height (eV)	Li atomic charge (e)					
			Mulliken		Hirshfeld		ESP	
			M	B	M	B	M	B
H site	-1.69	10.2 (10.7) [a]	0.55	-1.64	0.48	0.20	0.62	0.28
SW	-1.94	6.35	0.53	-1.00	0.44	0.20	0.63	0.67
V1	-3.12	8.86 (10.3) [a]	0.46	-1.05	0.38	0.14	0.71	0.53
V2	-2.36	2.36	0.53	-0.04	0.40	0.18	0.62	0.56

[a] See Ref. [76]

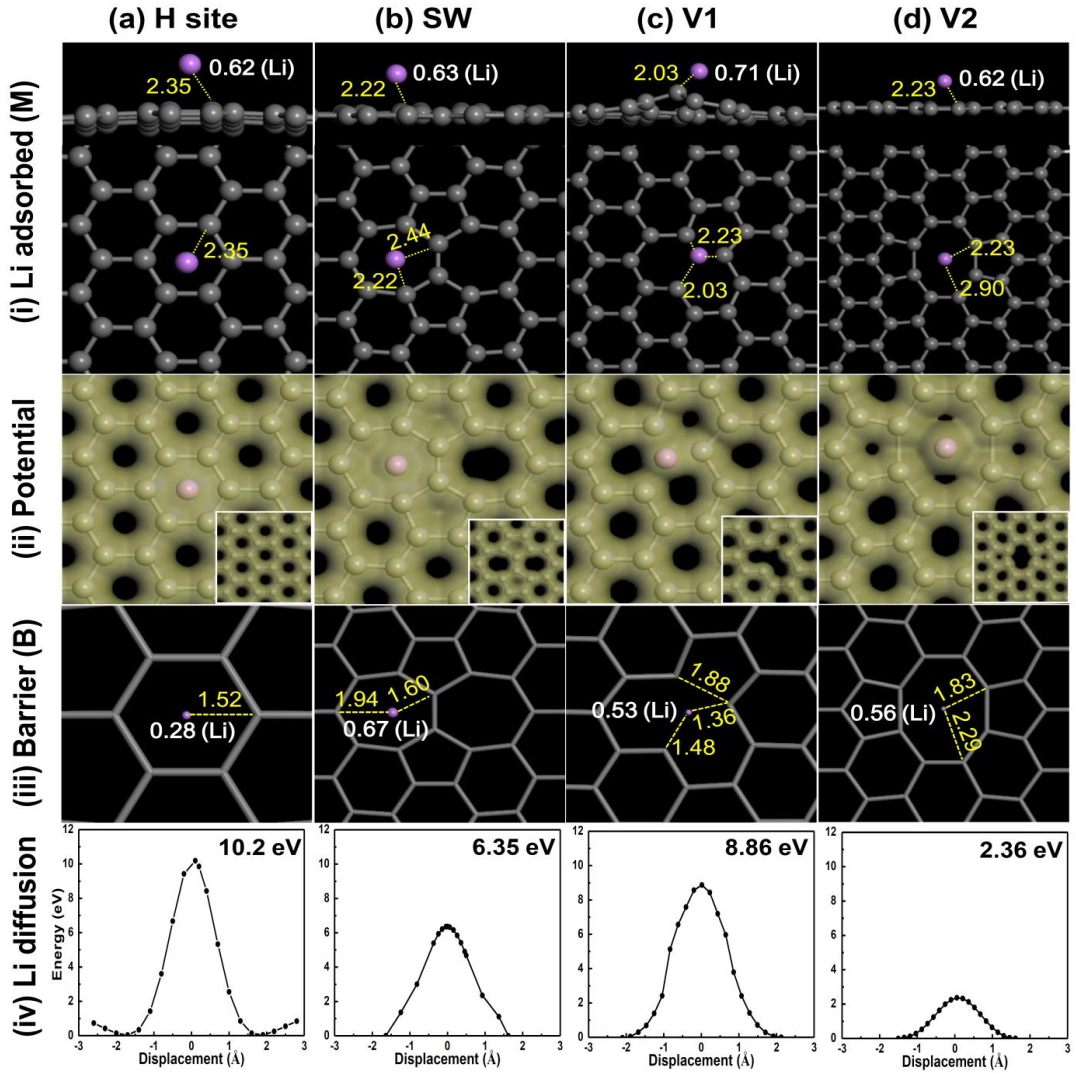

Figure 4.13. Side and top views of atomic configurations (top panel), isosurface images of electrostatic potential (second panel), bond lengths and local charge distributions at the barrier states (third panel), and the diffusion barrier profiles of Li (bottom panel) through (a) graphene hexagonal site (H site), (b) Stone-Wales (SW) defect (c) monovacancy (V1), and (d) divacancy (V2). Isovalue for rendering isosurfaces is 0.25 e/Å^3. The insets in the third panel show isosurface image of electrostatic potential for each corresponding structure without Li ion. Bond lengths (yellow color) and electrostatic potential charges (white color) are in units of Å and electrons, respectively.

Li atom adsorbs on the H site with a bond length of 2.35 Å above the graphene plane and with an adsorption energy of -1.69 eV, as shown in the upper panel of **Figure 4.13a** and **Table 4.1**. Li ESP charge at H site is partially depleted to 0.62 *e*. The ESP charge of Li atom at barrier state is 0.28 *e*, much less compared to that at the binding site. This charge difference between adsorption and barrier state is an important variable in determining the Coulomb interaction energy. As the Li approaches to the barrier site, the available space for Li is narrow with a short separation distance of 1.52 Å, invoking severe charge overlapping between Li and adjacent carbon atoms, as can be seen in the electrostatic potential contour in the second panel of **Figure 4.13a**. This increases

repulsive forces, giving rise to large diffusion barrier height of 10.2 eV, similar to the previous report (**Table 4.1**) validating our approaches. Similar situation takes place in the SW defect which is abundant in the graphene grain boundary. The Li adsorption energy near the heptagon is -1.94 eV, slightly stronger than that of H site. Although the charge overlapping is still severe, a longer separation distance of 1.60 Å and also much less charge difference between adsorption and barrier state (0.04 *e*) forms a relatively smaller activation barrier height of 6.35 eV than that of H site, as shown in **Figure 4.13b**. In the case of V1, Li adsorbs at the vacancy site with an adsorption energy of -3.12 eV, keeping closer distance (2.03 Å), as shown in the top panel of **Figure 4.13c**. The excess charge difference of Li atom between adsorption and barrier site is 0.18 *e* and the closest separation distance at the barrier site is 1.36 Å. Charges are distributed not only on the Li and carbon sites but also between them, implying both covalent bonding and ionic bonding characters due to charge depletion from Li atom. This produces a large diffusion barrier height of 8.86 eV. On the other hand, V2 provides a rather large open space with an adsorption energy of -2.36 eV near the middle of the two dimers (top panel of **Figure 4.13d**) such that a large separation distance of 2.90 Å is maintained. This gives minimizes electrostatic charge overlapping and a large bond length of 1.83 Å at the barrier state, i.e., steric hindrance is minimized, as shown in the second and third panels in **Figure 4.13d**. The charge difference between the adsorption and the barrier states is 0.04 *e*. All of these factors induced a smallest diffusion barrier height (2.36 eV) among the defects

we studied. This barrier height can be overcome under the typical charging conditions of the battery.

4.3 Summary of Chapter Four

We have studied lithium diffusion pathways with two types of graphene samples prepared by CVD; i) well-defined basal plane graphene grown on Cu foil and ii) edge plane-enriched graphene layers grown on Ni film. We have discovered that electrochemical reaction of electrode (substrate/graphene) not only is related to the number of graphene layers but also relies on the defect sites on the basal plane of graphene. The experimental and calculated results related to the specific type of defects such as divacancies and higher order defects that can assist lithium ion diffusion through basal plane could help us in designing high capacity and highly conductive corrosion-free electrode for lithium ion battery. It would be reasonable to expect that substrate protective nature of few-layer graphenes could be the basis of further investigation of preparing original substrate which remains unaltered properties and has longer lifetime under severe electrochemical corrosion conditions for battery. Furthermore, by correlating the lithium diffusion in graphene layers to the D/G intensity ratio from Raman spectra, we developed a way of predicting the graphene crystallinity from electrochemical method.

Bibliography of Chapter Four

[1] K.S. Novoselov, et al., *Science* **2004**, *306*, 666.

[2] Y.B. Zhang, Y.W. Tan, H.L. Stomer, P. Kim, *Nature* **2005**, *438*, 201.

[3] A. Altland, *Phys. Rev. Let.* **2006**, *97*, 236802.

[4] D. Chen, L.H. Tang, J.H. Li, *Chem. Soc. Rev.* **2010**, *39*,3157.

[5] D.A.C. Brownson, D.K. Kampouris, *J. Power Sources* **2011**, *196*, 4873.

[6] M. Pumera, *En. Env. Sci.* **2011**, *4*, 668.

[7] P. Lian, et al., *Electrochimica Acta* **2010**, *55*, 3909.

[8] A.K.Geims, K.S. Novoselvo, *Nat. Mater.* **2007,** *6*, 183.

[9] M.S. Fuhrer, C.N. Lau, A. H. MacDonald, *MRS Bull.* **2010**, *35*, 289.

[10] A. K. Geim, K. S. Novoselov, *Nature Mater.* **2007**, *6***,** 183.

[11] G. W. Semenoff, *Phys. Rev. Lett.* **1984**, *53***,** 5449.

[12] V. P. Gusynin, S. G. Sharapov, *Phys. Rev. Lett.* **2005**, *95*, 146801.

[13] N. M. R. Peres, A. H. Castro Neto, F. Guinea, Phys. Rev. B **2006,** *73*, 195411.

[14] K. S. Novoselov, A. K. Geim, S. V. Morozov, D. Jiang, M. I. Katsnelson, I. V. Grigorieva, S. V. Dubonos, A. A. Firsov, Nature **2005**, *438*, 197.

[15] Y. Zhang, Y.-W. Tan, H. L. Stormer, P. Kim, Nature **2005,** *438*, 20.

[16] K. S. Novoselov, Z. Jiang, Y. Zhang, S. V. Morozov, H. L. Stormer, U. Zeitler, J. C. Maan, G. S. Boebinger, P. Kim, A. K. Geim, Science **2007,** *315*, 1379.

[17] J.-C. Charlier, P. C. Eklund, J. Zhu, A. C. Ferrari, Ed. Jorio, A., G.

Dresselhaus, M. S. Dresselhaus, Berlin/Heidelberg: Springer-Verlag, **2008.**

[18] Ph.D. Thesis, Dr. Vladimiras Gavriusinas, Faculty of Physics, Vilnius University, Lithuania, **2008.**

[19] A. H. C. Neto, F. Guinea, M. N. Peres, R., K. S. Novoselov, A. K. Geim, Rev. Mod. Phys. **2009**, *81*, 109.

[20] C. Lee, X. D. Wei, J. W. Kysar, J. Hone, *Science* **2008**, *321*, 385.

[21] V. M. Pereira, A.H. Neto, **2008**, arXiv:0810.4539v1.

[22] A. A. Balandin, S. Ghosh, W. Bao, I. Calizo, D. Teweldebrhan, F. Miao, C. N. Lau, *Nano Lett*. **2008**, *8*, 902.

[23] R. R. Nair, P. Blake, A. N. Grigorenko, K. S. Novoselov, T. J. Booth, T. Stauber, N. M. R. Peres, A. K. Geim, *Science* **2008**, *320*, 1308.

[24] U. Kürüm, O. Ö. Ekiz; H. G. Yaglioglu, A. Elmali, M. Ürel, H. Güner, A. K. Mızrak, B. Ortaç, A. Dâna, *Appl. Phys. Lett.* **2011**, *98*, 141103.

[25] Q. Bao, H. Zhang, Y. Wang, Z. Ni, Y. Yan, Z. X. Shen, K. P. Loh, D. Y. Tang, *Adv. Funct. Mater*. **2009** *19*, 3077.

[26] K. S. Novoselov, A. K. Geim, S. V. Morozov, D. Jiang, Y. Zhang, S. V. Dubonos, I. V. Grigorieva, A. A. Firsov, *Science* **2004**, *306*, 666.

[27] P. Sutter, *Nat. Mater.* **2009**, *8*, 171.

[28] P. W. Sutter, J.-I. Flege, E. A. Sutter, *Nat. Mater.* **2008**, *7*, 406.

[29] I. Pletikosić, M. Kralj, P. Pervan, R. Brako, J. Coraux, A. T. N'Diaye, C. Busse, T. Michely, *Phys. Rev. Lett.* **2009**, *102*, 056808.

[30] M. Eizenberg, J. M. Blakely, *Surf. Sci.* **1970,** *82*, 228.

[31] A. Reina, X. Jia, J. Ho, D. Nezich, H. Son, V. Bulovic, M. S. Dresselhaus, J. Kong,*Nano Lett.*, **2009**, *9*, 30.

[32] K.S. Kim, Y. Zhao, H. Jang, S.Y. Lee, J.M. Kim, J.H. Ahn, P. Kim, J.Y. Choi, B.H. Hong, *Nature* **2009**, *457*, 706.

[33] F. Güneş, G. H. Han, K. K. Kim, E. S. Kim, S. J. Chae, M. H. Park, H.-K. Jeong, S. C. Lim, Y. H. Lee, *Nano* **2009**, *4*, 83.

[34] X. Li, W. Cai, J. An, S. Kim, J. Nah, D. Yang, R. Piner, A. Velamakanni, I. Jung, E. Tutuc, S. K. Banerjee, L. Colombo, R. S. Ruoff, *Science* **2009**, *324*, 1312.

[35] H. P. Boehm, A. Clauss, G. O. Fischer, U. Hofmann, *Zeitschrift für anorganische und allgemeine Chemie* **1962**, *316*, 119.

[36] X. Gao, J. Jang, S. Nagase, *J. Phys. Chem. C* **2010**, *114*, 832.

[37] M.Winter, O. J.Besenhard, E. M. Spahr, P. Novák, *Adv. Mater.* **1998**, *10*, 725.

[38] M.Winter, P. Novák, A. Monnierb, *J. Electrochem. Soc.* **1998**, *145*, 428.

[39] D. Bar-Tow, E. Peled, L. Bursteinb, *J. Electrochem. Soc.* **1999**, *146*, 824.

[40] Y. Ren, R. A. Armstrong, F. Jiao, G. P. Bruce, *J. Am. Chem. Soc.* **2010**, *132*, 996.

[41] T. Tran, K. Kinoshita, *J. Electroanal. Chem.* **1995**, *386*, 221.

[42] K. Persson, A. V. Sethuraman, J. L. Hardwick, Y. Hinuma, S. Y. Meng, A. Ven, V. Srinivasan, R. Kostecki, G. Ceder, *Phys. Chem. Lett.* **2010**, *1*, 1176.

[43] Meyer, S. Passerini, M. Winter, *J. Power Sources* **2012**, *200*, 83.

[44] B. Jungblut, E. Hoinkis, *Phys. Rev. B* **1989**, *40*, 10810.

[45] Y. Yamada, K. Miyazaki, T. Abe, *Langmuir* **2010**, *26(18)*, 14990.

[46] J. M. Tarascon, D.G. Guyomard, Extended Abstracts, *Spring Meeting of the Electrochemical Society*, May 16-21, **1993**, 93-1, Honolulu, HI, no. 69.

[47] T. Takamura, K. Endob, L. Fuc, Y. Wu, K. J. Lee, T. Matsumoto, *Electrochim. Acta*, **2007**, *53*, 1055.

[48] X. S. Li, W. W. Cai, J. H. An, S. Kim, J. Nah, D. X. Yang, R. D. Piner, A.Velamakanni, I. Jung, E. Tutuc, S. K. Banerjee, L. Colombo, R. S. Ruoff, *Science* **2009**, *324*, 1312.

[49] C. Biswas, Y. H. Lee, *Adv. Func. Mater.* **2011**, *21*, 3806.

[50] W. J. Yu, S. H. Chae, S. Y. Lee, D. L. Duong, Y. H. Lee, *Adv. Mater*. **2011**, *23(16)*, 1889.

[51] A. L. M. Reddy, A. Srivastava, R. S. Gowda, H. Gullapalli, M. Dubey, M. P. Ajayan, *ACS Nano* **2010**, *4*, 6337.

[52] J. Vetter, P. Novák, M.R. Wagner, C. Veit, K.- C. Möller, J.O. Besenhard, M. Winter, M. Wohlfahrt-Mehrens, C. Vogler, A. Hammouche, *J. Power Sources* **2005**, *147*, 269.

[53] P. Arora, E. R. White, *J. Electrochem. Soc.* **1998**, *145*, 3647.

[54] T. Wijesinghe, D. Blackwood, *Corrosion Science* **2007**, *49*, 1755.

[55] S. Kadry, *European. J. Scientific Research* **2008**, *22*, 508.

[56] C.T. Hyams, J. Go, M.T. Devinea, *J. Electrochem. Soc.* **2007**, *154*, C390.

[57] S.-W. Song, J. T. Richardson, V. G. Zhuang, M. T. Devine, W. J. Evans, *Electrochim. Acta* **2004**, *49*, 1483.

[58] X. Zhang, B. Winget, M. Doeff, W. J. Evans, M. T. Devine, *J. Electrochem. Soc.* **2005**, *152*, B448.

[59] E. Pollak, B. Geng, K.-J. Jeon, T. I. Lucas, J. T. Richardson, F. Wang, R. Kostecki, *Nano Lett.* **2010**, *10*, 3386.

[60] A. L. M. Reddy, A. Srivastava, R. S. Gowda, H. Gullapalli, M. Dubey, M. P. Ajayan, *ACS Nano* **2010**, *4*, 6337.

[61] S. Chen, L. Brown, M. Levendorf, W. W. Cai, S.-Y. Ju, J. Edgeworth, X. Li, C. Magnuson, A. Velamakanni, D. R. Piner, J. Kang, J. Park, S. R. Ruoff, *ACS Nano* **2011**, *5*, 1321.

[62] D. Prasai, J. C. Tuberquia, R. R. Harl, G. K. Jennings, K. I. Bolotin, *ACS Nano* **2012**, *6 (2)*, 1102.

[63] G. H. Han, F. Güneş, J. J. Bae, E. S. Kim, S. J. H.-J. Shin, J.-Y. Choi, D. Pribat, Y. H. Lee, *Nano Lett.* **2011**, *11*, 4144.

[64] S. J. Chae, F. Güneş, K. K. Kim, E. S. Kim, G. H. Han, S. M. Kim. H.-J. Shin, S.- M. Yoon, J.-Y. Choi, M. H. Park, C. W. Yang, D. Pribat, Y. H. Lee, *Adv. Mater*. **2009**, *19(16)*, 2553.

[65] F. Güneş, G. H. Han, H.-J. Shin, S. Y. Lee, M. Jin, D. L. Duong, S. J. Chae, E. S. Kim,; F. Yao, A. Benayad, J.-Y. Choi, Y. H. Lee, *Nano* **2011**, *6*, 409.

[66] C. Casiraghi, S. Pisana, K. S. Novoselov, A. K. Geim, A. C. Ferrari, *Appl. Phys. Lett.* **2007**, *91*, 233108.

[67] R. R. Nair, P. Blake, A. N. Grigorenko, K. S. Novoselov, T. J. Booth, T. Stauber, N. M. R. Peres, A. K. Geim, *Science* **2008**, *320*, 1308.

[68] E.J. Yoo, J. Kim, E. Hosono, H. S. Zhou, T. Kudo, I. Hunma, *Nano Lett.* **2008**, *8*, 2277.

[69] J. P. Perdew, K. Burke, M. Ernzerhof, *Phys. Rev. Lett.* **1996**, *77*, 3865.

[70] Li, X.; Geng, D.; Zhang, Y.; Meng, X.; Li, R.; Su, X. *Electrochem. Commu.* **2011**, 13, 822.

[71] P.G. Bruce, B. Scrosati, J. - M. Tarascon, *Angew. Chem. Int. Ed*. **2008**,*47*, 2930.

[72] J. Yan, J. Zhang, Y.C. Su, X. G. Zhang, B. Xia, J. *Electrochim. Acta.* **2010**, *55*, 1785.

[74] K. N. Kudin, B. Ozbas, H. C. Schniepp, R. K. Prud’homme, I. A. Aksay, R. Car, *Nano Lett.* **2008**, *8*, 36.

[75] T. M. G. Mohiuddin, A. Lombardo, R. R. Nair, A. Bonetti, G. Savini, R. Jalil, N. Bonini, D. M. Basko, C. Galiotis, N. K. Marzari, S. Novoselov, A. K. Geim, A. C. Ferrari, *Phys. Rev. B* **2009**, *79*, 205433.

SUMMARY

Carbon-Based Nanomaterials as an Anode for Lithium Ion Battery

The improvement of the capacity of raw CNF mat has been realized in the current research through electrochemical deposition of Si. The Si/CNF mat prevents the use of metal substrate, binder, and conducting polymers. However, several drawbacks of the current free-standing Si/CNF mat structure need to be mentioned: (i) The as-fabricated CNF mat exhibited a rather lower conductivity compared to that of CNTs which could be the reason for the original low capacity (< 300 mAh/g) of raw CNF mat. (ii) The flexibly of the as-fabricated CNF mat reduces after high temperature annealing which hinders the further investigation for flexible anode applications. These two factors can be further improved by the incorporation of CNTs, graphene flakes or other more advanced materials. (iii) Although the interfacial binding strength of Si and CNF was improved by the formation of Si-C bond through annealing as discussed in the context, structural pulverization of deposited Si film induced by the large volume expansion during charge/discharge was still observed in the current structure. Therefore, increasing the Si anchoring sites on the CNF mat by the surface functionalization and enhancing the degree of entanglement through the introduction of CNTs could provide better structure stability. The optimization to improve composite

structures for capacity, charge transfer, and cycle life is further required for industry applications.

On the other hand, in order to clarify the Li diffusion pathways through graphene plane and the role of defects in Li diffusion to reveal the mystery of Li-C system, graphene was used as a media for the study of this fundamental science of diffusion in this work. We found that the electrochemical performance of few-layer graphenes which are overlapped up to three layers of single layer graphene is strongly affected by the substrate reaction. Experimental results showed that 6 layers of basal plane-enriched large area graphene were needed to provide sufficient substrate protection from severe electrolyte attack. Li diffusion across the pure basal plane of graphene is strongly limited and nevertheless non-negligible diffusion is still allowed, suggesting possible diffusion through defects that might be formed on the graphene plane. Combing the experimental results and density functional theory calculations, we found that divacancies and higher order defects can be shortcuts for lithium ion diffusion with respect to the graphene basal plane. Further exploration of high energy density and long lifetime anode by fabricating high capacity materials on graphene could be an interesting research direction in the future.

Key Words: nanocarbon materials, lithium ion battery, carbon nanofiber, silicon, Graphene

CURRICULUM VITAE

FEI YAO

LPICM-École Polytechnique, CNRS (UMR 7647)
Laboratoire de Physique des Interfaces et Couches Minces
Route de Saclay; 91128 PALAISEAU Cedex, France

IBS Center for Integrated Nanostructure Physics, Institute for Basic Science, Department of Energy Science, Sungkyunkwan University
Room 85689, Corporate Collaboration Center, 300 Cheoncheon-dong, Jangan-gu, Suwon, Gyeonggi-do 440-746, Korea · 82-31-299-6509 ·
Mobile: +82-10-2757-1299
E-mail: apaperyao@gmail.com, yaofei@skku.edu

Education

2010.08 ~	Ph.D. candidate LPICM-École Polytechnique Laboratoire de Physique des Interfaces et Couches Minces, Route de Saclay; 91128 PALAISEAU Cedex , France; IBS Center for Integrated Nanostructure Physics, Institute for Basic Science, Department of Energy Science, Sungkyunkwan University, Korea. Advisor: Professor Young Hee Lee Dr. Costel-Sorin Cojocaru
2008.03 ~ 2010.08	M.S Sungkyunkwan Advanced Institute of Nanotechnology Sungkyunkwan University Korea. Advisor: Professor Young Hee Lee

2003.09~2007.09 B.S
Department of Electronic Information Engineering
Shandong Normal University
China.

RESEARCH EXPERIENCE

1. CNT gas sensor fabrication
   - Enhancement of sensitivity to NO_2, SO_2, NH_3 gases etc.
   - Selectivity among NO_2, SO_2, NH_3 gases etc.
2. Dispersion of SWCNTs / MWCNTs
   - In water with surfactant (SDS, NaDDBS etc)
   - In organic solution (NMP, DCE etc)
3. Synthesis of graphene and carbon nanotubes by chemical vapor deposition
   - Large-area few-layer graphene synthesis on metal substrates (Ni, Cu), etching & transfer onto desired substrates (SiO_2, PET etc.)
   - Large-area monolayer graphene growth on Cu foil, etching & transfer processes
   - Synthesis of SWCNTs network and MWCNTs by chemical vapor deposition
4. Doping of graphene for electrode applications
   - P-type doping by metal-salts and acid solutions for enhancement of conductivity for flexible transparent conducting film applications
   - Multiple-layered graphene film preparation and investigation of conductivity enhancement by Layer-by-Layer (LBL) doping
5. Carbon nanofiber fabrication using electrospinning method for energy application
   - Carbon nanofibers with CNT composite
   - Carbon nanofiber with Si composite
6. Si-based material synthesis and energy storage applications
   - Si thin film deposition by PECVD for energy application (lithium ion battery, solar cell)
   - Si nanoparticle deposition by electrochemical method for battery application.
7. Fuel cell application with carbon-based materials

EQUIPMENTS

- Plasma enhanced CVD, Thermal CVD, Atomosphere pressure CVD
- E-beam and thermal evaporator
- Magnetron sputter
- Micro Raman and confocal Raman spectroscopy
- High resolution scanning electron microscope (HR-SEM)
- Atomic force microscope (AFM)
- UV-NIR absorption spectroscopy
- Potentiostat /Galvanostat equipment
- Spray equipment
- Electrospinning equipment

PUBLICATIONS (SCI journal)

12. Fethullah Gunes*, **Fei Yao***, Hongyan Yue, Hung T. Nguyen, Bing Li, and Young Hee Lee, 'A direct synthesis of Si-nanowires on a 3D porous graphene as high performance anode material for Li-ion batteries', 2013, submitted.

11. M. Jin, **Fei Yao**, J. Chang, and Y. H. Lee, 'Graphene sheets as anode materials with super high rate and large capacity for Lithium ion batteries' 2013, in preparation.

10. Jian Chang, Meihua Jin, **Fei Yao,** and Young Hee Lee, 'Asymmetric Supercapacitors Based on Graphene/MnO_2 Nanospheres and Graphene/MoO_3 Nanosheets with High Energy Density ' 2013, Adv. Func. Mater., accepted.

9. Seung Mi Lee, **Fei Yao,** and Young Hee Lee, 'Lithium ion diffusion through basal plane of graphene: A density functional theory study' 2013, J. Nanoscience and nanotechnology, submitted.

8. **Fei Yao**, Bing Li., Fethullah Gunes, Costel Sorin Cojocaru, and Lee, Y. H. 'Silicon and carbon nanofiber composite as an anode material for lithium ion battery' 2013, Nanoscale, submitted.

7. Thuc Hue Ly, Dinh Loc Duong,Quang Huy Ta, **Fei Yao**, Quoc An Vu, Hye Yun Jeong, Sang Hoon Chae, and Young Hee Lee, 'Nondestructive Characterization of Graphene Defects' 2013, Adv. Func. Mater, accepted.

6. **Fei Yao**, Fethullah Gunes, Huy Quang Ta, Seung Mi Lee, Seung Jin Chae, Kyeu Yoon Sheem, Costel Sorin Cojocaru, Si Shen Xie, and Young Hee Lee, 'Diffusion Mechanism of Lithium Ion through Basal Plane of Layered Graphene', J. Am. Chem. Soc., 134(20), 8646-8654, (May 23, 2012).

5. Hung T. Nguyen, **Fei Yao**, Mihai R. Zamfir, Chandan Biswas, Kang Pyo So, Young Hee Lee, Seong Min Kim, Seung Nam Cha, Jong Min Kim, Didier Pribat, 'Highly Interconnected Si Nanowires for Improved Stability Li-Ion Battery Anodes', Advanced Energy Materials ,1(6), 1154–1161, (Nov, 2011).

4. Fethullah Güneş, Gang Hee Han, Hyeon-Jin Shin, Si Young Lee, Meihua Jin, Dinh Loc Duong, Seung Jin Chae, Eun Sung Kim, **Fei Yao**, Anass Benayad, Jae-Young Choi and Young Hee Lee, 'UV Light-Assisted Oxidative Sp3-Hybridization of Graphene', NANO, 6 (5),409–418, (May 26, 2011).

3. **Fei Yao**, Dinh Loc Duong, Seong Chu Lim, Seung Bum Yang, Ha Ryong Hwang, Woo Jong Yu, Il Ha Lee, Fethullah Gunes, and Young Hee Lee, 'Humidity-assisted selective reactivity between NO_2 and SO_2 gas on carbon nanotubes', J. Mat. Chem., 21(12), 4502-4508, (Mar. 28, 2011).

2.Il Ha Lee, Un Jeong Kim, Hyung Bin Son, Seon-Mi Yoon, **Fei Yao**, Woo Jong Yu, Dinh Loc Duong, Jae-Young Choi, Jong Min Kim, Eun Hong Lee and Young Hee Lee, 'Hygroscopic Effects on AuCl3-Doped Carbon Nanotubes', Journal of Physical Chemistry C, 114(26), 11618-11622 ,(Jun. 10. 2010).

1. **Fei Yao**, Seong Chu Lim, Woo Jong Yu, Il Ha Lee, Fethullah Gunes, Ha Ryong Hwang, Seung Bum Yang, Kang Pyo So, Gang Hee Han, and Young Hee Lee, 'AC Response to Gas Exposure in Vertically Aligned Multiwalled Carbon Nanotube Electrode', J. Phys. Chem. C, 114(8), 3659-3663, (Feb. 5, 2010).

PATENTS (Korea)

Large Area Graphene as a Protecting Layer for Metal Corrosion, submitted.

Presentations

---

6. **Fei Yao,** Bing Li, Kangpyo So, Jian Chang, Vu Quoc An, Didier Priba1, Costel Sorin Cojocaru, Hongyan Yue, Sishen Xie, Young Hee Lee1, 'Silicon-Coated Carbon Nanofiber Mat for Anode of Lithium Ion Battery', Imaginenano 2013, Bilbao, Spain, April 23~26, 2013, oral.

5. **Fei Yao,** Fethullah Gunes, Ta Quang Huy, Seung Mi Lee, Seung Jin Chae, Kyeu Yoon Shem, Costel Sorin Cojocaru, Si Shen Xie, Young Hee Lee, 'Lithium Ion Diffusion Through Basal Plane of Layered Graphene Synthesized by Chemical Vapor Deposition', 16th International Meeting on Lithium Batteries (New Era for Smart Energy Storage) (IMLB 2012), ICC Jeju, Korea, June 17~22, 2012, p.104.

4. **Fei Yao,** Hung Tran Nguyen, Kang Pyo So, Chandan Biswas, Giduk Kwon, Si Thanh Pham, Zamfir Mihai Robert, Young Hee Lee and Didier Pribat, 'Carbon Nanofiber/Si Nanowire As an Anodematerial for Li-Ion Battery', 1st Korean-French Seminar On Nanomaterials for Energy, Sungkyunkwan University, Mar. 6-8,2011, p.50

3. **Fei Yao,** Hung Tran Nguyen, Kang Pyo So, Chandan Biswas, Giduk Kwon, Si Thanh Pham, Zamfir Mihai Robert, Young Hee Lee, Dider Pribat, 'Carbon Nanofiber/Si Nanowire as An Anode Material for Li-Ion Battery', A3 Symposium on Emerging Materials: Nanocarbons and Nanowires for Energy, Core-Riviera Hotel, Jeonju, Nov. 7-11. 2010, p.61

2. **Fei Yao,** Duong Dinh Loc, Seong Chu Lim, Seung Bum Yang, Ha Ryong Hwang, Woo Jong Yu, Fethullah Gunes, Young Hee Lee, 'Humidity-assisted selective reactivity between NO_2 and SO_2 gas on carbon nanotubes', NT10(11th International Conference on the Science and Application of Nanotubes 2010), Hilton Bonaventure Montreal, Quebec, Canada, Jun 27-Jul 2. 2010, p.96

1. **Fei Yao,** Seong Chu Lim, Woo Joong Yu, Fethullah Gunes and Young Hee Lee 'Capacitive Gas Sensor of Vertically Aligned Carbon Nanotubes', International Green Energy Nanocarbon Conference 2009,Jeollabuk-do provincial office, Jeonju, Korea, Nov. 3~6. 2009, p.155